UNIVERSITY OF CALIFORNIA
RIVERSIDE

Search for New Physics in All-Hadronic Events With the Compact Muon Solenoid Experiment at the Large Hadron Collider

A Dissertation submitted in partial satisfaction
of the requirements for the degree of

Doctor of Philosophy

in

Physics

by

Pawandeep Singh Jandir

June 2016

Dissertation Committee:

Professor Owen Long, Chairperson
Professor Stephen Wimpenny
Professor Jose Wudka

The Dissertation of Pawandeep Singh Jandir is approved:

Committee Chairperson

University of California, Riverside

Acknowledgments

An undertaking of this magnitude is not accomplished alone. It is influenced, guided, and aided by countless others. I am grateful to a wide array of individuals and I will attempt to express my gratitude to all these individuals here. To anyone I miss in this list, I apologize. This work would not have been possible without the fantastic effort of the thousands who made the Large Hadron Collider (LHC) and Compact Muon Solenoid (CMS) a reality. The extraordinary work by the LHC staff and my CMS collaborators has been incredible as the excellent performance of both machines has yielded impressive results.

I give sincere thanks to my thesis adviser Owen Long. I regard myself as very lucky to have the privilege of working alongside him all these years. More than just special technical ability, he showed me vision, determination, and leadership. He put up with my naïveté with tireless patience. And with his support and guidance, instilled in me confidence. Thank you!

The help provided by the rest of the UCR group has also been tremendous. Bill Gary is a constant with immense knowledge and insightful comments. Sudan Paramesvaran, Jared Sturdy, and Harold Nguyen were indispensable in integrating and easing me to the group and to CERN. I am very grateful to them for this, particularly Jared, whose couch I called home when I first arrived at CERN. I very much enjoyed my partnership with Florent Lacroix as well. Thank you all!

I also had the pleasure of being in a very talented analysis team. The RA2*b* group taught me much about teamwork and focus. I owe special thanks to: Joshua Thompson, Keith Ulmer, Alessandro Gaz, Luke Winstrom, Jim Smith, Bill Ford, Troy Mulholland, Jeff Richman, Ben Kreis, Rishi Patel, Jim Hirschauer, Kevin Pedro, Nhan Tran, Andrew Whitbeck, Jack Bradmiller-Feld, and Manuel Sevilla. In particular, Joshua and Keith took me under their wing. I appreciate the time they spent guiding me and answering my many questions. To these collaborators, thank you!

I would also like to thank my HCAL colleagues in teaching me the ins and outs of the HCAL subsystem, notably, Salavat Abdoulline, Aleko Khukhunaishvili, Bugra Bilin, Richard Kellogg, and Pawel De Barbaro. The countless meetings and after-hours discussions were invaluable to me.

I owe many thanks to Marshall Styczinski, Osama Almughrabi, Matthew Scholl, Philip Buss, Hank Nguyen, Lindsay Perrigo, and Jessica Scheimer who made my undergraduate years unforgettable. Your friendships mean the world to me.

Without my family, I could not have stayed sane these past years. They helped me overcome any setbacks. My unbelievable sisters Mandeep and Rajhdeep made childhood easy, somehow. Their continuous support, encouragement and love has sustained me. I greatly value and admire them. Their belief in me is very much appreciated. My brothers Jasbir and Sandeep are incomparable gentlemen, whom I aspire to be like. Thank you all!

I also must recognize my guiding star. She lifted me up when I needed it the most and whose smile lights up my world. Thank you Samreen.

I owe an un-payable debt to my parents and I speak to you directly. You birthed me, raised me, and taught me. You gave me life. You too made many sacrifices to give us an easier life. I can never forget the unconditional love and support you gave me. It is an honor to be your son. This achievement is meant to both thank and honor you, my parents. I could not have done anything in my life without you. I love you with all my being. You have my unending and eternal appreciation.

And to my dad, whom I miss so terribly. You were taken much too soon from us. Thank you for everything. I love you and will continue to do so forever.

To Mummaji and Papaji for showing me the path and to Samreen for lighting that path when it had become dark.

ABSTRACT OF THE DISSERTATION

Search for New Physics in All-Hadronic Events With the Compact Muon Solenoid Experiment at the Large Hadron Collider

by

Pawandeep Singh Jandir

Doctor of Philosophy, Graduate Program in Physics
University of California, Riverside, June 2016
Professor Owen Long, Chairperson

In this dissertation, a search for New Physics is presented in proton-proton collisions at $\sqrt{s} = 13$ TeV. This collision data was collected by the Compact Muon Solenoid detector at the CERN Large Hadron Collider located in Geneva, Switzerland in 2015 and corresponds to an integrated luminosity of $2.3\,\mathrm{fb}^{-1}$. The search analyzes events with zero leptons and large hadronic activity. The data is divided into search regions of jet multiplicity, bottom quark tagged jet multiplicity, missing transverse momentum, and scalar sum of jet transverse momenta. The observed event count in the search regions are found to be in agreement within the standard model expectation. Thus, the results are interpreted in the context of simplified supersymmetric models of gluino pair production leading to a significant improvement in the exclusion limits on the possible mass of the gluino and neutralino.

Contents

List of Figures

List of Tables

Part I

Physics background and motivation

Chapter 1

Introduction

Equipped with his five senses, man explores the universe around him and calls the adventure Science.

- Edwin Powell Hubble [1]

The search for truth has been a driving force of humanity for millennia. From early Greek and Indian philosophers in the 1st millennium BCE to French philosophers in the 18th century CE, there has been an unquenchable thirst for knowledge and understanding of nature. As humanity has explored, science has developed as a tool to understand nature and the universe. Scientists of the 19th century developed atomic theory, seemingly proving the ancient theory of indivisible and indestructible atoms correct. However, in 1897, J.J. Thomson discovered the electron, showing the atom was made up of even smaller particles [2]. The electron heralded the dawn of a new era of science and physics: the field of elementary particle physics was born. The 20th century saw the discovery of the proton and neutron, the main sub-atomic particle constituents of the atom along with the electron.

In the time since, particle physicists have made great strides probing the sub-atomic scale using a wide variety of experimental apparatuses with ever greater precision. This has led to the discoveries of numerous other fundamental particles and the further formulation and development of theoretical models.

This dissertation will give an overview of the current understanding in particle physics. Despite the many advances, there are still unanswered questions about the universe. It is commonly understood that undiscovered physics processes should exist to describe the unexplained phenomena. These issues and a proposed theoretical solution is presented in Chapter 2. The experimental apparatus and particle reconstruction methods used in this dissertation are given in Chapters 3 and 4. A search for a presently unknown particle is presented in Chapters 5, 6, and 7. Chapter 5 serves as an introduction to the analysis, Chapter 6 describes the background estimation techniques used, and Chapter 7 gives the results of the search. Finally, the conclusion is presented in Chapter 8.

Chapter 2

Theory and Motivation

2.1 The Standard Model

Particle physics is the study of the elementary particles that make up matter and the interactions among them. In the late 20th century, particle physicists developed a self-consistent model which both describes a vast array of experimental observations with high precision and makes testable predictions. This Standard Model (SM) of particle physics is now a successful mathematical framework accurately describing the fundamental physics interactions we have observed. The elementary particles of the SM are depicted in Fig. 2.1 and the interactions between them in Fig. 2.2. This overview is not meant to be comprehensive; a much more detailed description can be found in Ref. [3].

The central feature of the SM, a quantum field theory, is local gauge invariance under the

$$SU(3)_C \times SU(2)_L \times U(1)_Y \tag{2.1}$$

symmetry group. $SU(3)_C$ describes the color interactions among quarks, $SU(2)_L$ describes the weak interactions among the quarks and leptons and $U(1)_Y$ describes the electromagnetic interaction. These three interactions correspond to the three fundamental forces (ignoring gravity): the strong force, the weak force and the electromagnetic force, respectively.

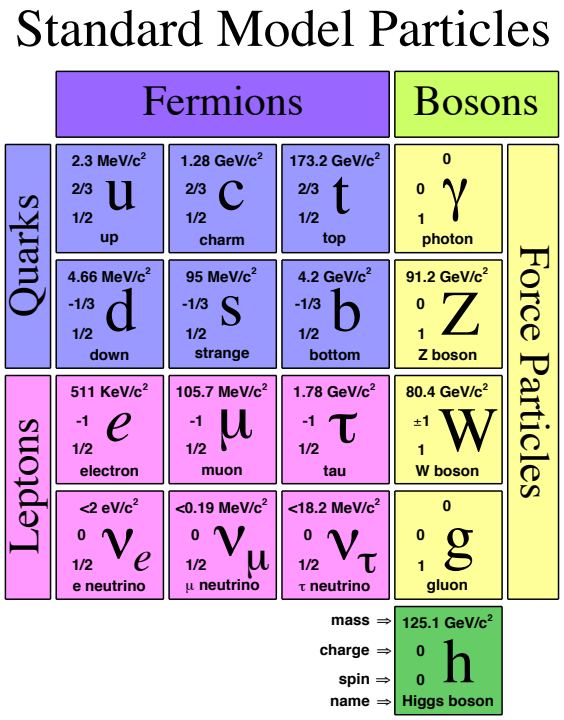

Figure 2.1: The SM particles, with the fermions occupying the left three columns of the figure and the bosons the last, right-most column.

The electroweak force then is the group $SU(2)_L \times U(1)_Y$, where the weak and electromagnetic forces have been unified [4].

Experiments spanning several decades have shown the SM to be accurate and successful. These experiemnts have shown the existence of predicted particles in addition to other aspects of the validity of the SM [5–8]. The Higgs mechanism, responsible for the spontaneous breaking of the $SU(2)_L \times U(1)_Y$ electroweak symmetry, is an important piece of the SM [4, 9, 10]. A new boson with mass of 125 GeV was found at the general purpose detectors at the Large Hadron Collider in 2012. This new particle seems to be consistent with the SM Higgs boson, the particle associated with the Higgs mechanism [11, 12]. The experimental proof of this particle finally answers one of the long standing questions of the SM as now the entirety of Fig. 2.1 is now known.

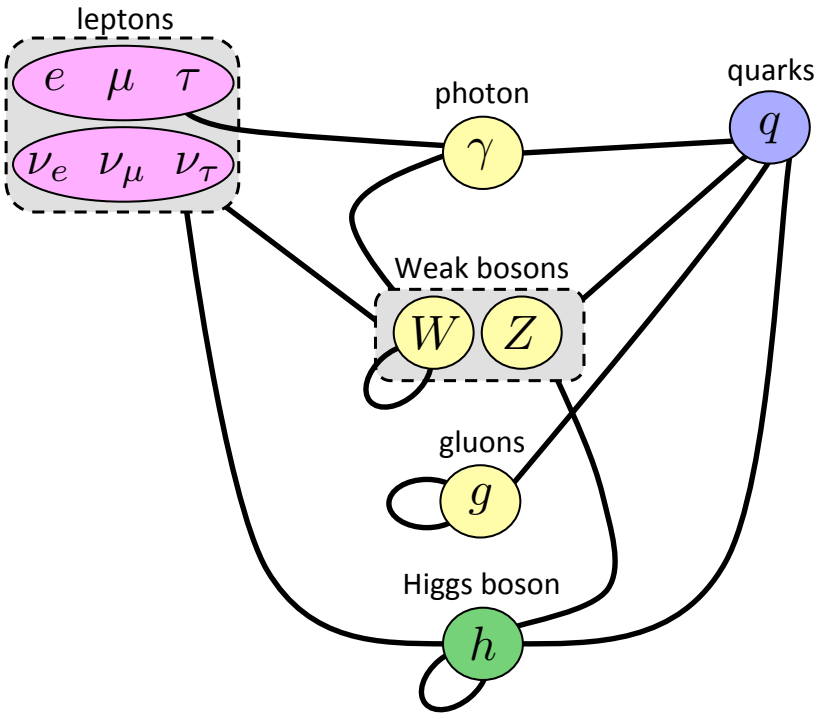

Figure 2.2: An illustration of the SM particles and their interactions with each other. The fermions occupy the left and right columns of the figure while the bosons occupy the middle column. The black solid lines represent the possible interactions. Note a loop to itself indicates a self-interacting particle.

2.2 Motivation for Physics beyond the Standard Model

While the Standard Model has been very successful, it is still not a complete theory of Nature. Although the SM predictions agree with a multitude of measurements and can explain many phenomena, there still remain some open questions:

Description of gravity: Gravity is very well measured on astronomical to atomic scales, but is not described in the SM as its strength is nearly zero in comparison to the other three forces. Can the description of gravitation, formulated in a gauge quantum field theory, be related to the SM?

Unification of forces The electronic and the magnetic forces were reformed to a single unified theory [13]. Similarly, the electromagnetic and weak forces can be described

by the electroweak theory. Unification is not just an elegant way to formulate laws of nature from a mathematical point of view, but it improves the understanding of nature [14]. Can the strong and electroweak forces be unified as well? If so, do they have the same origin?

Astrophysics observations The mass of galaxies and other astronomical structures estimated by gravitational effects is much larger than the mass estimated from the visible matter for these objects. The matter which interacts only via gravity but not through the strong or electromagnetic forces is a possible explanation to this observation. This type of matter is called Dark Matter. Neutrinos are SM particles that fit this profile of matter, but their contribution to Dark Matter is very small [15]. While there is indirect evidence for Dark Matter [16], no Dark Matter particle has been found yet.

Much more matter than anti-matter is observed (for example many more electrons than positrons [17]). Some mechanism must exist which explains the excess of matter in comparison to anti-matter.

Hierarchy problem The mass scale of higher-order corrections to the SM Higgs boson mass can end up being much larger than the on-shell Higgs boson mass itself [14]. This is the hierarchy problem.

2.3 Supersymmetry

One of the ways to solve many of the above problems is to introduce a new symmetry between the fermions and bosons of the SM. This SUper SYmmetry (SUSY) [14,18,19] transforms a boson into a fermion and vice versa:

$$Q|\text{Boson}\rangle = |\text{Fermion}\rangle \qquad Q^\dagger|\text{Fermion}\rangle = |\text{Boson}\rangle. \tag{2.2}$$

The $Q(Q^\dagger)$ operators are generators of the supersymmetric transformations. The single particle states of supersymmetry are constructed as irreducible representations of the alge-

bra associated with supersymmetry and are known as supermutliplets. Each particle and its superpartner are grouped in a supermultiplet by definition.

A chiral supermultiplet is composed of a single fermion, with two helicity states, and two real scalars, which are grouped in a complex scalar field. All SM fermions along with their superpartners can then be grouped this way. The naming convention of these resulting scalars is defined by prepending a s to the SM particles' name (such as sbottom). They all have spin-0. A gauge supermultiplet is composed of a massless spin-1 vector boson and a spin-$\frac{1}{2}$ superpartner (called a gaugino), each with two helicity states. If gravity is included, the graviton (the gauge boson for the gravitational force with spin-2) and its superpartner, the gravitino, form their own supermultiplet. The partners of the SM bosons have *ino* appended at the end of their name (such as gluino). The particle content of the Minimal Supersymmetric Standard Model (MSSM) is shown in Table 2.1 [18, 19]. The particles known as neutralinos (denoted by χ^0) result from the mixing of the bino, wino, and neutral higgsinos. These states are notable in that they can be experimentally determined and thus are of particular interest in the search presented in this thesis.

2.3.1 R-parity

Because of new couplings in the MSSM, baryon number, B, and lepton number, L, are no longer conserved. However, no violation of either quantum number has ever been observed [21]. Thus, a new quantum number P_R, R-parity, is introduced and is assumed to be conserved:

$$P_R = (-1)^{3(B-L)+2s}, \tag{2.3}$$

where s is the spin of the particle. All SM particles have P_R of $+1$ while SUSY particles have P_R of -1. As a consequence of this conservation law:

- Supersymmetric particles are produced in even numbers.

Table 2.1: SUSY particles of the MSSM. After electroweak symmetry breaking, the bino and the neutral wino mix to photino and zino. This table is adapted from [20].

Names	Spin	P_R	Gauge Eigenstates	Mass Eigenstates
Higgs Boson	0	+1	$H_u^0\ H_d^0\ H_u^+\ H_d^-$	$h^0\ H^0\ A^0\ H^\pm$
squarks	0	-1	$\tilde{u}_L\ \tilde{u}_R\ \tilde{d}_L\ \tilde{d}_R$	(same)
			$\tilde{s}_L\ \tilde{s}_R\ \tilde{c}_L\ \tilde{c}_R$	(same)
			$\tilde{t}_L\ \tilde{t}_R\ \tilde{b}_L\ \tilde{b}_R$	$\tilde{t}_1\ \tilde{t}_2\ \tilde{b}_1\ \tilde{b}_2$
sleptons	0	-1	$\tilde{e}_L\ \tilde{e}_R\ \tilde{\nu}_e$	(same)
			$\tilde{\mu}_L\ \tilde{\mu}_R\ \tilde{\nu}_\mu$	(same)
			$\tilde{\tau}_L\ \tilde{\tau}_R\ \tilde{\nu}_\tau$	$\tilde{\tau}_1\ \tilde{\tau}_2\ \tilde{\nu}_\tau$
neutralinos	1/2	-1	$\tilde{B}^0\ \tilde{W}_0\ \tilde{H}_u^0\ \tilde{H}_d^0$	$\tilde{\chi}_1^0\ \tilde{\chi}_2^0\ \tilde{\chi}_3^0\ \tilde{\chi}_4^0$
charginos	1/2	-1	$\tilde{W}^\pm\ \tilde{H}_u^+\ \tilde{H}_d^-$	$\tilde{\chi}_1^\pm\ \tilde{\chi}_2^\pm$
gluino	1/2	-1	$\tilde{g}$	(same)
goldstino (gravitino)	1/2 (3/2)	-1	$\tilde{G}$	(same)

- When a supersymmetric particle decays, there will always be at least one daughter supersymmetric particle.
- The lightest supersymmetric particle (LSP) cannot decay and is stable.

2.3.2 SUSY motivation

The result of the conservation of R-parity is that the LSP will be produced at the end of all SUSY decay chains. If the LSP is electrically neutral, it becomes a very good Dark Matter candidate. Due to the cancellation between the diagrams involving SM particles and the analogous diagrams involving their superpartners (i.e. SUSY particles), the quadratic divergences to the Higgs boson mass are cancelled to all orders in perturbation theory. This alleviates the hierarchy problem of the SM. As shown in Fig. 2.3, the electroweak and strong interactions will unify in strength at energy scales of $\sim 10^{16}$ GeV. These three predictions or features of SUSY make it a desirable extension to the SM.

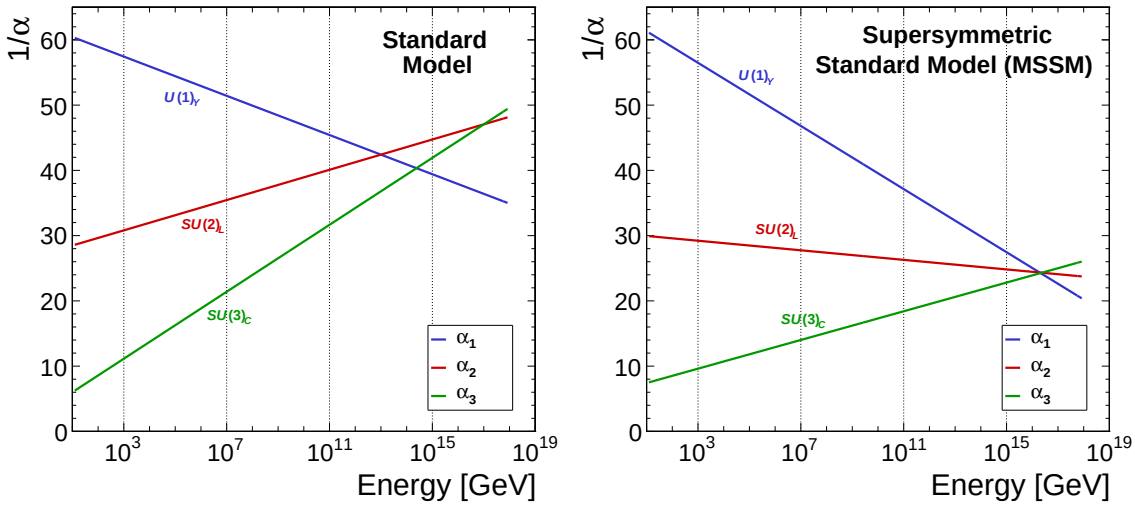

Figure 2.3: The inverses of the three gauge coupling constants plotted against the energy scale. They change from their very well measured values at the low energy scale (at the mass of the Z boson) to higher energies using the equations of the Standard Model (left plot) and of the Minimal Supersymmetric Standard Model at the SUSY breaking scale M_{SUSY} ~1 TeV (right plot). These three gauge couplings are as follows: α_1 is the electromagnetic interaction (blue), α_2 is the weak interaction (red), and α_3 is the strong interaction (green).

However, If SUSY particles had the same mass as their SM counterparts, their discovery would be trivial. However, no such particles have been observed. This implies SUSY is not a perfect symmetry but a broken one and the masses of the SUSY particles must be larger than their corresponding SM partners. The actual SUSY breaking mechanism is not known, but many models can provide the mechanism for SUSY breaking such as mediation through gravity or other explicit insertion of terms into the supersymmetric Lagrangian. Additional models for this SUSY breaking can be found in Ref. [22].

2.3.3 Experimental searches and strategies

There are a host of different signatures in supersymmetric models. Observation of SUSY in these different channels is then critical as it will strengthen the interpretation of the discoveries. This thesis will focus on the all hadronic search channel, as strong production modes tend to have the highest cross sections. There are advantages to studying other

search channels, such as photonic ones, since hadronic activity can be difficult to measure. In that sense, the photonic search channel can be easier to analyze.

One way to measure hadronic activity is in the form of 'jets.' Free quarks and gluons create showers of decay particles (hadrons). This process, called hadronization, occurs because particles must be color neutral, otherwise the particle will have quark-antiquark pairs spontaneously created around it. The resulting narrow cluster of hadrons is called a jet and an illustration of this is shown in Fig. 2.4. Thus, when there is lots of quark and gluon activity in an event, there will be many jets.

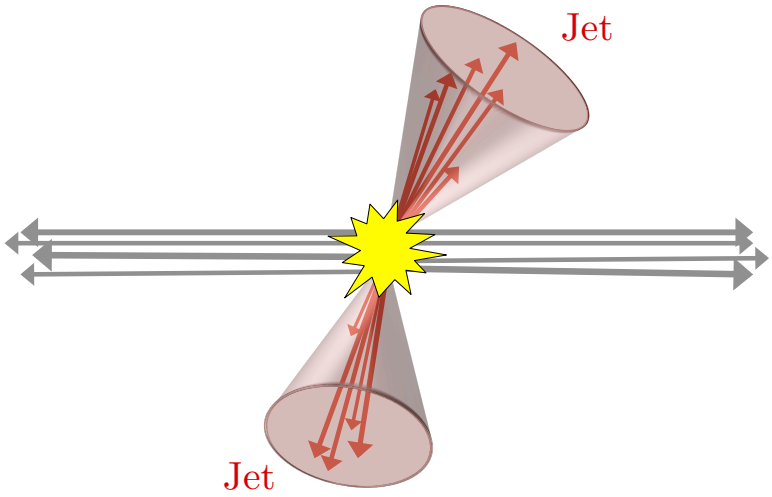

Figure 2.4: Simple illustration of a hard scattering pp collision which consists of a cluster of hadrons (red arrows) traveling roughly in the direction of the initial beam particles (gray arrows) and two clusters of hadrons (i.e. 'jets' in red cones) with large transverse momentum. The two large transverse momentum jets are roughly back-to-back in azimuthal angle.

Another common search variable is missing transverse momentum. The transverse component of the missing momentum is used because the colliding partons in the beam axis have unknown momentum, but the initial energy in the transverse plane is zero. Thus any net momentum in the transverse direction is indicative of missing transverse momentum.

As discussed previously, R-parity conserving SUSY will yield a weakly interacting,

long-lived, stable LSP which will escape detection. However, this will leave behind an energy imbalance, i.e. missing transverse momentum, so the LSP can still be detected if indirectly. Because the SUSY particles have large masses, the decay chains tend to involve many particles. This of course will result in large numbers of final-state particles. It becomes imperative then to be able to detect as precisely as possible, the energy and activity in the detector.

The past several decades have seen experimental searches for SUSY at the Large Electron-Positron Collider (LEP) formerly located in the current Large Hadron Collider (LHC) tunnel at the European Organization for Nuclear Research (CERN) [23] as well as at the Tevatron [24] located at Fermilab. At the LHC, the Compact Muon Solenoid (CMS) and A Toroidal LHC ApparatuS (ATLAS) general-purpose experiments continue to search for SUSY. Thus far, no search has uncovered any such experimental evidence. Presented in 2014, a summary of SUSY results for CMS is shown in Fig. 2.5. This shows the excluded range of sparticle masses using Simplified Model Spectra (SMS) signal samples (see Sec. 5.1.3). Note Fig. 2.5 is not a completely exhaustive list nor does it contain any information from recently completed 2015 and 2016 searches. This thesis will present one of these new 2015 CMS searches in all-hadronic final states, that is, events where there are no leptons.

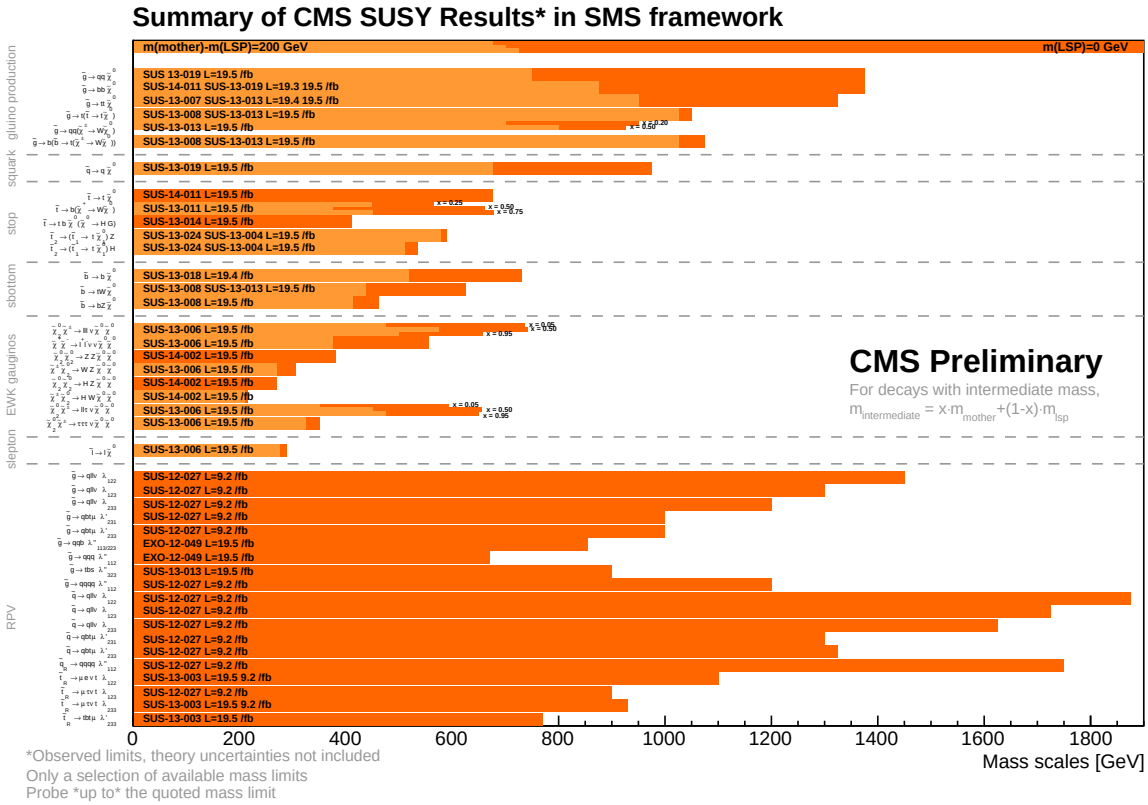

Figure 2.5: These are the best exclusion limits presented at the 2014 ICHEP conference by CMS. The limits are obtained within the SMS framework. Branching ratios of one are assumed and values shown in this plot are to be interpreted as upper limits. From Ref. [25].

Part II

Experimental tools

Chapter 3

Experimental Setup

The Large Hadron Collider (LHC) is the world's largest high energy particle accelerator and collider, located at the European Organization for Nuclear Research (CERN) in Geneva, Switzerland whose aim is to test the predictions of the SM and reveal the physics beyond the SM [26]. The Compact Muon Solenoid (CMS) experiment is a general-purpose detector that measures the properties of particles produced from pp and heavy-ion collisions at the LHC. In this thesis, a search for SUSY with the Compact Muon Solenoid detector at the Large Hadron Collider using 2015 data is presented. This chapter provides a technical overview and description of the design of both the LHC and CMS.

3.1 Large Hadron Collider

The LHC is a two-ring superconducting hadron accelerator. It is designed to collide oppositely rotating proton bunches with a centre-of-mass energy ($\sqrt{s}$) of 14 TeV (i.e. 7 TeV per beam) and luminosity of 10^{34} cm^{-2}s^{-1} (or 36 pb^{-1} per hour). It can also collide heavy ions (Pb) with an energy of 2.8 TeV per ion and a luminosity of 10^{27} cm^{-2}s^{-1} (or 3.6 μb^{-1} per hour). However, the LHC did not start at its designed 14 TeV center-of-mass energy. Instead it increased over the years of its operation: this can be seen in Table. 3.1.

Protons are extracted from a duoplasmatron source (a device which ionizes hydro-

Table 3.1: Maximum center-of-mass energy of LHC pp running in the different years of operation.

Year	2011	2012	2015	2016+
$\sqrt{s}$ [TeV]	7	8	13	14 (design)

gen atoms). These protons gain kinetic energy in several preaccelerators. First the protons are accelerated in the Linac2 to 50 MeV, then by the Proton Synchrotron Booster to 1.4 GeV, then by the Proton Synchroton to 26 GeV and finally by the Super Proton Synchroton to 450 GeV. This injector chain gets the protons into the LHC main ring where they are accelerated to their final energy. Note also that for heavy ion running, the ions are accelerated by the Linac3 instead of Linac2 which bypasses the usual Proton Synchrotron Booster stage. The acceleration in the LHC is performed by radio-frequency (RF) cavities running at 400 MHz with a field of 5.5 MV/m. In addition to this main purpose, the RF cavities keep the proton beam separated in short and dense bunches. The beams are bent into a circular orbit by 1,232 superconducting dipole magnets. The limiting factor of the proton beam energy is the maximum magnetic field of 8.33 T. Because the proton beams are oppositely run in the LHC ring, two separate beam lines are required. This means all LHC ring structures need to have two separate bending coils and RF cavities for each beam. The full accelerator complex can be seen in Fig. 3.1.

The LHC has a circumference of 27 km and is located ∼100 m underground on the Franco-Swiss border. There are two general purpose detectors located at approximately opposite positions in the ring: the Compact Muon Solenoid (CMS) [28] and A Toroidal LHC ApparatuS (ATLAS) [29] experiments. The two other large detectors are the Large Hadron Collider beauty experiment (LHCb) [30], which is specialized in measuring b-quark dominated events and the A Large Ion Collider Experiment (ALICE) [31], which is optimized to study heavy ion collisions. The arrangement of these experiments and the LHC can be seen in Fig. 3.2.

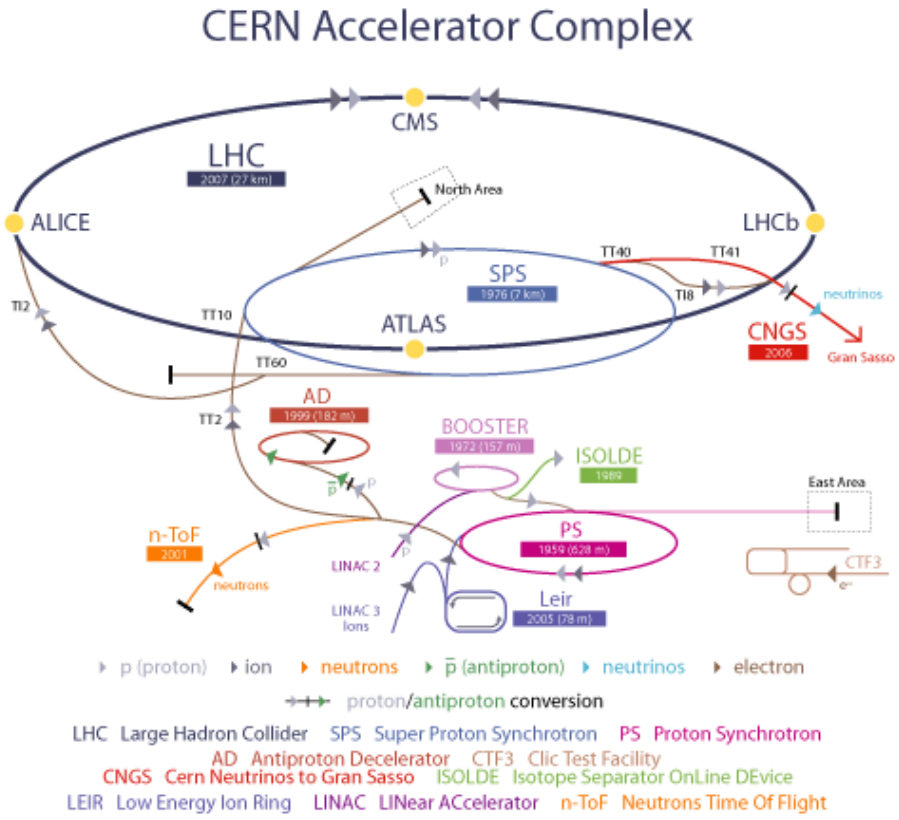

Figure 3.1: The full schematic view of the LHC accelerator complex. From Ref. [27].

The number of events generated in the LHC can be shown as:

$$N_{\text{Event}} = L\sigma_{\text{Event}} \tag{3.1}$$

where σ_{Event} is the cross section for the event and L is the machine luminosity. Protons are accelerated in bunches of approximately $N_{\text{b}} = 1.15 \times 10^{11}$ protons. Up to $n_{\text{b}} = 2808$ bunches are injected per beam. With the revolution frequency f_{rev} of 11.245 kHz set by the LHC circumference, an instantaneous luminosity,

$$L = \frac{N_{\text{b}}^2 n_{\text{b}} f_{\text{rev}} \gamma_{\text{r}}}{4\pi\varepsilon_{\text{n}}\beta*} F, \tag{3.2}$$

of 10^{34} cm^{-2}s^{-1} (or 36 pb^{-1} per hour) can be achieved by design. The γ_r is the relativistic gamma factor ($\gamma_{\text{r}} = E_{\text{p}}/m_{\text{p}}c^2$) which is set by the beam energy. In 2015 the center-of-mass

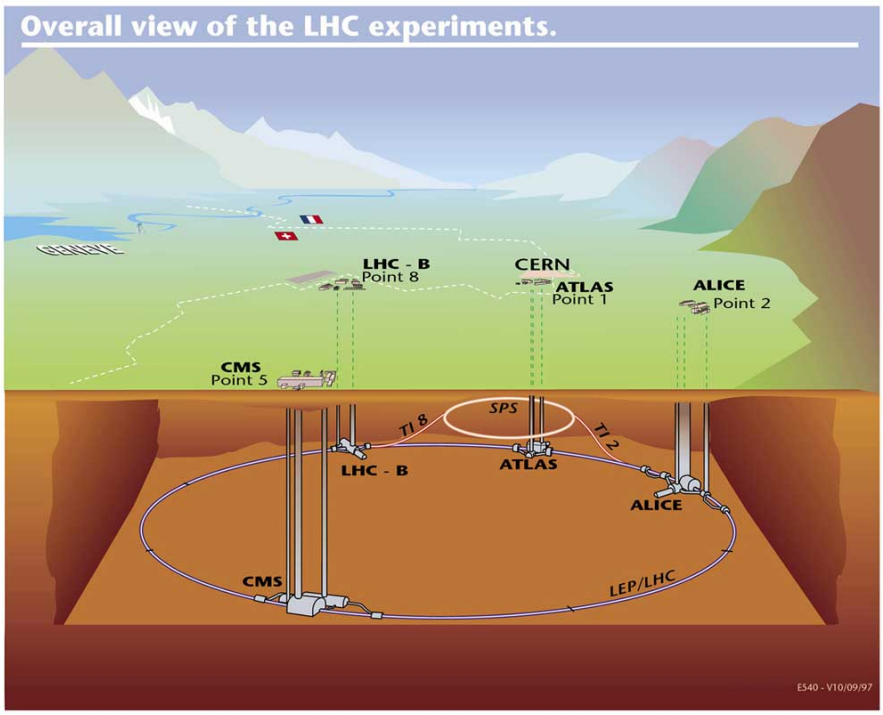

Figure 3.2: Sketch of the LHC tunnel below the Franco-Swiss boarder near Geneva. The location of the four main experiments CMS, ATLAS, LHCb, and ALICE is shown. From Ref. [32]

energy was 13 TeV, so the beam energy was 6.5 TeV. ε_{n} is the normalized beam emittance of 3.75 mm·mrad. It is a measure of the spread of the beam in the plane transverse to its motion. $\beta*$ is a measure of the transverse size of the particle beam at the collision point; it is related to the focusing strength of the magnets at those points. It has a value of 0.55 m. Lastly, F is a geometric luminosity reduction factor related to the crossing angle of the bunches when they collide.

The luminosity delivered by the LHC does not remain constant over the course of a physics collision run; it decays and is limited by:

- the beam emittance, which must fit into the small aperture of the superconducting LHC magnets;
- the synchrotron radiation produced thermal energy, which must be absorbed by the

cryogenic system (restricts the total intensity $n_{\mathrm{b}} \cdot N_{\mathrm{b}}$);

- the beam-beam effect causing a spread in the number of oscillations of particles about their stable orbits, which must to be kept below a certain limit (restricts the transverse beam brightness $N_{\mathrm{b}}/\varepsilon_{\mathrm{n}}$)
- the space-charge limit in the injectors (scales with $N_{\mathrm{b}}/\varepsilon_{\mathrm{n}}$)

These sources of beam loss restrict the total lifetime of the beam to approximately 15 hours. In addition, the large numbers of protons in a single bunch increases the chances that more than one collision will occur. This implies that in a single bunch crossing, there can be multiple collisions. The additional collisions, not from the primary collision, are termed Pile-Up (PU).

A measurement of the amount of data that has been recorded by the LHC and CMS is important. It is done by calculating the time integral of the instantaneous luminosity. CMS keeps track of these values as that which has been 'delivered' and 'recorded.' The delivered luminosity refers to the amount the LHC provides to the experiments, and is thus seen by CMS. If everything operated perfectly, the delivered and recorded luminosities would be the same. Unfortunately, in certain instances, CMS is unable to take data due to a busy data acquisition chain or a subsystem being down. The recorded and delivered luminosity for CMS across its operation is shown in Fig. 3.3. Previous to 2015, the LHC delivered bunches with spacing of a fixed 50 ns. This was lowered to the design value of 25 ns for 2015. The total integrated luminosity recorded in 2015 is $3.81\,\mathrm{fb}^{-1}$. This corresponds to 90% of the delivered luminosity. The peak luminosity achieved during this period was $5.13 \times 10^{33}\mathrm{cm}^{-2}\mathrm{s}^{-1}$ [33].

3.2 Compact Muon Solenoid Detector

The Compact Muon Solenoid (CMS) experiment is one of the two general purpose detectors on the LHC [28]. It is located at Point 5 on the LHC ring, as can be seen in

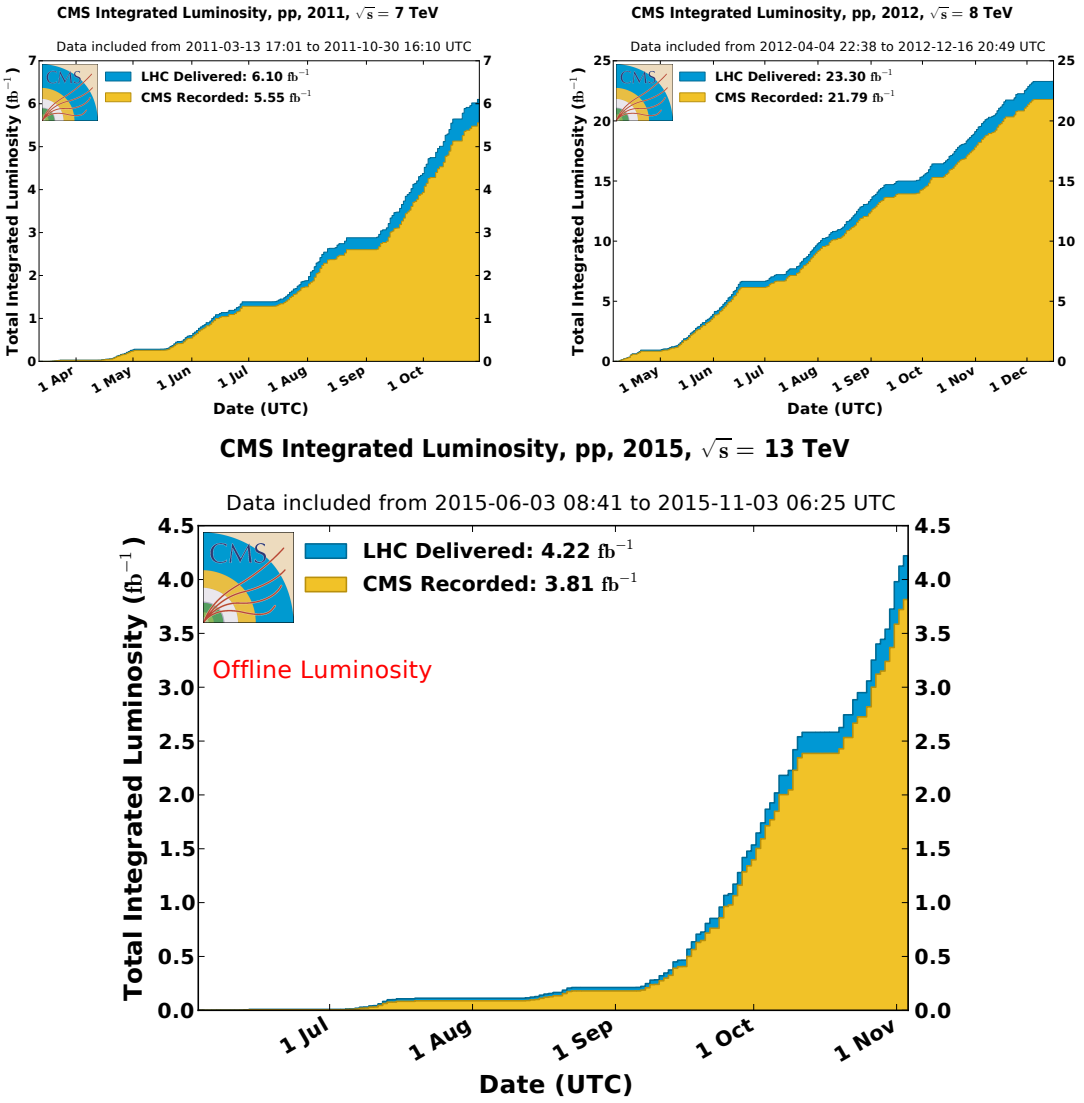

Figure 3.3: The delivered and recorded luminosity of CMS as a function of time. The top left shows the luminosity for 2011, the top right shows the luminosity for 2012 and the bottom shows the luminosity for 2015. In all plots the delivered luminosity is in blue and the recorded luminosity is in yellow. From Ref. [33]

Fig 3.2. The physics goals of CMS are:

- discover the Higgs boson and study its properties,
- search for beyond the SM physics, such as extra dimensions or SUSY,
- test the validity of the SM at the TeV scale by conducting high precision measurements

of the SM

- observe and investigate rare processes in the heavy-flavor sector of the SM,
- and study quark-gluon plasma using heavy-ion collisions.

In order to achieve these goals CMS is required to have:

- good muon identification and reconstruction, good muon momentum resolution over a large range of angles and momenta, good dimuon mass resolution ($\approx$ 1% at 100 GeV), and excellent muon charge identification (for muons with p $<$ 1 TeV);
- good charged particle reconstruction and momentum resolution inside the tracker and pixel detectors close to the interaction area to allow efficient triggering and (offline) tagging of tau leptons and b-quark jets;
- good electromagnetic energy resolution, good diphoton and dielectron mass resolution ($\approx$ 1% at 100 GeV), large geometric coverage of the interaction area, rejection of π^0 particles, and efficient photon and lepton isolation (at high luminosities);
- and good missing transverse energy and dijet mass resolution, which requires hadron calorimeters with a wide hermetic geometrical coverage and fine lateral segmentation.

This has allowed for excellent reconstruction efficiencies and energy resolution for photons, electrons, muons, and hadrons (mesons or baryons) [34].

The CMS experiment is built out of many sub-detectors. The innermost part features the silicon pixel and strip detectors which measure the tracks and momenta of charged particles. The next two parts are the electromagnetic crystal and hadron sampling calorimeters, which measure the energies of photons, electrons, and hadrons. The symbolic center of the CMS experiment is the superconducting magnet, which encloses the sub-detectors already described. To enable the tracking system to precisely measure the momenta of charged particles, a strong magnetic field is needed to bend the tracks of charged particles. To that end, the solenoid, which is 6 m-in-diameter and 12.5 m-long, produces a magnetic

field of 3.8 T. This also allows the detector to be built in a tightly packed way. Surrounding the solenoid, a steel yoke, made out of five wheels and two endcaps, enables the return of the magnetic flux. The muon system is built within the steel return yoke, giving additional track measurements for muons. The very forward region contains additional hadron calorimeters to supplement the measurement of energy in an event. The architecture of the experiment can be separated into two parts: a cylindrical onion-shape at the center around the beamline (i.e. the barrel) and two flat endcaps at the forward ends of the detector. This gives CMS a near 4π coverage of the interaction point. A schematic view of CMS is shown in Fig. 3.4.

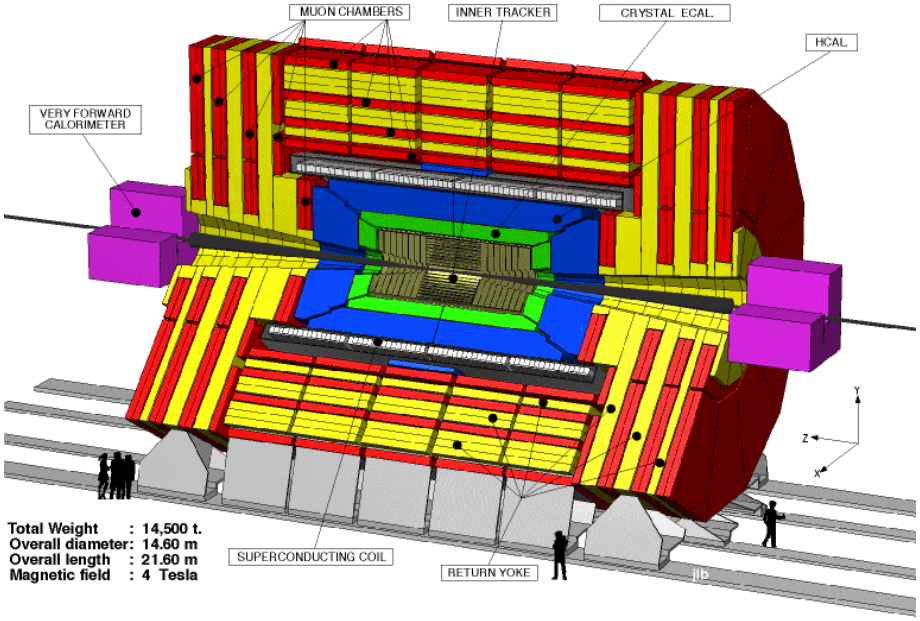

Figure 3.4: Overview of the CMS detector with labelled sub-detectors. For scale, people are shown at the bottom of the detector. From Ref. [35]

3.2.1 Coordinate System

The center of the detector near the point of collision defines the origin of the coordinate system used by CMS. The x-axis points towards the center of the LHC, the

y-axis points vertically upwards, and the z-axis lies in the direction of the beam pipe. This forms the right-handed coordinate system and is shown towards the bottom right of Fig. 3.4. The distance r, to the z-axis, is defined as $\sqrt{x^2 + y^2}$. The azimuthal angle ϕ is measured within the $x - y$ plane from the x-axis, ranging from -π to π. The polar angle θ is measured from the positive z-axis. Rapidity is commonly used in theoretical predictions since rapidity differences are Lorentz invariant along the z-axis. However, this rapidity,

$$y = \frac{1}{2} \ln \frac{E + |\vec{p}|}{E - |\vec{p}|}, \tag{3.3}$$

is difficult to use in experiments, as the mass of particles is often not known. Instead the pseudorapidity, defined as

$$\eta = -\ln \tan \frac{\theta}{2}, \tag{3.4}$$

is a good approximation to the rapidity for particles moving close to the speed of light. Note that the pseudorapidity, like the rapidity, is a Lorentz invariant quantity. The $\eta - \phi$ plane then becomes a standard way to define physical quantities as will be shown. Fig. 3.5 shows how the pseudorapidity behaves as a function of θ. Distances can be measured in this plane by an angular separation variable:

$$\Delta \mathrm{R} = \sqrt{\Delta\phi^2 + \Delta\eta^2}. \tag{3.5}$$

A benefit of using ΔR as a measure is that it is also Lorentz invariant.

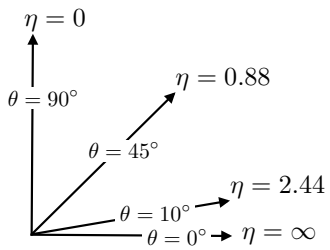

Figure 3.5: A view of the $\theta - \eta$ plane used in CMS. Varying points along the plane are shown.

A common issue facing all hadron colliders is the fact that the longitudinal momenta of the initial partons are not known. Because the initial transverse momenta are small, and the total transverse momentum must be conserved, the total transverse momentum of all final states must also be small. Accordingly, the transverse momenta of the final states are more meaningful than the absolute value of the momentum. The transverse momentum is then defined as

$$p_{\mathrm{T}} = |\vec{p}| \sin\theta. \tag{3.6}$$

In the same way, the transverse energy is defined as

$$E_{\mathrm{T}} = E \sin\theta. \tag{3.7}$$

3.2.2 Tracking System

The heart of CMS is the tracking system, constructed solely of silicon tracking technology. The tracker is designed to measure the trajectories and vertices of charged particles coming from the collision point. The momentum of a particle can be calculated using the size of the curvature in its trajectory through the magnetic field. The tracking system employs p-n junctions to identify ionization signals from charged particles that cross the p-doped and n-doped silicon sensor materials. The silicon sensors are reverse biased to get a depletion region, a region without any charge carriers but with a strong electric field. Accordingly, when a charged particle traverses the fully depleted sensor, the resultant charge carriers drift to the anode or cathode. This ionization current is measured by the read-out electronics, which is proportional to the energy loss of the particle. The tracker is composed of an inner pixel detector and an outer strip tracker. The pixel and strip trackers are supplemented by endcaps, which extend the pseudorapidity coverage of the tracker to $|\eta| < 2.5$.

At the design luminosity of the LHC, approximately 1,000 particles from 20 pp interactions every bunch crossing (every 25 ns) is expected to be produced. Thus, the

particle flux is largest at $r < 10$ cm. Because of this, the pixel detector was designed to limit the hit occupancy below 1%. This is done with 1,440 pixel modules, where each sensor measures 100×150 μm^2. For 20 cm $< r <$ 110 cm, the particle flux decreases enough to enable the use of 15,148 silicon strips, commonly $\sim$10 cm $\times$ $\sim$100 μm.

3.2.2.1 Pixel Tracker

The purpose of the pixel detector is to reconstruct the secondary vertices from tau or b-quark decays and provide seed tracks for reconstruction of outer tracks. It is composed of three barrel layers (BPix) at varying radii of 4.4, 7.3, and 10.2 cm each. The barrel is sandwiched by two pixel modules (FPix). In sum, there are 66 million pixels in the BPix+FPix structure (48 million and 18 million respectively). This system supplies three hits for each pixel seed over the full pseudorapidity range, $|\eta| < 2.5$. The layout of the pixel detector within the whole tracking system is shown in Fig. 3.6. Because all produced particles must first pass through the pixel tracker before the rest of the detector, the spatial resolution of the pixel detector must be fine, which has been measured to be between 15 and 20 μm.

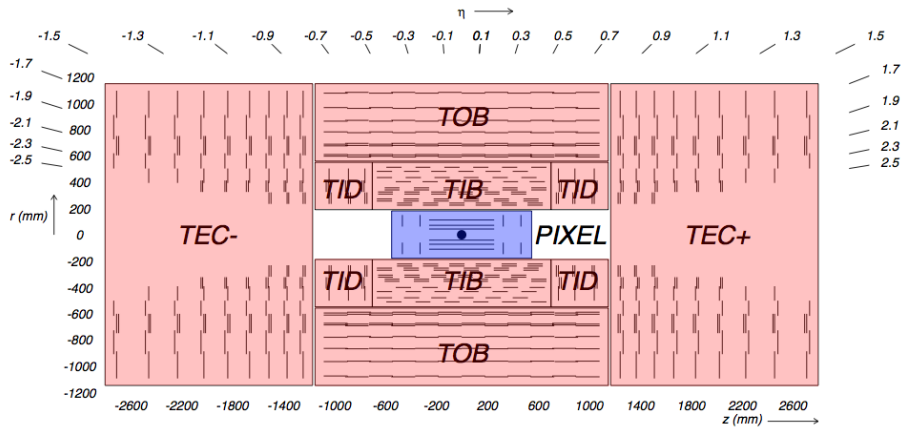

Figure 3.6: Schematic of the CMS tracker system with labelled subsystems. The pixel detector is in blue in the middle of the figure while the silicon strip detectors form the red. From Ref. [34]

3.2.2.2 Strip Tracker

The strip tracker consists of three different subsystems and ensures at least 9 hits. First, the Tracker Inner Barrel (TIB) and Tracker Inner Disk (TID) extend from $20 < r < 55$ cm and are composed of 4 barrel layers and 3 endcap disks on each end. Secondly, the Tracker Outer Barrel (TOB), which covers a radius up to 116 cm, encompasses the TIB/TID. The TOB is composed of 6 barrel layers and extends in z between $\pm$ 118 cm. Lastly, on each end is the Tracker End Cap (TEC), which each cover $124 < |z| < 282$ cm and $22.5 < r < 113.5$ cm. Each TEC is composed of 9 disks. These subsystems are shown in Fig. 3.6 as well. The first two layers of the TIB, TID, and TOB in addition to rings 1, 2 and 5 of the TEC have a supplemental micro-strip module installed on the back at a stereo angle of 100 mrad. This double-sided layer technique assures that $\sim$4 hits are two-dimensional. The resolution in the TIB and TOB is 230 and 530 μm, respectively. In the TEC, the resolution varies.

Every silicon strip tracker is composed of one (two) silicon sensor module(s) braced by a frame of graphite or carbon. To insulate the silicon sensor, a Kapton circuit layer is used. In addition, it supplies an electrical connection to the back plane. When there are two sensors, the strips use a wire bond connection. One sensor is used in the modules in the inner barrel, inner disks, and rings 1-4 in the endcaps. Two sensors are used in the outer barrel and rings 5-7 of the endcaps.

3.2.3 Electromagnetic Calorimeter

The Electromagnetic Calorimeter (ECAL) lies outside the tracking system. The major purpose of the ECAL is to measure photon and electron energy. High energy photons lose energy by pair production (create a electron-positron pair) and high energy electrons generally lose energy by bremsstrahlung, in matter. Therefore, when a high energy photon or electron enters the ECAL, it will create an electromagnetic (EM) shower.

The ECAL, a hermetic calorimeter, consists of 75,848 lead-tungstate crystals. It

is composed of a barrel which is sandwiched on each end by endcaps. The barrel covers a pseudorapidity range of $|\eta| < 1.479$, while the endcaps cover $1.479 < |\eta| < 3.0$. In the barrel, a supermodule has 1,700 crystals arranged in a 20×85 grid in the $\phi \times \eta$ plane. One row, in ϕ, is formed by laying two supermodules end-to-end. The barrel then is made of 18 rows. In the endcap, the rest of the available 14,648 crystals are distributed nearly evenly amongst 18 wedge-shaped sectors. A layered pre-shower consisting of a lead absorber and silicon detectors stands in front of each endcap. The pre-shower serves to discern prompt photons and photons that arise from neutral hadron decay. Higgs boson physics depends on this crucial tool to differentiate photons. The geometry of the ECAL is shown in Fig. 3.7.

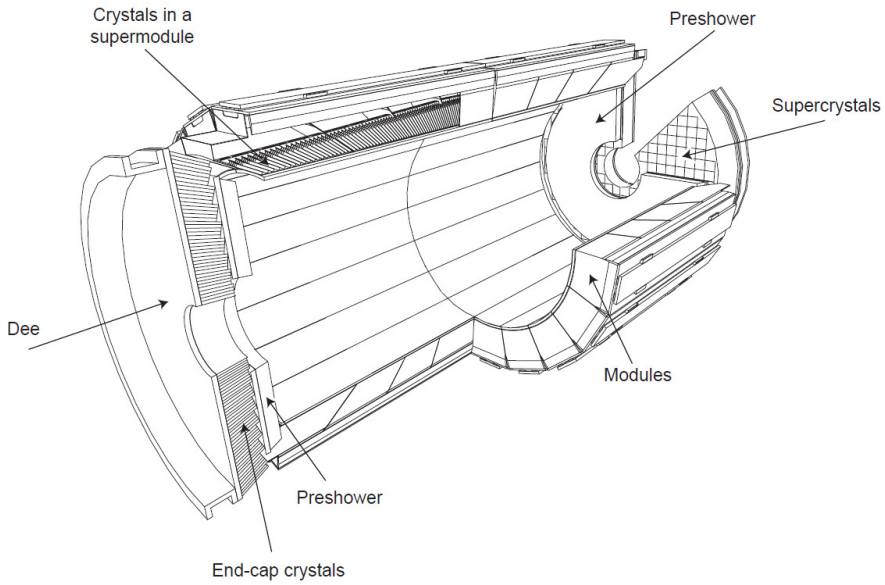

Figure 3.7: Schematic of the CMS ECAL with labelled parts. From Ref. [36]

The lead-tungstate crystals used in the ECAL were selected because of their radiation hardness, short radiation length ($X_0 = 0.89$ cm), and small Moliére radius (2.2 cm). Knowing that most EM showers can be contained in 20 X_0, 230 mm, which for the crystals used corresponds to 25.8 X_0, is used. A particle traversing the crystals will scintillate allowing the avalanche photodiodes in the barrel or vacuum photodiodes in the endcaps to

collect the emitted light and measure the energy of the particle. A sample crystal from the ECAL with attached photodetectors is shown in Fig. 3.8. The total energy resolution of the ECAL can be parameterized as:

$$\left(\frac{\sigma}{E}\right)^2 = \left(\frac{S}{\sqrt{E}}\right)^2 + \left(\frac{N}{E}\right)^2 + C^2, \tag{3.8}$$

where S is the stochastic term dominated by event-to-event fluctuations and photostatistics; N is the term describing digitization, electronic, and Pile-Up noise; and C is the constant term taking into account inter-calibration errors, non-uniformity of the longitudinal light collection and leakage of energy from the back of the crystal. A normal energy resolution for the ECAL in CMS was measured using electron beams with momenta between 20 and 250 GeV to be:

$$\left(\frac{\sigma}{E}\right)^2 = \left(\frac{2.8\%}{\sqrt{E[GeV]}}\right)^2 + \left(\frac{12\%}{E[GeV]}\right)^2 + (0.3\%)^2\,. \tag{3.9}$$

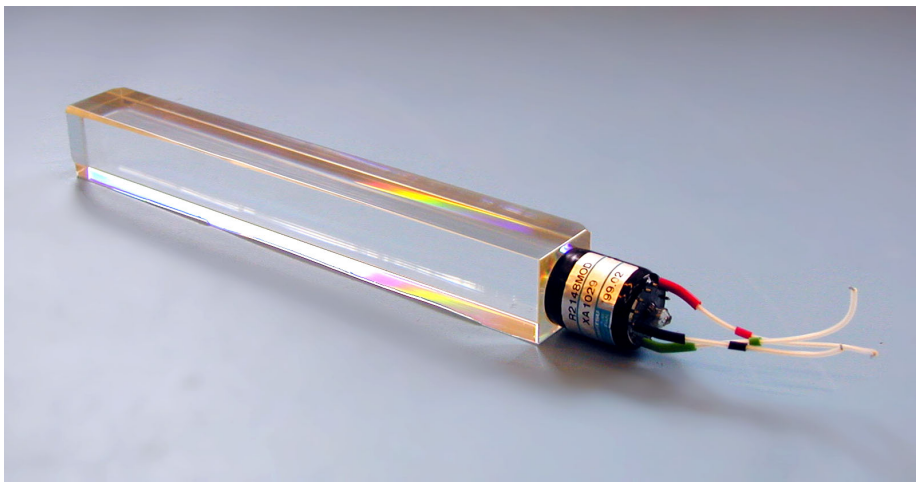

Figure 3.8: Photo of ECAL crystal with photodiode. From Ref. [36]

3.2.4 Hadron Calorimeter

Outside the ECAL and inside the magnet is the Hadron Calorimeter (HCAL) which is designed to complement the energy measurement of hadrons. Measurements of jet energy and missing energy are crucial and cannot be done without the HCAL. The HCAL is separated into four components: the Hadron Barrel (HB) and Hadron Endcap (HE) detectors, enclosed inside the magnet, the Hadron Outer (HO) detector located just outside the magnet, and the Hadron Forward (HF) detector in the very forward region close to the beam line.

The HCAL is composed of an absorber and scintillator sampling calorimeter. In the HB, which covers $|\eta| < 1.3$, there are 16 absorber plates made out of brass save for the very first and last plates which are made of steel. The brass comes from decommissioned Russian Navy shells, shown in Fig. 3.10. The thickness of the brass plates varies between 50.5-56.6 mm while the inner (outer) steel plate is 40 (70) mm thick. There is radiation-hard plastic scintillator between the absorber plates. This active material is 3.7 mm thick, except for the first and last layers which are 9 mm thick. For $|\eta| = 0.0$ (1.3), the sampling corresponds to 5.82 (10.6) interaction lengths (λ_I). In the HB, the channel segmentation, or granularity, is $\Delta\eta \times \Delta\phi = 0.087 \times 0.087$.

A hadronic shower at central psuedorapidities cannot be fully contained within the HB. Thus, the HO is needed and HCAL is extended beyond the magnet. In this instance, the solenoid also acts as an absorber material. In the HO, covering $|\eta| < 1.262$, there are two scintillator layers interspersed with a 19.5 cm thick iron plate in the innermost ring, and one scintillator layer for the outer rings. The effective interaction length of the HCAL is then extended to a minimum of 11.8 λ_I in the barrel.

In the HE, covering $1.3 < |\eta| < 3.0$, there are 79 mm thick brass absorber plates and 3.7-9 mm thick plastic scintillator layers. The channel segmentation of the HE is $\Delta\eta \times \Delta\phi \approx 0.087 \times 0.087$ for $|\eta| < 1.6$ and $\Delta\eta \times \Delta\phi \approx 0.17 \times 0.15$ for the remainder of the HE subsystem.

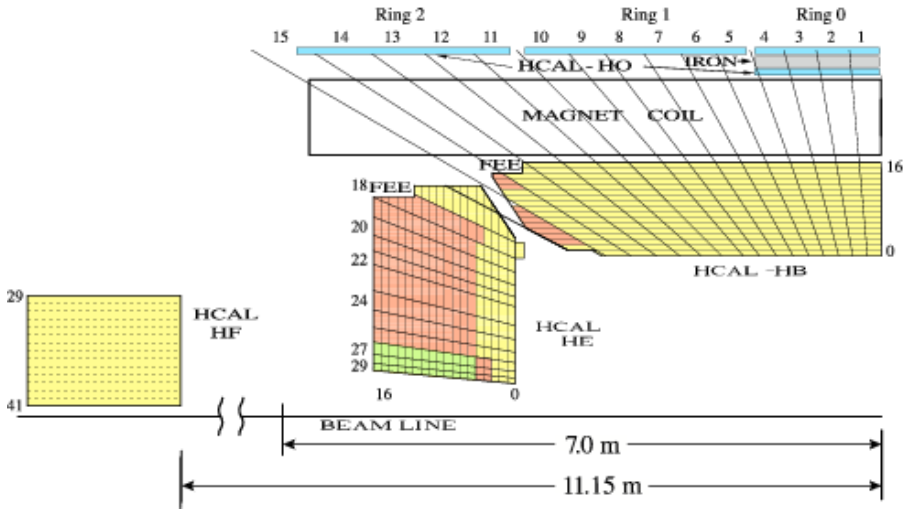

Figure 3.9: Schematic of the CMS HCAL and illustration of its segmentation. HCAL subsystems are also labelled. From Ref. [37]

An additional subsystem is included beyond most of the rest of the detector at the very forward region of $3.0 < |\eta| < 5.0$. It must cope with extremely high particle flux and be very resistant to the resulting high radiation. Long and short quartz fibers are used as the active material. The long fibers cover the full depth of the detector while the short fibers start at a depth of 22 cm from the front of the detector. Both sets of fibers are interleaved with steel absorbers. The quartz fibers capture the Cherenkov light and get read out by a conventional photomultiplier tube (PMT). The channel segmentation of the HF is $\Delta\eta \times \Delta\phi \approx 0.175 \times 0.175$.

The energy resolution for hadrons of the combined calorimeter (both the ECAL and HCAL) has been determined for the barrel as:

$$\frac{\sigma}{E} = \frac{84.7\%}{\sqrt{E[GeV]}} + 7.4\%. \tag{3.10}$$

Separately for the HF, the resolution is:

$$\frac{\sigma}{E} = \frac{198\%}{\sqrt{E[GeV]}} + 9\%. \tag{3.11}$$

Figure 3.10: Photo showing the the Russian Navy shells re-purposed for the CMS HCAL. From Ref. [38]

It is worth mentioning that the author of this thesis spent significant time working on this subsystem. The details of this time can be found in App. A.

3.2.5 Superconducting Magnet

The superconducting magnet was designed to aid in the measurement of high energy muon momenta. For this reason a solenoid was chosen and provides CMS with its namesake. It sits outside the calorimeter subsystems. The solenoid provides large bending power to more accurately determine the momentum of charged particles by bending the particle trajectories in the ϕ direction. This large magnetic field enables measurement of particle momentum and charge even at high energies. Muons with transverse momentum of 1 TeV can then be measured with a momentum resolution of less than 10% [39].

Weighing 220 t, the solenoid is a 4-layer winding of stabilized and reinforced niobium-titanium. The cold mass is cooled to 4.5 K in order to become superconducting. Within this state, it can store an energy of 2.3 GJ and generate a magnetic field of 3.8 T. The 10,000 t iron yoke is used to return this flux. The return yolk is interwoven with

the muon system (discussed in the next section, Sec. 3.2.6). This system focuses the return field within the muon system volume to supply an additional handle on the measurement of high energy muon momenta.

3.2.6 Muon System

Outside the magnet is the muon system. All particles should be stopped by the other subsystems save for muons and other non-interacting particles. A muon, as a long-lived particle, can go through meters of material without interacting. The muon system then has the task of accurate detection of muons. This is important because many interesting physics phenomena feature a muon, or muons, in their signature.

Three separate gaseous detectors compose the muon system: Drift Tubes (DTs), Cathode Strip Chambers (CSCs), and Resistive Plate Chambers (RPCs). As the magnetic field is constant within the barrel, DTs are used in four stations, of 172,000 wires each, and cover $|\eta| < 1.2$. Since the magnetic field changes within the endcaps, 4 CSC stations, of 234 strips each, are employed to identify muons within $0.9 < |\eta| < 2.4$. The RPCs are in both the barrel and endcap regions and are divided into 109,608 strips with widths between 1.95 and 4.10 cm. Fig. 3.11 shows a cross-sectional quarter view of the muon system.

Each DT is filled with an 85% argon and 15% carbon dioxide gas mixture. It is 2.4 m in length and 13 $\times$ 42 mm in cross section. The walls are covered by electrodes at $\sim$1.5 kV and an anode wire runs along the full length of the tube at 3.6 kV. The gas atoms become ionized when a muon passes through a tube. Electronics read out the freed electrons which drift towards the anode along the electric field. The maximum drift time is 380 ns.

Each CSC is composed of alternating cathode strip and anode wire layers. The space between two consecutive planes is filled with a 40% argon, 50% carbon dioxide and 10% tetrafluoromethane gas mixture. Similar to a DT, when a muon passes through a CSC, gas atoms are ionized resulting in ions drifting towards the cathode. The read out

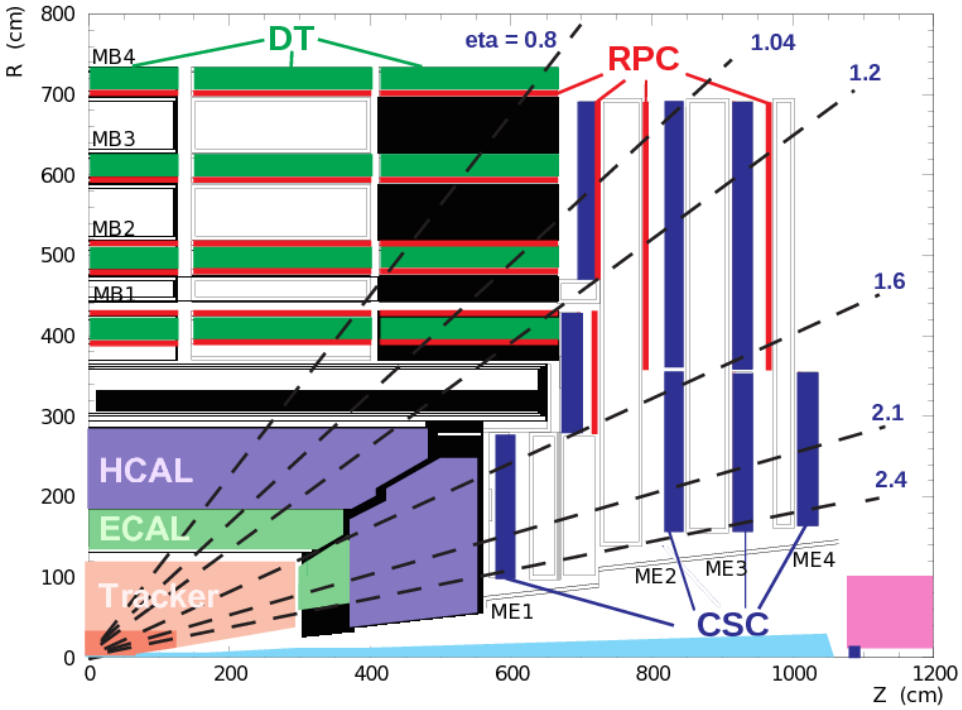

Figure 3.11: Schematic of the CMS muon system with labelled subsystems. From Ref. [39]

also functions the same as in the DTs. An additional measurement provided by the cathode strip read out is the induced charge.

Each RPC consists of parallel-plate detectors based on bakelite. The space between these plates is filled with a 95.2% norflurane, 4.5% butane, and 0.3% sulfur hexafluoride gas mixture. This gas mixture is also kept at a humidity of ∼45% to ensure a constant bakelite resistivity. The RPCs provide a very fast muon measurement, efficiently triggering events with a muon, with a timing resolution of ∼1 ns.

Using only the muon system, the resolution for muons is 15-40% for $p_{\mathrm{T}} = 1$ TeV and down to about 9% for $p_{\mathrm{T}} \gtrsim 200$ GeV. When combining the muon system information with that of the tracker system however, a momentum resolution of 5-10% for $p_{\mathrm{T}} = 1$ TeV and 0.8-2% for $p_{\mathrm{T}} \gtrsim 200$ GeV can be achieved.

3.2.7 Trigger System

Because it is impossible to store and analyze every event that is produced at CMS, the number of events that are recorded must be drastically reduced. This is done before the data is even ready for the offline analysis phase. Thus, the trigger is the first stage of event selection. It can cut down the event rate from 40 MHz to 300 Hz. The rate reduction is achieved in two stages: the Level 1 trigger (L1) and the High Level Trigger (HLT).

3.2.7.1 Level-1 Trigger

The L1 trigger is based on a hardware system of programmable electronics. It is responsible for every event that is collected by CMS. The L1 trigger has 3.2 μs after a bunch crossing to determine if an event will be passed to the HLT, at a total rate of 100 kHz. A schematic of the L1 architecture as of 2015 can be seen in Fig. 3.12.

First, the Trigger Primitive Generators (TPGs) are seeded by deposits in the calorimeters and/or hits in the muon system. The seeded TPGs then calculate the E_{T} sums from the calorimeters and the muon tracks, which are combined into Layer 1 Calo Triggers (L1CTs) or muon track finders, respectively. Based on p_{T} and quality, they are then sorted. The regional information is combined to form the Layer 2 Calo Triggers and the Global Muon Triggers, respectively. Once these triggers determine the best physics object, they are finally combined to form the Global Trigger. The Global Trigger applies the final set of selection criteria to physics objects. At the end, the Global Trigger decides if an event will be kept and further analyzed by the HLT or if it will be discarded.

3.2.7.2 High Level Trigger

The events that pass the L1 trigger algorithms are transmitted on to the HLT where objects are reconstructed closer to the offline method. This enables events which are interesting for offline data analysis to be selected with further identification criteria.

The hardware portion of the HLT is formed by the event filter farm (EVF) of

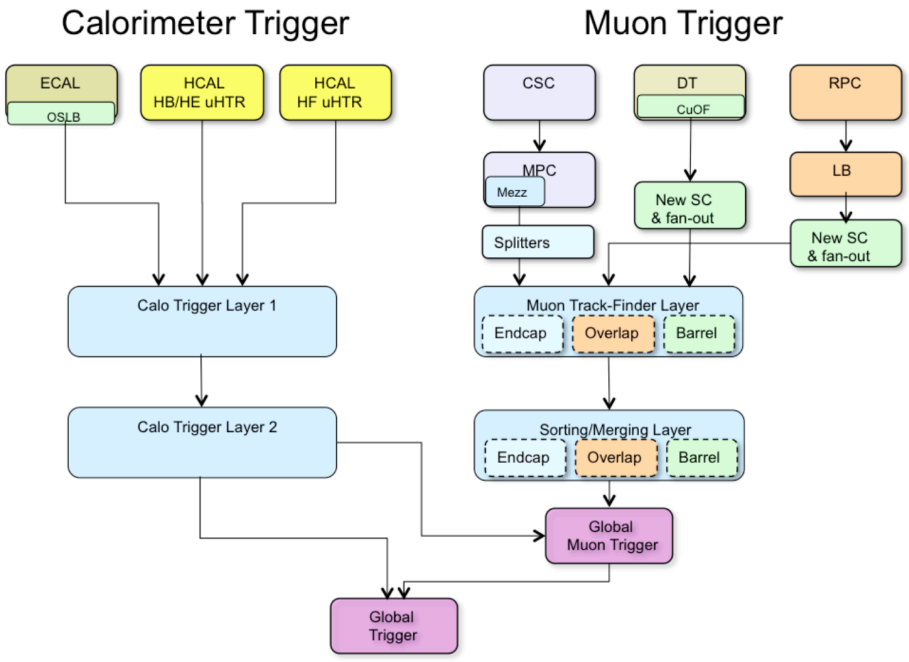

Figure 3.12: Schematic of the CMS L1 trigger system with labelled constituent trigger layers. From Ref. [40]

CPUs with builder and filter units. The EVF consisted of 13,000 CPU cores by the end of 2012. Builder units use the information from the separate sub-detectors to build a complete event picture. Filter units then handle the built event from the builder units to convert the raw data into sub-detector specific data structures. They also perform the actual event reconstruction and trigger decisions. The filter farm uses significant computing resources to manage the input rate of 100 kHz, with an average processing time of up to ∼175 ms per event. The HLT design specification is described in full in [41].

Data is processed at the HLT using sophisticated offline-quality reconstruction algorithms with optimized performance to reduce any dead time. The algorithms are processed in an HLT path which reconstructs and selects physics objects. The order of these algorithms is given by its computational complexity. This reduces the input rate before the computationally expensive reconstruction, such as the particle-flow algorithm (detailed further in Sec. 4.2).

After the complete online reconstruction, the final decision is made to keep or discard an event. The events that are accepted are sent to the storage manager to be held in a local disk, before transferring to the CMS Tier-0 center at CERN for permanent storage and offline processing. The output rate, from 300 to 1000 Hz, of the HLT is limited by the event size and ability for the CERN Tier-0 to process the events. Most events are processed instantaneously.

3.2.8 Summary

CMS reconstructs particles and objects with high efficiency. The arrangement of sub-detectors in CMS and their overall purposes are given in Fig. 3.13. The particles produced in the primary collision travel through the silicon tracker. Here the trajectory and momentum of charged particles is measured. Once past the tracker, electrons and photons produce an electromagnetic shower in the ECAL and stop, giving a measure of their energy. Charged and neutral hadrons continue their shower and produce a hadronic shower in the HCAL, giving a measure of their energy. Lastly, muons will travel through the HCAL and the superconducting solenoid and be detected by the muon system. Since some particles will not be detected by any CMS sub-detectors, such as neutrinos and other neutral and weakly interacting particles, there will be an energy imbalance in the transverse plane. This imbalance forms the missing energy measurement.

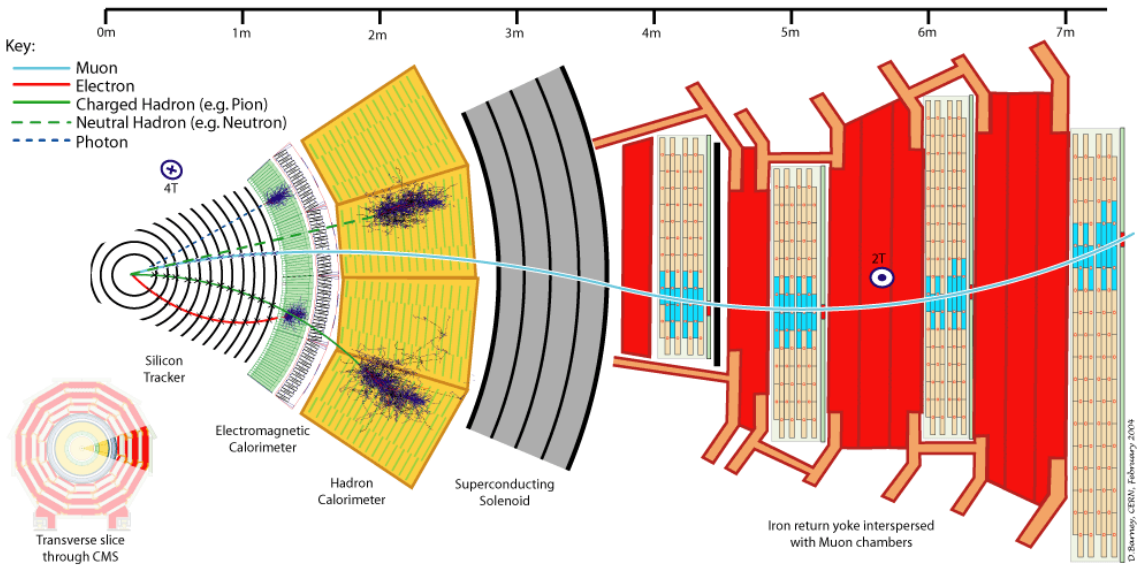

Figure 3.13: A transverse slice of CMS. All particles produced will travel through the silicon tracker. The tracker will measure the trajectory of charged particles and reconstruct the momenta. Next, photons and electrons will shower in the ECAL and deposit all of their energy. Hadrons will continue through the ECAL and produce hadronic showers in the HCAL. Muons will not be stopped by the ECAL or HCAL and will continue through the magnet to the muon system. From Ref. [42]

Chapter 4

Event and Object Reconstruction

The output from CMS is collected and combined to reconstruct physics objects and candidates for particles. This allows for the interpretation of an event and the physics processes involved. This chapter gives an overview of the reconstruction methods used in CMS.

4.1 Track reconstruction

Signals above a noise threshold within the pixel and strip detectors are clustered into hits [43]. These hits are combined among neighboring detector units and the hit center is determined. The hit center is also corrected for the drift of the collected charge caused by the magnetic field. Using a track finder algorithm based on the Kalman filter method, tracks are reconstructed from the hits [44]. The algorithm is applied successively. First only "simple" (e.g. high-p_{T}) tracks are reconstructed, before the algorithm is applied again this time with additional tracks included. This process repeats itself six times to reduce the number of combinatorics needed for the algorithm.

Each iteration of the algorithm is performed in five steps. First a seed is constructed from hits. The minimal information needed to construct a seed are hits which are consistent with a track so that a trajectory can be calculated. Second, the trajectory is ex-

trapolated and compatible hits are added. This track finding is based on the Kalman filter. Third, the reconstructed track is fitted to obtain estimates on its properties, such as momentum. Lastly, the track is subject to quality criteria; any tracks failing this requirement are removed. The full description of this algorithm can be found in Ref. [43].

4.1.1 Primary Vertex reconstruction

The reconstructed tracks are assigned to interaction vertices, primary or secondary. The primary vertex (PV) is the one that comes from the hard scattering in the event. The reconstruction of the primary vertex is the primary focus in this section.

The vertex candidates are formed by groups of tracks separated the least in the z-axis. The candidates' parameters are estimated with an adaptive fit technique. In this technique, each track is assigned a weight factor based on its consistency with the candidate vertex. This weight factor is defined from 0 to 1, where 1 means the tracks are fully consistent with the vertex. A track must have a factor of at least 0.5 in order to be assigned to a vertex. In order to estimate the compatibility of the group of tracks with the candidate vertex, a χ^2 test is used. Finally, an adaptive vertex fit is used to determine the vertex properties (such as position). The vertex with the largest sum of the squared transverse momenta of the assigned tracks and within 24 cm of the center of CMS along the z-axis is chosen as the PV of the event.

4.2 Particle Flow

The Particle Flow (PF) event reconstruction algorithm's purpose is to identify and reconstruct all particles from a collision by using the information from the sub-detectors [45, 46]. This algorithm uses tracks from the tracker and muon systems in addition to calorimeter clusters as input. The calorimeter clusters are seeded by calorimeter cells with local energy maxima. Adjacent cells are added if they pass noise thresholds. The tracks and clusters then link together to form PF blocks. These PF blocks are then fed into the

particle reconstruction and identification algorithm. As an example of the linking, a track trajectory can be extrapolated to the ECAL sub-detector. If a compatible ECAL cluster is found, these two measurements are linked to form a block. This linking also extends to the HCAL and muon sub-detectors. Additional effects and information such as calorimeter shower shapes, are also taken into account at this stage.

The PF algorithm can reconstruct electrons, muons, photons, and charged and neutral hadrons. The rest of this chapter is devoted to describing physics objects used in this thesis. At the end of each section describing a physics object, the identification requirements are given.

4.3 Muon reconstruction

Muons are reconstructed from the tracker and muon sub-detectors only. Because of this, there exist three types:

tracker muons: reconstruction based only on tracker system information,

stand-alone muons: reconstruction based only on muon system information,

global muons: reconstruction based on both tracker and muon systems information.

The stand-alone muon tracks are obtained using the Kalman filter similar to the track finding algorithm. These tracks are then extrapolated to the tracker system to find a compatible track. These two tracks are combined to create the global muon. This global muon reconstruction informs the PF muon algorithm [39]. Since the muon is a long-lived particle, it leaves virtually no deposits in the calorimeters. This information is leveraged to distinguish prompt muons (i.e. promptly after the pp collision) from charged hadrons. The PF muon algorithm is still capable of identifying non-prompt muons. Non-prompt muons can come from, for example, b-quark decays and be inside a jet. These non-prompt muons will not be isolated. This is important to note because this muon energy needs to be

corrected for in the jet energy. The identification efficiency for a PF muon has been found to be $\approx 99\%$ for muons with $p_{\mathrm{T}} < 20$ GeV and 100% for muons with $p_{\mathrm{T}} > 20$ GeV.

For the analysis in this thesis, muons are required to be PF global muons. They must be associated with the PV and pass identification requirements to discriminate them against charged hadrons. The full criteria can be found in Ref. [47]. These muons are from the 'medium' muon selection. In addition muons must have a distance of closest approach to the PV of less than 0.5 mm along the beam axis and 0.2 mm in the transverse plane. Muons must also be isolated, satisfying $I_{\mathrm{mini}} < 0.2$. I_{mini} is an isolation definition where the scalar sum of the p_{T} values of all PF hadrons (neutral and charged) and photons within a ΔR cone (see Eq. 3.5) around the candidate direction is divided by the lepton p_{T}:

$$I_{\mathrm{mini}} = \frac{1}{p_T}\Bigg(\sum_{\mathrm{cone}} p_{\mathrm{T}}(\text{charged hadrons from PV}) + \max\Bigg[0, \sum_{\mathrm{cone}} \mathrm{p}_{\mathrm{T}}^{\mathrm{photons}} + \sum_{\mathrm{cone}} p_{\mathrm{T}}(\text{neutral hadrons}) - \frac{1}{2}\sum_{\mathrm{cone}} p_{\mathrm{T}}(\text{charged hadrons not from PV})\Bigg]\Bigg). \quad (4.1)$$

The ΔR cone size is muon p_{T} dependent: for $p_{\mathrm{T}} < 50$ GeV the size is 0.2, for 50 GeV $\leq p_{\mathrm{T}} \leq 200$ GeV the size is given by 10 divided by the muon p_{T}, and for $p_{\mathrm{T}} > 200$ GeV the size is 0.05. This decreasing cone size is due to the fact that the collimation of a heavy particle's decay products increases as its Lorentz boost also increases. This isolation definition should differentiate muons coming from W or Z boson decays (i.e. prompt) and from b-quark decays (i.e. non-prompt). In this analysis only prompt muons are of interest.

4.4 Electron reconstruction

Electrons are reconstructed from the tracker and ECAL sub-detectors only. They make a track and deposit all their energy in the ECAL. Because of this, electron reconstruction is seeded by two separate quantities: a track, for low-p_{T} electrons, or an ECAL supercluster, for high-p_{T} electrons [48]. The ECAL supercluster is defined as 35×5 cells

wide in the barrel and 5×5 cells wide in the endcaps within $\phi \times \eta$. Using a Gaussian sum filter (GSF), the track, ECAL energy deposit, and track trajectory are reconstructed. However, since the budget material of the tracker is large and it causes many electrons to bremsstrahlung before reaching the ECAL, the GSF includes this information and corrects the electron reconstruction to account for the bremsstrahlung photon emissions and change in electron momentum and trajectory. The track trajectory and momentum and ECAL deposit location and energy must be consistent. To distinguish electrons from charged hadrons, the HCAL deposit energy divided by the ECAL deposit energy must be small in addition to the shower shape along η in the ECAL. The identification efficiency for electrons then is measured to be between 80 and 99% depending on the electron identification requirements made [49].

For the analysis in this thesis, electrons are not allowed to be in $1.442 < |\eta| < 1.566$, which is the ECAL barrel-endcap transition region. The full criteria for the 'Veto' electron selection can be found in Ref. [50]. Electrons must also be isolated, like muons and also use the I_{mini} definition in Eq. 4.1. Electrons are required to have $I_{\text{mini}} < 0.1$.

4.5 Photon reconstruction

Much like electrons, the photon reconstruction algorithm is based on ECAL superclusters [51]. Photons also face the same large material budget of the tracker, and in this case, they can convert to e^+e^- pairs before reaching the ECAL. The algorithm searches for two oppositely charged tracks inside an ECAL supercluster that are compatible with a photon decay. Photons that mimic electron candidates are rejected. In order to distinguish photons from neutral hadrons (e.g. π^0), a narrow shower shape is required. Since the shower shape is independent of the magnetic field, it is a good discriminator. In addition there must be low HCAL deposits compared to the ECAL signal, otherwise the candidate is taken to be a neutral hadron. The identification efficiency for reconstructed photons is measured to be $\gtrsim$ 90 (85) % for photons in the ECAL barrel (endcaps) [52].

For the analysis in this thesis, photons, like electrons, are not allowed to be in $1.442 < |\eta| < 1.566$, which is the ECAL barrel-endcap transition region. In addition photons must have $p_{\mathrm{T}} > 20$ GeV and be within $|\eta| < 2.4$. Photons are required to be isolated, where the isolation is based on greatly restricting the energy from PF candidates around a ΔR cone of 0.3 around the photon. The full criteria for the 'Loose' photon selection can be found in Ref. [53].

4.6 Jet reconstruction

As previously stated, jets are clusters of hadrons coming from the decay of quarks or gluons. The anti-k_{T} algorithm takes these clusters as input [54]. For a pair of particles of i and j, three distance parameters are determined:

$$d_{ij} = \min(p_{\mathrm{T,i}}^{-2}, p_{\mathrm{T,j}}^{-2}) \, \frac{(\phi_1 - \phi_2)^2 + (y_i - y_j)^2}{R^2} \, , \tag{4.2}$$

$$d_{i,(j)} = p_{\mathrm{T,i(j)}}^{-2} \, , \tag{4.3}$$

where $y = \frac{1}{2} \ln \left(\frac{E+p_z}{E-p_z} \right)$ is the rapidity and R the clustering radius. This R parameter is chosen to be 0.4. First, the algorithm is given the full list of PF particles. For each clustering step, the three distance parameters, d_i, d_j, and d_{ij}, are calculated. Objects i and j are clustered into a new object, k, and are removed if the minimum of the three distance parameters is the d_{ij} parameter. The new object k is then added to the particle list. If any d_i (d_j) parameter is the minimum, object i (j) is removed from the particle list and is defined to be a jet. This algorithm continues until there is no object left in the particle list. The algorithm must also be infrared- and collinear-safe, as the decaying parton can emit soft gluons or split into multiple collinear sub products. This ensures the reconstructed jet does not change in momentum [55]. For this thesis, an additional requirement is made on the particles in the algorithm: charged particles not coming from the PV are removed from

the jet. This is called charged-hadron subtraction (CHS) and reduces the effect PU has on the jet energy [56].

The jet clustering must take into account detector measurements which are artificial in nature due to noise signals. In order to keep noise signals from faking jets, identification criteria on the hadronic, electromagnetic and charged energy fractions is applied. These requirements and the rest of the 'loose' jet identification requirements can be seen in Tab. 4.1 [57]. An exception is made if the jet is within a ΔR cone of 0.04 of an isolated lepton, photon, or track: the jet does not need to pass the 'loose' jet identification requirements. This is done because the jet identification requirement is applied to filter out jets arising from anomalous sources. Lastly, jets are required to be within the range of the tracker, $|\eta| < 2.4$, as well as have $p_{\mathrm{T}} > 30$ GeV.

Table 4.1: Loose jet identification criteria.

ID variable	Requirement
Number of PF constituents	> 1
Number of charged PF constituents	> 0
Neutral hadron fraction	< 0.99
Neutral electromagnetic fraction	< 0.99
Charged hadron fraction	> 0
Charged electromagnetic fraction	< 0.99

Unfortunately, the measured energy of a jet using the full detector information does not usually equal the "true" energy of the parton that produced the jet [58]. This is due to a variety of factors and there are a few corrections to the jet energy made. The first correction accounts for PU effects from the jet energy. Because the PU effects are to first-order uniformly distributed, the PU energy is subtracted from the jet energy. The second and third corrections account for the p_{T} and η dependent jet response. For data, a small residual is applied to correct for differences in data and simulation. The total jet energy correction is found to be between 0.5 and 4% for the analysis presented in this thesis.

4.6.1 b-quark identification

Because many SUSY models predict a light squark third-generation leading to enhanced production of b-quarks, identifying jets coming from the hadronization of b-quarks (i.e. b-jets) is particularly critical to be sensitive to those models. Jets arising from b- or c-quark (called heavy-flavor) hadronization can be distinguished from u-, d-, or s-quark or gluon jets (called light-flavor). This can be done because the heavy-flavor quarks have relatively large masses and lifetimes, ensuring their decay a short distance away from their origin. The daughter particle tracks then point to a secondary vertex close to but not at the PV. Several algorithms are used in CMS to identify b-jets [59, 60].

In this analysis, the combined secondary vertex version2 (CSVv2) algorithm is used. As the name implies, the algorithm leverages secondary vertex and track lifetime information. The secondary vertex is reconstructed with the Inclusive Vertex Fitter (IVF) which is described in detail in Ref. [61]. The IVF algorithm clusters tracks around seeding tracks. The clusters are then fitted to a common vertex. A vertex with tracks compatible with the K_s^0 mass is rejected. Any vertices that share at least 70% of their tracks with each other are merged. Lastly, based on significance and compatibility, all tracks are assigned to the primary vertex or secondary vertices. With this secondary vertex information as well as the tracks in a jet and their impact parameter, the CSVv2 forms a likelihood fit. This likelihood fit outputs a discriminator with good efficiency.

A b-jet tag efficiency of $\sim$68% can be achieved for a light-flavor rejection of 99%. The corresponding c-jet misidentifying rate is $\sim$15%. This is true for the 'medium' working point of the CSVv2 tagger, thus a jet that passes this selection is defined to be a b-jet. Both the b-jet tagging and misidentifying efficiencies are a function of the jet p_T and η. An illustration of these two efficiencies in simulation are given in Fig. 4.1 as a function of jet p_T only.

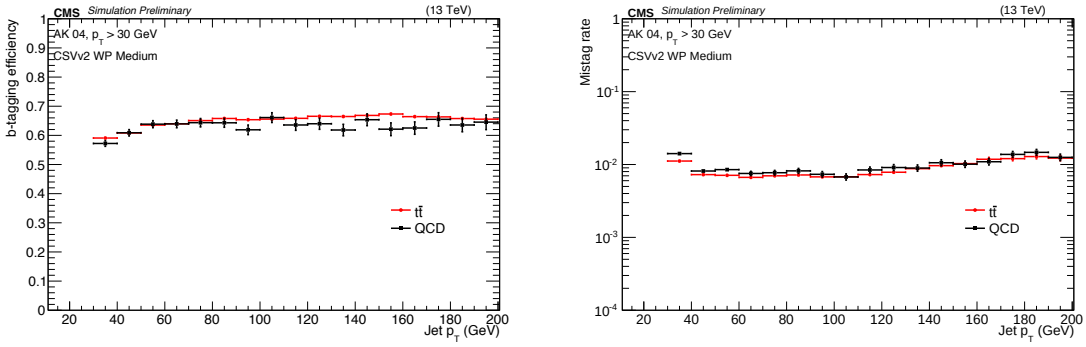

Figure 4.1: The b-jet tagging efficiency (left) and light-flavor mistagging rate (right) as a function of jet p_{T} for the medium CSVv2 working point. Simulated $t\bar{t}$ and QCD multijet (see Sec. 5.2) events are shown in red and black respectively. From Ref. [62].

4.7 Missing energy reconstruction

The energy imbalance left behind by undetected particles is the missing energy of the event. Practically, this is measured as the missing transverse momentum of the event. As noted previously, the transverse component is used as the initial transverse energy of the parton-parton system is nearly zero, while the momenta along the beam axis is unknown. The negative vectorial sum of all particles in the event then define:

$$\vec{E}_{\mathrm{T}}^{\mathrm{miss}} = -\sum_{\mathrm{particles}} \vec{p}_{\mathrm{T}}. \tag{4.4}$$

The particle information can come from the calorimeter only or involve the full PF algorithm, though it is usually the latter. For the analysis in this thesis, a simpler version of missing energy is used. Since the search is for all-hadronic events, jets are the principal measurement tool. Owing to this, a new quantity, $H_{\mathrm{T}}^{\mathrm{miss}}$, is defined:

$$H_{\mathrm{T}}^{\mathrm{miss}} = \left| \sum_{\mathrm{jets}} \vec{p}_{\mathrm{T}} \right|. \tag{4.5}$$

This missing transverse hadronic activity variable is computed from jets as defined in Sec. 4.6. But, the jet definition in Sec. 4.6 only includes jets within the tracker acceptance of the detector. Because the missing energy variable needs to be calculated with as

much information as possible, jets out to the detector limit of $|\eta| = 5$ must also be included in this sum. With this in mind, the jet identification requirements are modified and reduced for these jets, as shown in Tab. 4.2. An advantage to the $H_{\mathrm{T}}^{\mathrm{miss}}$ variable is that since it is composed of only jets, the jet energy corrections are also included in its calculation. This means no additional corrections due to detector response or noise are needed.

Table 4.2: The jet identification criteria used in the $H_{\mathrm{T}}^{\mathrm{miss}}$ calculation for the jets outside the tracker acceptance, $|\eta| > 2.4$.

ID variable	Requirement	
	$2.4 < \|\eta\| < 3.0$	$3.0 < \|\eta\| < 5.0$
Number of PF constituents	> 1	Not applied
Neutral hadron fraction	< 0.99	Not applied
Neutral electromagnetic fraction	< 0.99	< 0.90
Number of neutral PF constituents	Not applied	> 10

Part III

Search for New Physics in all-hadronic events

Chapter 5

Search for Supersymmetry in all hadronic events

This chapter describes the SUSY search strategy using a pp collision data sample collected by the CMS experiment at $\sqrt{s} = 13$ TeV. The data sample corresponds to an integrated luminosity of 2.3 fb^{-1}.

This study [63] combines and extends search strategies developed for the analysis of CMS data collected at $\sqrt{s} = 8$ TeV during the LHC Run 1: the study from Ref. [64] which used b-jet multiplicity but not jet multiplicity as a search variable with the study from Ref. [65] which used jet multiplicity but not b-jet multiplicity as a search variable. Both these studies focused on all-hadronic events. The search presented here is now a unified study combining both strategies from LHC Run 1 which results in a better, more sensitive search.

5.1 Data and Simulation Samples

5.1.1 Data Samples

Data collected by the CMS experiment is stored in different primary datasets. The primary datasets are defined by the triggers that fired in a given event. For this analysis the `HTMHT` dataset is used to define the signal regions. These datasets are fed by triggers based on H_{T} and $H_{\mathrm{T}}^{\mathrm{miss}}$ or their combination, so called "cross triggers." If an event passes one of the triggers that defines the primary dataset, the event is stored in that primary dataset. A given event, because it can fire more than one trigger, can be stored in several primary datasets. The various primary datasets used in this analysis is shown in Tab. 5.1.

Table 5.1: Data samples with a total integrated luminosity of $2.3\,\mathrm{fb}^{-1}$ used in the search. The samples are divided by their use is the signal region or a control region.

Dataset	Region
`HTMHT`	signal
`SingleElectron`	Z$\to \nu\bar{\nu}$ (control)
`SingleMuon`	had. τ & $Z \to \nu\bar{\nu}$ (control)
`SinglePhoton`	Z$\to \nu\bar{\nu}$ (control)

5.1.2 Background Simulation Samples

To study the backgrounds, simulated samples of the following Standard Model processes are used: $t\bar{t}$, single-top production, W+jets, Quantum Chromodynamics (QCD) multijet production, Z $\to \nu\bar{\nu}$, γ + jets, Z/γ^* (Drell-Yan), as well as much smaller rare backgrounds such as diboson and associated higgs boson production. $t\bar{t}$, W+jets, QCD multijet production, Z $\to \nu\bar{\nu}$, and γ + jets are simulated by the MadGraph5 event generator. The powheg v1.0 program is used for the t and tW channel single-top processes. Relatedly, the MadGraph5_mc@nlo program generates events for the s channel single-top process, in addition to the rare backgrounds. The full detector simulation with Geant4 is used to trace particles through the detector and to model the detector response. These simulated

datasets are normalized to next-to-leading or next-to-next-to-leading-order cross sections, according to the calculations currently available. To model the effects of PU, or more the number of interactions in an event, the simulation is generated with a nominal distribution of PU. It is then corrected to match the observed distribution in data. A full list of these samples, along with their cross sections, can be found in App. B.

5.1.3 Signal Simulation Samples

This analysis uses 'Simplified Model Spectra' or SMS [66] as signal samples. These SMS scenarios are purposefully designed for simple topologies of new physics, with relatively few particles and can be described by a minimum set of parameters including sparticle masses. The production cross sections only depend on sparticle masses and they decline rapidly with increasing sparticle mass. Additionally, because the sparticle masses depend on how SUSY breaking occurs, the sparticle masses cannot be predicted. This is why inclusive searches with sensitivity to a wide range of sparticle masses, such as this one, are performed.

Each SMS topology comprises of pair production of sparticles. The sparticles can then decay directly to a SM particle or through an intermediate decay involving one or more other sparticles. Since only R-parity conserving models are considered, all decay chains will end in the production of the LSP. A SMS topology is then interpreted with the results to obtain limits based on the product of the cross section and branching fraction as a function of sparticle masses, if no evidence for new physics is found.

There are four distinct signal samples all of which feature gluino ($\tilde{g}$) pair production. The first three samples has each gluino decay into a quark and off-shell squark. The off-shell squark then decays into a quark and the lightest neutralino. Since flavor is conserved, the final decay products of the gluino are a quark-antiquark pair along with the neutralino. The first sample has each gluino decay into $b\bar{b}\widetilde{\chi}_1^0$ (via an intermediary off-shell $\tilde{b}$), the second into $t\bar{t}\widetilde{\chi}_1^0$ (via an intermediary off-shell $\tilde{t}$), and the third into $q\bar{q}\widetilde{\chi}_1^0$ (via an intermediary off-shell $\tilde{q}$) where each q here is any non-third generation (s)quark. The last

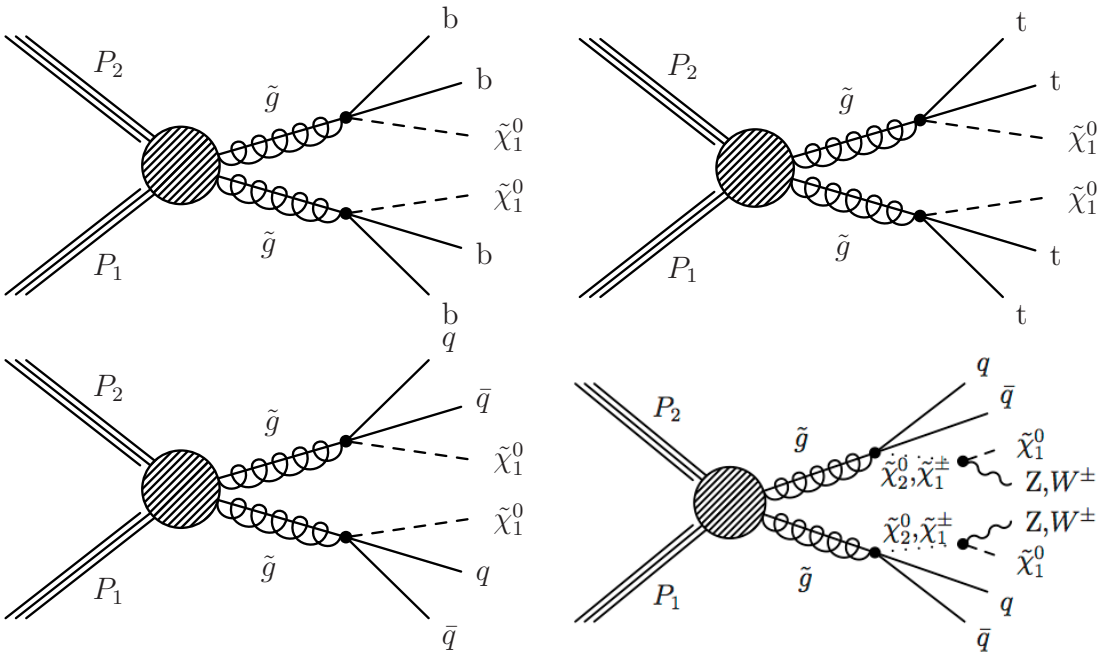

Figure 5.1: Event diagrams for the four signal samples. The top left is the T1bbbb scenario, the top right is the T1tttt scenario, the bottom left is the T1qqqq scenario, the bottom right is the T5qqqqVV scenario. The lightest neutralino, $\tilde{\chi}_1^0$, is assumed to be the LSP.

sample also has each gluino decay into a non-third generation quark and corresponding off-shell squark. This off-shell squark decays, with an even 1/3 probability for each, to the next-to-lightest neutralino $\tilde{\chi}_2^0$, or to a lightest-chargino state $\tilde{\chi}_1^\pm$. The $\tilde{\chi}_2^0$ ($\tilde{\chi}^\pm$) then decays to the $\tilde{\chi}_1^0$ and to a Z ($W^\pm$). These four scenarios are known as T1bbbb, T1tttt, T1qqqq, and T5qqqqVV respectively. Also note that these scenarios scan the gluino mass-neutralino mass plane. Example diagrams of each of these four processes can be seen in Fig. 5.1.

5.2 Background sources

There are several backgrounds to searches of this type and can be summed broadly into three categories: background from top quark decays and W+jets, from QCD multijet, and from $Z \to \nu\bar{\nu}$ events. The first two are reducible backgrounds. In other words, their signatures are significant enough from the signal signature that they can be reduced by a cut or cuts. The latter, $Z \to \nu\bar{\nu}$, is an irreducible background because it produces genuine

missing energy and can be difficult or impossible to reduce with a cut. In this analysis, cuts such as jet multiplicity can help in decreasing the $Z \to \nu\overline{\nu}$ background. These three backgrounds contribute to the signal region:

1. from top quark decays and W+jets because of the leptonic decay of the W boson, which yields large hadronic energy, a neutrino (real missing energy) and a non-vetoed lepton. The non-vetoed leptons can fail the electron or muon veto requirements and make it into the signal region. This type of background is known as 'lost leptons.' The other reason for the non-vetoed leptons is from the hadronic decay of a tau. This makes two separate backgrounds to model and predict from top and W+jets events: the lost lepton and hadronic τ backgrounds;

2. from strong interaction multijet events (also known as QCD) because of the mismeasurement of jet p_{T}. If a jet p_{T} is mismeasured, then fake missing energy will be created in the event. This can happen due to jet resolution effects. An sdditional source of fake missing energy is if an event has a charm or bottom quark decay semileptonically;

3. from $Z \to \nu\overline{\nu}$ because of the production of a Z in association with jets with the subsequent decay of the Z to two neutrinos (real missing energy). This can result in both large hadronic activity and missing energy.

The backgrounds are predicted by data-driven estimation methods and will be discussed in detail the next chapter.

5.3 Event Selection

5.3.1 Search variables

The variables used in this study are:

- Jet multiplicity, N_{jet}: with jet requirements $p_{\mathrm{T}} > 30$ GeV, $|\eta| < 2.4$, and pass 'loose' jet identification requirements, see Sec. 4.6

- Hadronic energy, H_{T}: $H_{\mathrm{T}} = \sum_{\mathrm{jets}} p_{\mathrm{T}}$, where the jets must pass the jet selection defined above

- Missing energy, $H_{\mathrm{T}}^{\mathrm{miss}}$: $H_{\mathrm{T}}^{\mathrm{miss}} = |\sum_{\mathrm{jets}} \vec{p_{\mathrm{T}}}|$, with the η restriction of the jets used in the calculation loosened to $|\eta| < 5$; see full definition in Sec. 4.7

- b-jet multiplicity, $N_{\text{b-jet}}$: jets which satisfy the jet requirement for N_{jet} as well as pass the CSVv2 b-tagging algorithm medium working point, see Sec. 4.6.1

- Muon veto: muon candidate requires $p_{\mathrm{T}} > 10$ GeV, $|\eta| < 2.4$, and $I_{\mathrm{mini}} < 0.2$, in addition to passing the medium muon selection defined in Sec. 4.3; an event is vetoed if a muon satisfies these requirements

- Electron veto: electron candidate requires $p_{\mathrm{T}} > 10$ GeV, $|\eta| < 2.5$ and $I_{\mathrm{mini}} < 0.1$, in addition to passing the veto electron selection defined in Sec. 4.4; an event is vetoed if an electron satisfies these requirements

- Isolated track veto: isolated charged-particle track requires $p_{\mathrm{T}} > 10$ GeV (5 GeV if the track is identified as an electron or muon candidate by PF), $|\eta| < 2.4$, and

  - $m_{\mathrm{T}} < 100$ GeV, with $m_{\mathrm{T}}(\mathrm{tk}, E_{\mathrm{T}}^{\mathrm{miss}}) = \sqrt{2 p_{\mathrm{T}}^{\mathrm{tk}} E_{\mathrm{T}}^{\mathrm{miss}} (1 - \cos\Delta\theta)}$ where $p_{\mathrm{T}}^{\mathrm{tk}}$ is the transverse momentum of the track and $\Delta\theta$ is the azimuthal distance between the track and missing energy vector. This requirement is done to reject events where the track and $H_{\mathrm{T}}^{\mathrm{miss}}$ are consistent with a leptonic W decay. This also helps preserve signal efficiency.

  - $I_{\mathrm{tk}} < 0.1$ (0.2 if the track is identified as an electron or muon candidate), with $I_{\mathrm{tk}} = \sum_{\mathrm{cone}} p_{\mathrm{T}}(\text{other tracks})/p_{\mathrm{T}}^{\mathrm{tk}}$ where the p_{T} sum is of all the other tracks within a ΔR cone of 0.3 around the track under consideration. The sum is then divided by the track p_{T}. This defines the isolation requirement for tracks.

  An event is vetoed if an isolated track satisfies these requirements.

- Angular $\Delta\phi_{\text{min}}$ cut: $\Delta\phi(\text{j}_i, H_{\text{T}}^{\text{miss}}) > (0.5, 0.5, 0.3, 0.3)_{i=1,2,3,4}$, the four highest-$p_{\text{T}}$ jets within a certain radian of the $H_{\text{T}}^{\text{miss}}$ vector in the azimuthal coordinate results in an event rejection

- Event cleaning: Various event filters are applied, such as any event that has a jet failing the 'loose' jet identification requirement and missing energy filters which detect events with spurious energies

5.3.2 Baseline selection

This section defines the search's baseline signal selection amongst the variables that have been defined in the previous section. Fig. 5.2, 5.3, and 5.4 show $N-1$ style plots of the search variables after applying the baseline selection. That is, the plotted variable is the only variable whose baseline cut, if needed, is not applied, while all others are applied. Tab. 5.2 shows the event counts of the backgrounds with the sequential application of the signal region requirements. The baseline selection is then:

- $N_{\text{jet}} \geq 4$: since the focus of this study is on gluino pair production, at least four jets are required;

- $H_{\text{T}} > 500$ GeV: this helps select events with lots of hadronic activity;

- $H_{\text{T}}^{\text{miss}} > 200$ GeV: this helps select events with potential signal and removes events with spurious $H_{\text{T}}^{\text{miss}}$;

- Muon and electron vetoes: the SUSY signal samples in this analysis do not contain any leptons and the vetoes reduce the top-quark and W+jets background since these processes produce at least one charged lepton;

- Isolated track veto: this event veto helps eliminate hadronically decaying τ leptons as well as non-identified electrons or muons.

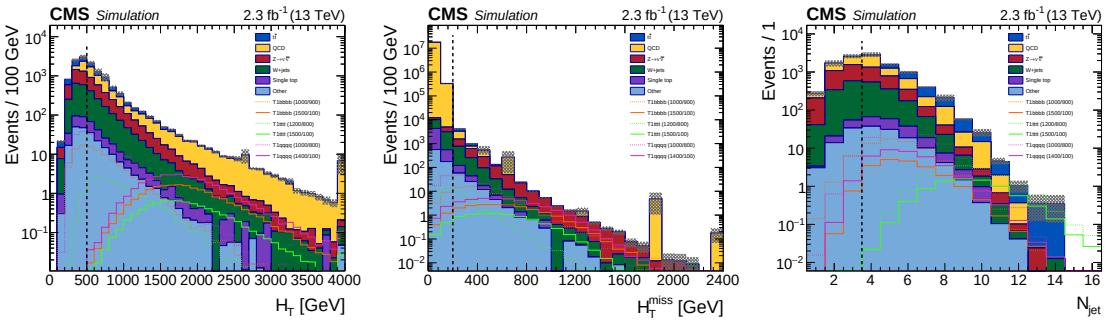

Figure 5.2: $N-1$ style plots of H_{T}, $H_{\mathrm{T}}^{\mathrm{miss}}$, and N_{jet}. Example signal points are shown in solid and dashed lines with particular gluino and LSP masses respectively for a few of the signal scenarios. Vertical black dashed lines indicate the minimum threshold required in each variable.

- $\Delta\phi_{\mathrm{min}}$ cut: this event veto helps eliminate QCD multijet events.

The following sets the full search binning. Using four exclusive search variables, 72 search bins are created:

- N_{jet}: 4-6, 7-8, $\geq$9;
- $N_{\mathrm{b\text{-}jet}}$: 0, 1, 2, $\geq$3;
- H_{T}: 500-800, 800-1200, $\geq$ 1200 GeV;
- $H_{\mathrm{T}}^{\mathrm{miss}}$: 200-500, 500-750, $\geq$750 GeV.

The bins with $H_{\mathrm{T}} < 800$ GeV and $H_{\mathrm{T}}^{\mathrm{miss}} > 750$ GeV are not used in the analysis as this is unphysical. Because $H_{\mathrm{T}}^{\mathrm{miss}}$ cannot exceed H_{T}, low numbers of events are expected at high $H_{\mathrm{T}}^{\mathrm{miss}}$, so an additional two bins are merged into their neighbors. For $500 < H_{\mathrm{T}}^{\mathrm{miss}} < 750$ GeV, a larger $500 < H_{\mathrm{T}} < 1200$ GeV is created. Similarly, for $H_{\mathrm{T}}^{\mathrm{miss}} > 750$ GeV a cut of $H_{\mathrm{T}} > 800$ GeV is also created. These two super bins (bin numbers 4 and 6 respectively) can be seen in Fig. 5.5. The relative importance of each background source can be seen in a binned subspace, $N_{\mathrm{jet}} \cdot N_{\mathrm{b\text{-}jet}}$, of the search space in Fig. 5.6.

Table 5.2: The cutflow and expected yields at $2.3\,\text{fb}^{-1}$ for Standard Model backgrounds, with the baseline selection. The simulation results are scaled using the cross sections listed in App. B. The efficiency of each cut, calculated with respect to the previous cut, is given in parentheses after the expected yield.

Cut	Other	Single top	W+jets	$Z \to \nu\bar{\nu}$	QCD	$t\bar{t}$	Total
Start	2×10^5	3×10^5	5×10^6	1×10^6	$> 10^9$	2×10^6	$> 10^9$
N_{jet} >3	2×10^4	9×10^4	5×10^5	5×10^4	$> 10^8$	1×10^6	$> 10^8$
H_{T} >500	5×10^3	1×10^4	7×10^4	1×10^4	$> 10^7$	2×10^5	$> 10^7$
$H_{\text{T}}^{\text{miss}}$ >200	683	991	7081	2271	25244	10098	46368
μ veto	458 (0.671)	658 (0.663)	4984 (0.704)	2268 (0.999)	25109 (0.995)	6717 (0.665)	40195 (0.867)
e veto	275 (0.600)	376 (0.572)	3033 (0.608)	2250 (0.992)	24891 (0.991)	4012 (0.597)	34837 (0.867)
μ track veto	263 (0.956)	353 (0.938)	2881 (0.950)	2245 (0.997)	24742 (0.994)	3722 (0.928)	34205 (0.982)
e track veto	236 (0.897)	311 (0.882)	2566 (0.891)	2224 (0.991)	24441 (0.988)	3252 (0.874)	33030 (0.966)
Had track veto	179 (0.760)	223 (0.715)	1850 (0.721)	2181 (0.981)	23748 (0.972)	2488 (0.765)	30669 (0.929)
$\Delta\phi_{\text{min}}$ cuts	106 (0.591)	92 (0.414)	1007 (0.545)	1482 (0.679)	3529 (0.149)	1222 (0.491)	7438 (0.243)
Evt. Cleaning	104 (0.980)	90 (0.977)	981 (0.974)	1473 (0.994)	2336 (0.662)	1186 (0.971)	6170 (0.830)
$N_{\text{b-jet}}$ bins							
$N_{\text{b-jet}}$ =0	64 (0.615)	20 (0.219)	803 (0.819)	1200 (0.815)	1528 (0.654)	225 (0.190)	3839 (0.622)
$N_{\text{b-jet}}$ =1	25 (0.243)	44 (0.493)	154 (0.157)	228 (0.155)	419 (0.179)	538 (0.454)	1409 (0.228)
$N_{\text{b-jet}}$ =2	12 (0.115)	23 (0.254)	22 (0.022)	41 (0.028)	372 (0.159)	363 (0.306)	832 (0.135)
$N_{\text{b-jet}}$ ≥3	3 (0.027)	3 (0.034)	2 (0.002)	4 (0.003)	18 (0.008)	60 (0.051)	90 (0.015)

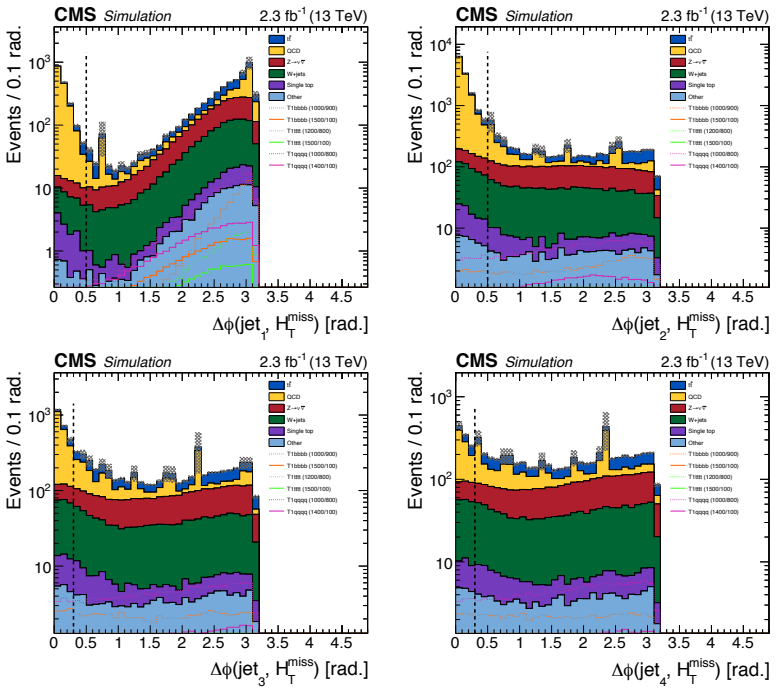

Figure 5.3: $N-1$ style plots of the four $\Delta\phi$ cuts. Example signal points are shown in solid and dashed lines with particular gluino and LSP masses respectively for a few of the signal scenarios. Vertical black dashed lines indicate the minimum threshold required in each variable.

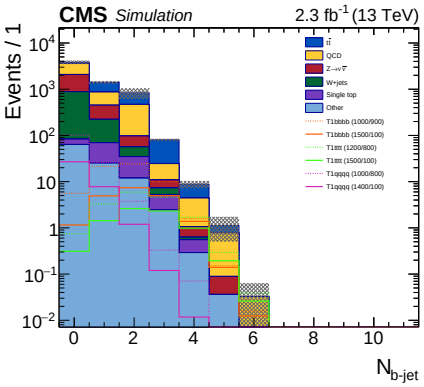

Figure 5.4: Plot of $N_{\text{b-jet}}$ after the baseline selection. Example signal points are shown in solid and dashed lines with particular gluino and LSP masses respectively for a few of the signal scenarios. Note there is no $N_{\text{b-jet}}$ requirement in the baseline selection.

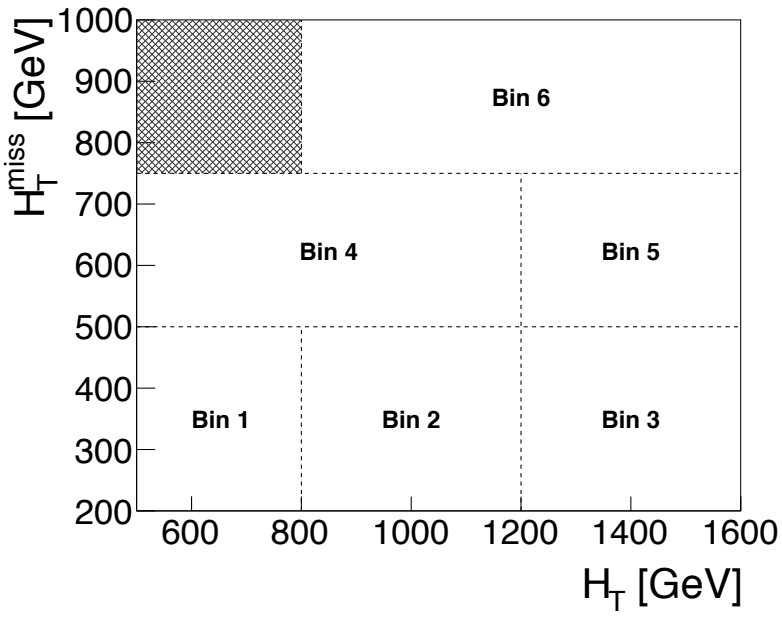

Figure 5.5: An illustration of the H_{T}-$H_{\mathrm{T}}^{\mathrm{miss}}$ plane search binning showing the six search intervals.

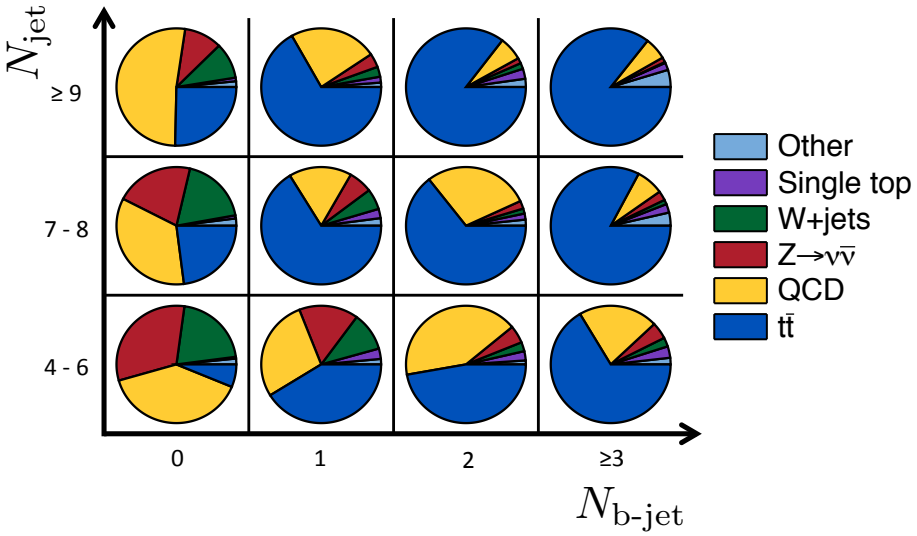

Figure 5.6: The relative expected contributions from each SM background for the baseline signal selection in bins of N_{jet} and $N_{\mathrm{b\text{-}jet}}$, while integrating over the H_{T} and $H_{\mathrm{T}}^{\mathrm{miss}}$ bins.

5.3.3 Triggers

The search in this analysis uses events that pass the `HLT_PFHT350_PFMET00_*` trigger. This trigger requires an on-line calorimeter-only H_{T} and $E_{\mathrm{T}}^{\mathrm{miss}}$ to be above 350 GeV and 100 GeV respectively. The efficiency of this trigger can be computed by using an orthogonal trigger, `HLT_Ele27_eta2p1_WPLoose_Gsf_*`, as the denominator and the main signal trigger as the numerator in the efficiency calculation. Using a selection of $N_{\mathrm{jet}} > 3$ and a single electron as the base sample, the efficiency simply becomes the fraction of base events that pass the main trigger. The efficiency of the main trigger as a function of the offline H_{T} and $H_{\mathrm{T}}^{\mathrm{miss}}$ can be seen in Fig. 5.7. The efficiency is measured to be greater than 98% in the baseline selection. However, small inefficiencies are observed in the $H_{\mathrm{T}}^{\mathrm{miss}}$ (right plot of Fig. 5.7), while the H_{T} efficiency is significantly above the offline H_{T} plateau. Because of this, the efficiency in the second and fourth $H_{\mathrm{T}}^{\mathrm{miss}}$ bins, corresponding to 200 $< H_{\mathrm{T}}^{\mathrm{miss}} <$ 500 GeV and $H_{\mathrm{T}}^{\mathrm{miss}} >$ 500 GeV, is measured and is shown in the Tab. 5.3

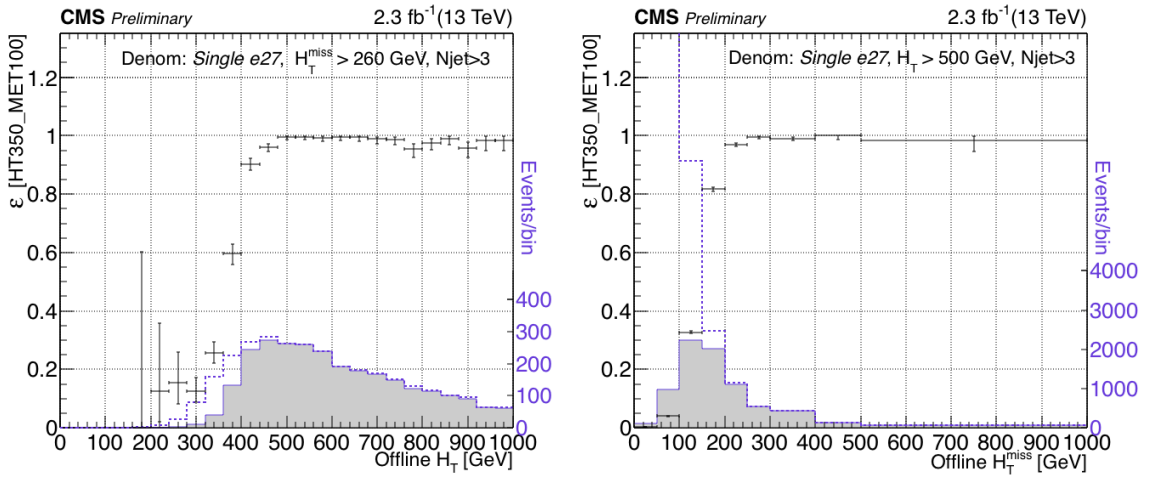

Figure 5.7: The trigger efficiency as a function of the search variables, showing the H_{T} on the left and the $H_{\mathrm{T}}^{\mathrm{miss}}$ on the right. For the left plot, the $H_{\mathrm{T}}^{\mathrm{miss}}$ is required to be above 260 GeV to ensure full efficiency of the $E_{\mathrm{T}}^{\mathrm{miss}}$ component of the trigger. Similarly for the right plot, the the H_{T} is required to be above the baseline selection of 500 GeV.

It is worth noting that the trigger efficiency as a function of the $H_{\mathrm{T}}^{\mathrm{miss}}$ should be

Table 5.3: The estimated fraction of signal events with an H_{T} greater than 500 GeV and $N_{\mathrm{jet}} > 3$ that pass the main trigger. Both statistical and systematic uncertainities are shown.

$H_{\mathrm{T}}^{\mathrm{miss}}$ range [GeV]	Efficiency
200-500	$0.9819^{+0.0028}_{-0.0033}(\mathrm{stat.}) \pm 0.0129(\mathrm{syst.})$
500+	$0.9833^{+0.0138}_{-0.0047}(\mathrm{stat.}) \pm 0.0001(\mathrm{syst.})$

affected by how the $H_{\mathrm{T}}^{\mathrm{miss}}$ is created. That is, if the the missing energy is actually from invisible particles or from jet mismeasurement as is the case in QCD events. Thus, another plot of trigger efficiency as a function of $H_{\mathrm{T}}^{\mathrm{miss}}$ is made á la Fig. 5.7 but in a QCD dominated control sample. This control sample is made by simply flipping the angular $\Delta\phi_{\mathrm{min}}$ cut. An inefficiency is observed as can be seen in Fig. 5.8. This trigger efficiency is also measured and is only applied to simulated QCD events when comparing the QCD simulation to data, e.g. in data-simulation plots. Note this implies, this does not enter the analysis directly. This trigger efficiency can be seen in Tab. 5.4

Table 5.4: The estimated fraction of signal events with an H_{T} greater than 500 GeV and $N_{\mathrm{jet}} > 3$ that pass the main trigger in a QCD dominated control region. Statistical uncertainties are shown.

$H_{\mathrm{T}}^{\mathrm{miss}}$ range [GeV]	Efficiency
200-250	$0.7316^{+0.0078}_{-0.0080}(\mathrm{stat.})$
250-300	$0.8041^{+0.0111}_{-0.0115}(\mathrm{stat.})$
300-400	$0.8348^{+0.0134}_{-0.0143}(\mathrm{stat.})$
400-500	$0.8734^{+0.0220}_{-0.0025}(\mathrm{stat.})$
500+	$0.8195^{+0.0343}_{-0.0000}(\mathrm{stat.})$

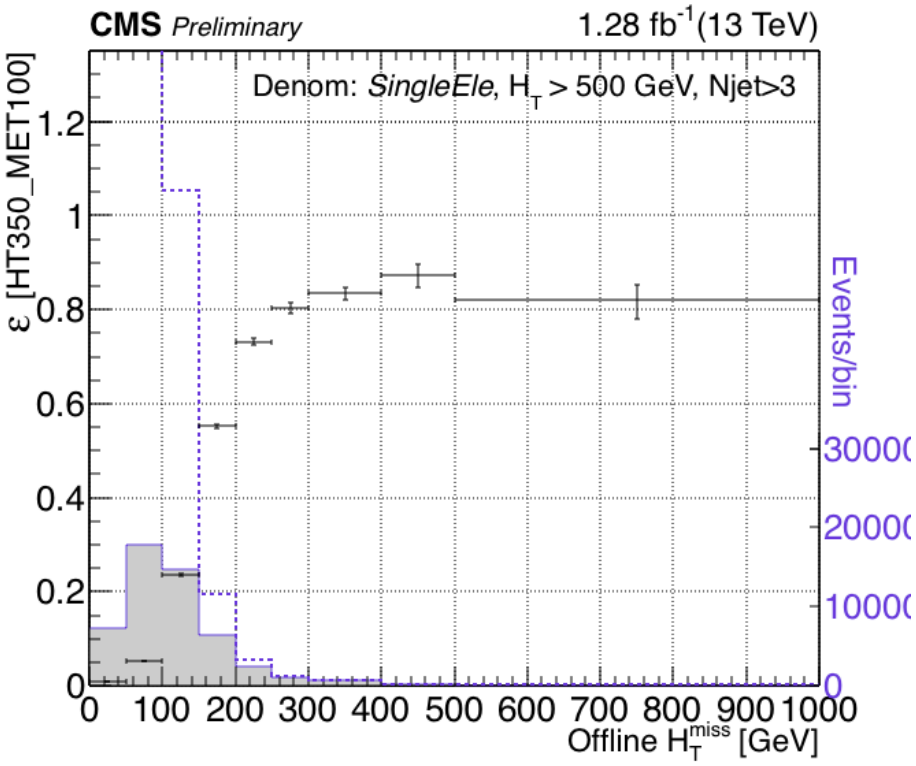

Figure 5.8: The trigger efficiency as a function of the $H_{\mathrm{T}}^{\mathrm{miss}}$ in a QCD dominated control region with an offline $H_{\mathrm{T}} > 500$ GeV.

Chapter 6

Background Estimates

The key component in any search is the robust and dependable estimation of the (SM) background in the signal region. As has been discussed in Sec. 5.2, there are three major sources of background in this analysis: leptonic decays from the W boson in top-quark and W+jets processes, missing energy from neutrinos from the decay of the Z boson in Z+jets processes, and strong interaction multijet processes (QCD). This chapter is devoted to these backgrounds and the methods to estimate their size.

6.1 The top and W+jets background

The biggest background in this analysis, the top-quark and W+jets events account for about half of the total background, when integrating over all search bins. Looking at Fig. 5.6, for larger values of N_{jet} and $N_{\text{b-jet}}$ this fraction grows past 90%. Recall that this background primarily is a result of a W boson decaying leptonically. This decay yields a neutrino, which is real missing energy, and a lepton. These types of events can appear in the signal region if the lepton does not get vetoed. These non-vetoed leptons can be electrons or muons that do not satisfy electron or muon selection requirements, as defined in Sec. 5.3.1 (i.e. 'lost leptons') or hadronically decaying taus. These two non-vetoed lepton categories form the two separate evaluations of this background.

6.1.1 Lost-lepton estimation method

Top-quark and W+jets events with electrons or muons can reach and fulfill the requirements for the signal region as the lost-lepton background if the electron or muon does not meet these requirements: kinematic acceptance, reconstruction or isolation (Fig. 6.1).

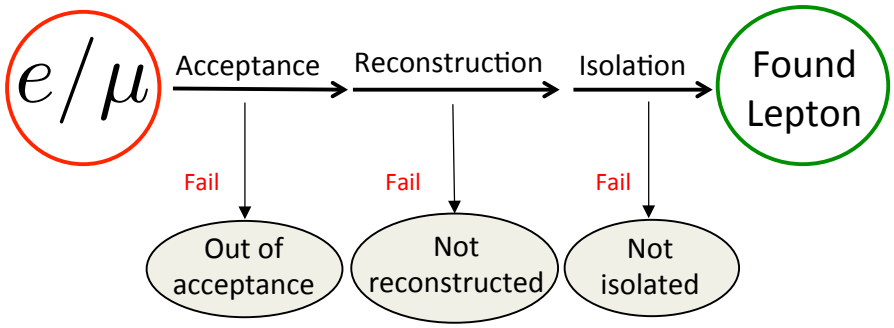

Figure 6.1: An illustration of the steps required for an electron or muon to be described as such. If the electron or muon do not satisfy these requirements, they are considered 'lost' and are a background in the signal region.

The data-driven method to evaluate the lost-lepton background is to create single-lepton Control Samples (CS) in the data analogous to the signal region but inverting the electron and muon vetoes, and weighting these events with a probability for them to appear within the signal region. These weight factors are calculated by the efficiencies for each step shown in Fig. 6.1. These weighted CS events, within the 72 signal bins, then define the prediction made by this method. Two separate CS are selected then: the single electron CS, where exactly one electron is required and the single muon CS, where exactly one muon is required. Note the isolated track veto is not applied to either of the two CS but all other selection criteria are applied. Also note the m_{T} restriction is applied as is in the single-lepton CS, except swapping the track with the lepton in question, as is defined in Sec. 5.3.1. This is done to minimize signal contamination of the CS. In addition, it maintains consistency with the reasoning behind the creation of single-lepton CS: to select W boson decays to

a lepton-neutrino pair. Recall the lepton vetoes are meant to reject events where the W decays leptonically.

The lepton efficiencies are determined from simulated events of $t\bar{t}$, W+jets, single top and other rare processes (see App. B). To calculate the acceptance efficiency, exactly one muon (electron) is selected via generator-level information. This muon (electron) must be associated with the hard interaction of the event. The generator-level muons (electrons) that pass or fail the kinematic p_{T} and η criteria then comprise the acceptance efficiency calculation, which can be seen in Fig. 6.2. If a muon (electron) passes the acceptance requirement, it is matched to a reconstructed muon (electron). The number of muons (electrons) that pass or fail the reconstruction matching criteria then comprise the reconstruction efficiency calculation, which can be seen in Fig. 6.3. This procedure is then repeated again for the isolation efficiency calculation, which can be seen in Fig. 6.4. The events that pass the isolation requirement are then used to determine the m_{T} selection efficiency, again similar to the procedure just outlined.

Dilepton events can contribute to both the signal region, if both leptons are lost, or the single-lepton CS, if one of the two leptons is lost. The dileptonic events add to the lost lepton background of the signal region, but only represent 2% of the lost lepton events. This contribution is calculated in a similar way to lepton efficiency procedure outlined above, with the difference that the acceptance, reconstruction, and isolation efficiencies are combined into a single efficiency. For these dilepton events, two generator-level leptons are required. The dileptonic contamination of the single-lepton CS is handled by applying a correction to the CS to remove this contamination.

Lastly, a correction is applied for the isolated track veto. This correction is obtained for each of the electron, muon, and pion tracks, within all signal bins. This efficiency is calculated by dividing the number of events after applying the lepton veto and track veto by the number of events after the lepton veto. This scaling factor reduces the background prediction. An additional correction is applied for electrons, as the single-electron CS shows an impurity from non-prompt (i.e. not promptly after the pp collision) electron decays. The

resulting purity is 96% and is used as the correction factor. No such impurity is observed for muons, as its purity exceeds 99%, so no correction is needed.

A critical choice is how to parameterize the lepton efficiency maps. A variety of choices are available and all have been thoroughly investigated: Tab. 6.1 summarizes what the parameterization choices are for each lepton efficiency map. The only parameter not introduced yet is Activity, which is a variable that measures the energy around the lepton, summing up the PF candidates' p_{T} in an annulus around the lepton divided by the lepton p_{T}.

Table 6.1: The specific parameterizations for the various lepton efficiency calculations.

Efficiency	Parameterization
Lepton acceptance	H_{T}, $H_{\mathrm{T}}^{\mathrm{miss}}$, and N_{jet}
Lepton reconstruction	lepton p_{T} and Activity
Lepton isolation	lepton p_{T} and Activity
single-electron CS purity	$H_{\mathrm{T}}^{\mathrm{miss}}$ and N_{jet}
m_{T} selection	H_{T} and N_{jet}
dilepton contamination of single-lepton CS	N_{jet}
dilepton contribution to signal region	N_{jet}
isolated track veto	H_{T}, $H_{\mathrm{T}}^{\mathrm{miss}}$ and N_{jet}

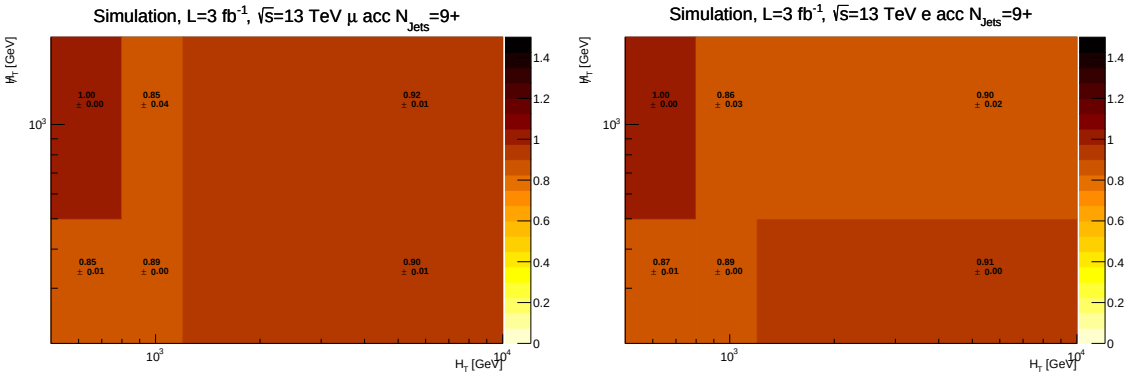

Figure 6.2: Muon (left) and electron (right) acceptance efficiency maps binned in H_{T} and $H_{\mathrm{T}}^{\mathrm{miss}}$ for $N_{\mathrm{jet}} = 9+$.

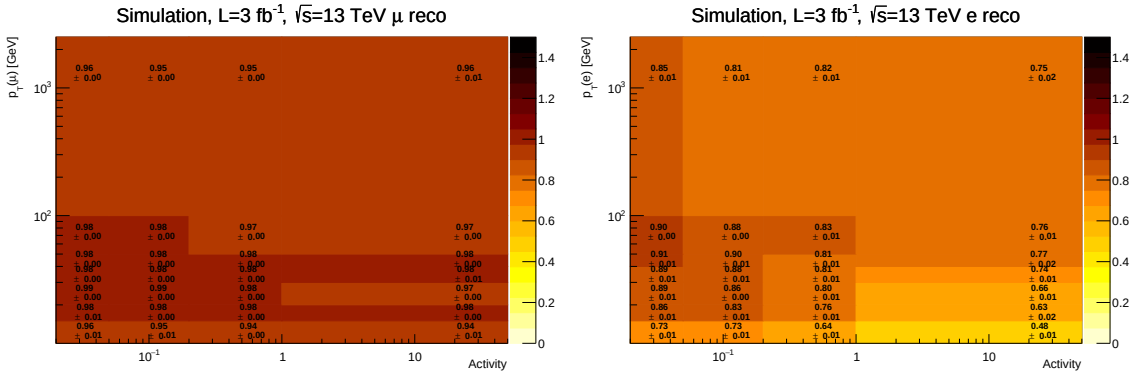

Figure 6.3: Muon (left) and electron (right) reconstruction efficiency maps binned in Activity and lepton p_{T}.

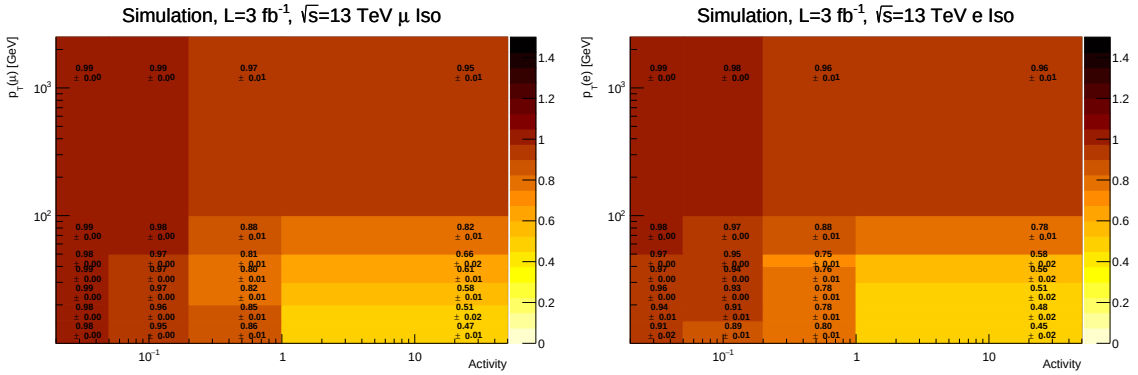

Figure 6.4: Muon (left) and electron (right) isolation efficiency maps binned in Activity and lepton p_{T}.

6.1.1.1 Lost-Lepton prediction method

The calculations used to make the lost-lepton prediction are given here. This section defines, for criterion X (acceptance, reconstruction, and isolation), the term $!\mathrm{X}^{\mathrm{lepton}}$, which is the applied weight for criterion X for a lepton and $\epsilon_{\mathrm{X}}^{\mathrm{lepton}}$, which is the efficiency of criterion X for a lepton. To estimate the non-isolated muons, the single-muon CS is weighted by:

$$!\mathrm{Iso}^{\mu} = N_{\mathrm{CS}}^{\mu} \cdot \frac{1 - \epsilon_{\mathrm{Iso}}^{\mu}}{\epsilon_{\mathrm{Iso}}^{\mu}}. \tag{6.1}$$

Next, the unreconstructed muons are modeled, taking the muon isolation efficiency into

account:

$$!\text{Reco}^{\mu} = N^{\mu}_{\text{CS}} \cdot \frac{1}{\epsilon^{\mu}_{\text{Iso}}} \cdot \frac{1-\epsilon^{\mu}_{\text{Reco}}}{\epsilon^{\mu}_{\text{Reco}}}. \tag{6.2}$$

Lastly, the out-of-acceptance muons are modeled, again taking into account the muon isolation and reconstruction efficiencies:

$$!\text{Acc}^{\mu} = N^{\mu}_{\text{CS}} \cdot \frac{1}{\epsilon^{\mu}_{\text{Iso}}} \cdot \frac{1}{\epsilon^{\mu}_{\text{Reco}}} \cdot \frac{1-\epsilon^{\mu}_{\text{Acc}}}{\epsilon^{\mu}_{\text{Acc}}}. \tag{6.3}$$

The lost electrons can also be modeled using the single-muon CS. Lepton universality guarantees the W boson to decay with equal probability to either an electron or muon which means lost electrons can also be modeled using the single-muon CS (and vice versa). The following relations then define the non-isolated, unreconstructed, and out-of-acceptance electrons, respectively:

$$!\text{Iso}^{\text{e}} = \text{N}^{\mu}_{\text{CS}} \cdot \frac{1-\epsilon^{\text{e}}_{\text{Iso}}}{\epsilon^{\mu}_{\text{Iso}}} \cdot \frac{\epsilon^{\text{e}}_{\text{Reco}}}{\epsilon^{\mu}_{\text{Reco}}} \cdot \frac{\epsilon^{\text{e}}_{\text{Acc}}}{\epsilon^{\mu}_{\text{Acc}}}; \tag{6.4}$$

$$!\text{Reco}^{\text{e}} = N^{\mu}_{\text{CS}} \cdot \frac{1}{\epsilon^{\mu}_{\text{Iso}}} \cdot \frac{1-\epsilon^{e}_{\text{Reco}}}{\epsilon^{\mu}_{\text{Reco}}} \cdot \frac{\epsilon^{e}_{\text{Acc}}}{\epsilon^{\mu}_{\text{Acc}}}; \tag{6.5}$$

$$!\text{Acc}^{\text{e}} = N^{\mu}_{\text{CS}} \cdot \frac{1}{\epsilon^{\mu}_{\text{Iso}}} \cdot \frac{1}{\epsilon^{\mu}_{\text{Reco}}} \cdot \frac{1-\epsilon^{e}_{\text{Acc}}}{\epsilon^{\mu}_{\text{Acc}}}. \tag{6.6}$$

The dilepton contribution to the lost-lepton prediction is modeled as follows:

$$\text{Lost}^{\text{dilep}} = N^{\mu}_{\text{CS}} \cdot (1-\epsilon^{\text{purity}}_{\text{monolep}}) \cdot \frac{1-\epsilon^{\text{found}}_{\text{dilep}}}{\epsilon^{\text{found}}_{\text{dilep}}}, \tag{6.7}$$

where $(1-\epsilon^{\text{purity}}_{\text{monolep}})$ is the number of dilepton events with exactly one lost lepton and $N^{\mu}_{\text{CS}} \cdot (1-\epsilon^{\text{found}}_{\text{dilep}})/\epsilon^{\text{found}}_{\text{dilep}}$ is the probability to also lose the second lepton. With these equations

in place, the total number of lost leptons can be calculated as:

$$\text{Total Lost Leptons} = \epsilon_{\text{isotrk}} \cdot \sum_{i=e,\mu} \left[\frac{[\epsilon_e^{\text{purity}}]}{\epsilon_{m_{\text{T}}}^i} \cdot \left(\epsilon_{\text{monolep}}^{\text{purity}} \cdot \left(!\text{Iso}^i + !\text{Reco}^i + !\text{Acc}^i \right) + \text{Lost}^{dilep} \right) \right], \tag{6.8}$$

where the $\epsilon_{m_{\text{T}}}^i$ term accounts for the m_{T}-selection efficiency, the ϵ_{isotrk} term accounts for the probability that an event passes the isolated track veto, and (only for electrons) the $\epsilon_e^{\text{purity}}$ term accounts for the CS purity. The same procedure outlined for the single-muon CS is also repeated for the single-electron CS, giving two independent predictions. The arithmetic mean of these two predicted values is then the final prediction for the lost-lepton background. A background method can be tested by applying a closure test: determining how well the method can predict the number of background events when applied to simulated events. This closure test of the method can be found in Fig. 6.5.

6.1.1.2 Method Uncertainties

The dominant uncertainty in the method is due to the limited statistics of the CS. Any differences in Fig. 6.5 larger than the statistical uncertainty on that difference is taken as a systematic uncertainty. An additional systematic uncertainty is taken from the lepton acceptance due to parton distribution functions (PDFs), which are used in the simulation of the samples. Smaller systematic uncertainties from the purity of the CS, lepton reconstruction, lepton isolation, and isolated track veto efficiencies are also assigned.

6.1.2 Hadronically decaying τ estimation method

A template technique is used to model the hadronic τ decay (τ_h) from top-quark and W+jets processes. Here, a Control Sample (CS) from single muons is again used; however, using a separate data trigger: a muon-H_{T} one. This trigger, `HLT_Mu15_IsoVVVL_PFHT350_*`, selects events with online H_{T} of 350 GeV and muon p_{T} of 15 GeV. Offline, a single muon is

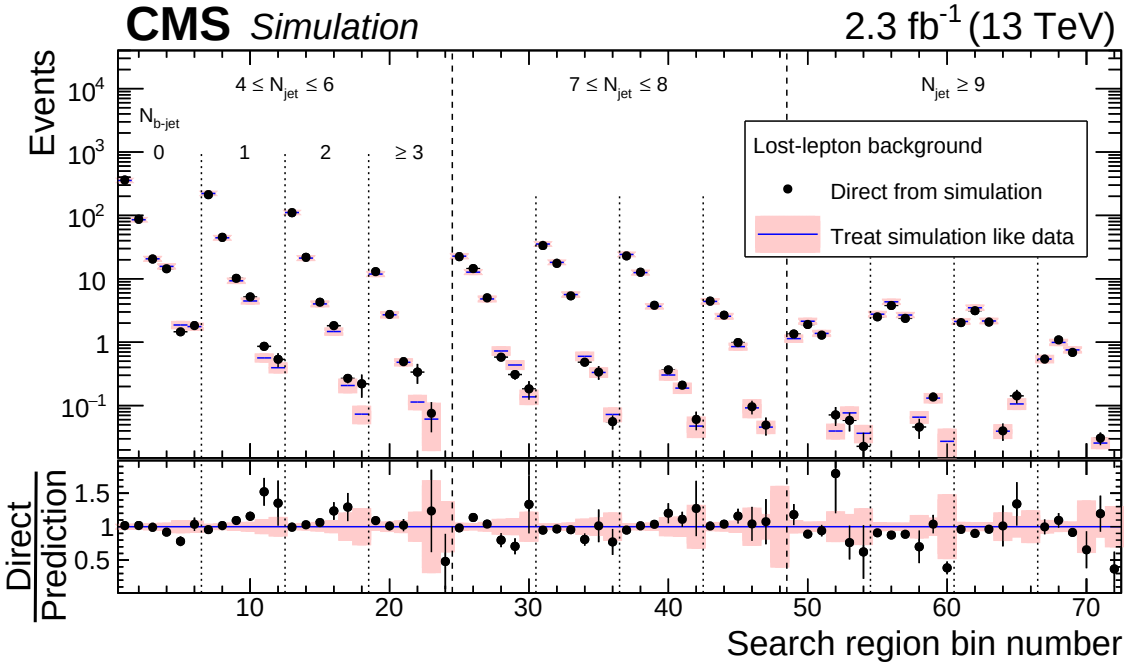

Figure 6.5: Comparison of the lost lepton prediction to the simulated event expectation in the 72 exclusive search bins. The black points are simulated events and the pink histograms are the predictions from the lost lepton method, both with statistical uncertainties. The six bins within each dashed line refer to the six kinematic regions of H_{T} and $H_{\mathrm{T}}^{\mathrm{miss}}$, as seen in Fig. 5.5. Overall, there is reasonable agreement between the prediction and the expectation. The simulation makes use of $t\bar{t}$, W+jets, single-top, Drell-Yan, and other rare SM event samples listed in App. B.

required with criteria $p_{\mathrm{T}} > 20$ GeV and $|\eta| < 2.1$ with all other reconstruction and isolation criteria of Sec. 5.3.1. In addition, the CS must also not have any electrons and have an m_{T} less than 100 GeV. This m_{T} requirement is applied for the same reasons as the lost lepton method: reduce signal contamination and keep consistency with the control sample $\mathrm{W} \to \ell\nu$ hypothesis. This muon-H_{T} trigger is fully efficient for the main analysis variables and is 95% for muons. This number is corrected for in the method. Notice this CS is different from the single-muon CS used in the lost-lepton prediction.

This CS is dominated by $t\bar{t}$ and W+jets decaying to $\mu\nu$+jets. The fact that μ+jets and τ_h+jets both come about because of the same underlying process means both sets of events should also have identical hadronic components excepting detector response

differences among muons and taus. The basic method then is to smear, or scale, the p_{T} of the muon from the CS with response functions taken from simulated events, otherwise known as the 'templates,' in order to mimic a τ_{h} response. The main kinematic variables, such as H_{T}, then must be recomputed and the signal selections reapplied.

The templates, dependent on tau p_{T}, are taken from simulated $t\bar{t}$ and W+jets events. A reconstructed jet is matched, according to ΔR, to a generator-level τ_{h} with the same criteria as the offline muon in the CS. Then the ratio of the respective p_{T} values is made, with the reconstructed jet p_{T} divided by its matched generator-level τ_{h} p_{T}: $p_{\mathrm{T},\tau_h\text{-reco}}/p_{\mathrm{T},\tau_h\text{-gen}}$. These distributions for several different generator-level τ_{h} p_{T} intervals are shown in Fig. 6.6. The distributions in Fig. 6.6 then are the tau response templates. This response template models the visible energy fraction of the tau decay. In other words, all the energy except the daughter neutrinos is considered.

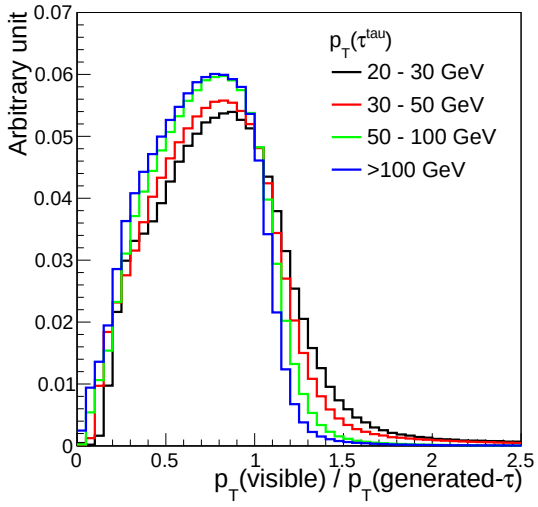

Figure 6.6: Plot of the τ_h response templates. Specifically these are distributions of the $p_{\mathrm{T},\tau_h\text{-reco}}/p_{\mathrm{T},\tau_h\text{-gen}}$ ratio in intervals of $p_{\mathrm{T},\tau_h\text{-gen}}$ from simulated $t\bar{t}$ and W+jets events.

6.1.2.1 Hadronic tau decay prediction method

For each event in the CS, the muon p_{T} is smeared by the tau response templates. This is accomplished by choosing the correct $p_{\mathrm{T},\tau_h\text{-gen}}$ interval, and thus its template, according to the muon p_{T}. This p_{T} value is then scaled by the tau response by randomly sampling the response template. After this smearing effect is applied, all kinematic variables of the event are recalculated, e.g. H_{T}, $H_{\mathrm{T}}^{\mathrm{miss}}$, N_{jet}, etc. A weight factor is then used to determine the contribution of each event to a signal bin. Further, a weight is also calculated to account for the misidentification of a tau as a b-jet. Because some of the muons in the CS come from $\mathrm{W} \to \tau\nu_\tau \to \mu\nu_\mu\bar{\nu}_\tau\nu_\tau$ events and not directly from the W boson as this method assumes, there is contamination of the CS. This is a non-negligible effect and can range from 12-40%. The method takes this contamination and corrects for it accordingly. The corrections used in this method are listed in Tab. 6.2.

Table 6.2: The specific corrections made to hadronic tau decay estimate.

Correction	Term	Parameterization
Ratio of branching fractions	$\frac{\mathcal{B}(W\to\tau_h\nu)}{\mathcal{B}(W\to\mu\nu)} = 0.6476 \pm 0.0024$ [67]	(constant)
Muon acceptance efficiency	$\epsilon^{\mu}_{\mathrm{Acc}}$	H_{T}, $H_{\mathrm{T}}^{\mathrm{miss}}$, N_{jet}
Muon reconstruction and isolation efficiency	$\epsilon^{\mu}_{\mathrm{Reco}}$ and $\epsilon^{\mu}_{\mathrm{Iso}}$	p_{T} and Activity
m_{T} selection efficiency	$\epsilon^{\mu}_{m_{\mathrm{T}}}$	H_{T}, $H_{\mathrm{T}}^{\mathrm{miss}}$, and N_{jet}
CS trigger efficiency	$\epsilon^{\mu}_{\mathrm{Trig}}$	(constant)
CS contamination from $W \to \tau\nu_\tau \to \mu\nu_\mu\bar{\nu}_\tau\nu_\tau$ events	$1 - f_{\tau\to\mu}$	H_{T}, $H_{\mathrm{T}}^{\mathrm{miss}}$, and N_{jet}
dilepton contamination of CS	$1 - f_{\ell\ell}$; $f_{\ell\ell} = 0.02$	(constant)
isolated track veto efficiency	$\epsilon_{\mathrm{isotrk}}$	H_{T}, $H_{\mathrm{T}}^{\mathrm{miss}}$ and N_{jet}

The muon acceptance, reconstruction, and isolation efficiencies are the same ones used in the lost-lepton background method. Combining all weights and terms together, the total τ_{h} background is given by:

$$N_{\tau_\mathrm{h}} = \sum_{i}^{N_\mathrm{CS}^{\mu}} \left(\sum_{j}^{\text{Template bins}} \left(P_{\tau_\mathrm{h}}^{\mathrm{resp}} \sum_{k} w_{\text{b-mistag}}^{\tau_\mathrm{h}} \right) \mathcal{C} \right), \tag{6.9}$$

$$\mathcal{C} = \frac{\epsilon_{\mathrm{isotrk}}}{\epsilon_{\mathrm{Trig}}^{\mu} \epsilon_{\mathrm{Reco}}^{\mu} \epsilon_{\mathrm{Iso}}^{\mu} \epsilon_{\mathrm{Acc}}^{\mu} \epsilon_{m_\mathrm{T}}^{\mu}} (1 - f_{\tau \to \mu})(1 - f_{\ell\ell}) \frac{\mathcal{B}(W \to \tau_\mathrm{h} \nu)}{\mathcal{B}(W \to \mu\nu)}, \tag{6.10}$$

where the first sum is over the single-muon CS events, the second sum is over the response template ($P_{\tau_\mathrm{h}}^{\mathrm{resp}}$), and the third sum is for misidentified τ_h jets as b-jets. Term $\mathcal{C}$ combines and applies the corrections from Tab. 6.2. A closure test of the prediction, similar to the lost lepton method, can be found in Fig. 6.7.

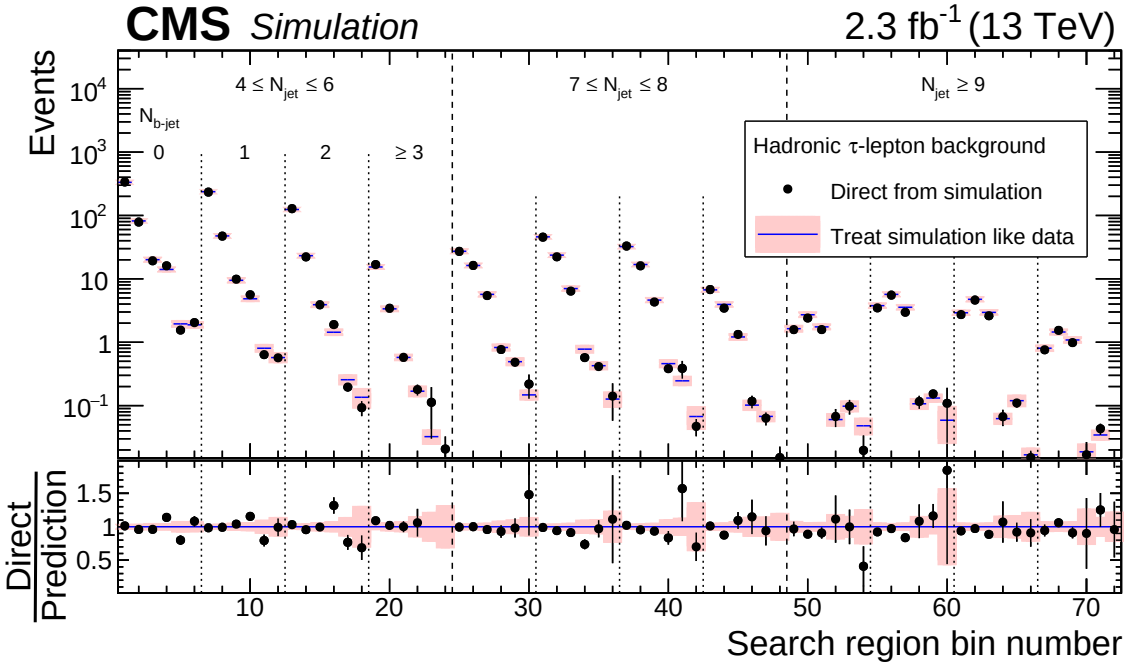

Figure 6.7: Comparison of the τ_h prediction to the simulated event expectation in the 72 exclusive search bins. The black points are simulated events and the pink histograms are the predictions from the lost lepton method, both with statistical uncertainties. The six bins within each dashed line refer to the six kinematic regions of H_T and $H_\mathrm{T}^{\mathrm{miss}}$, as seen in Fig. 5.5. Overall, there is reasonable agreement between the prediction and the expectation. The simulation makes use of $t\bar{t}$, W+jets, single-top, Drell-Yan, and other rare SM event samples listed in App. B.

6.1.2.2 Method Uncertainties

Similar to the lost lepton method, the τ_h method's dominant uncertainty comes from the limited statistics of the CS. Also, differences in Fig. 6.7 larger than the statistical uncertainty on that difference is taken as a systematic uncertainty. Additional systematic uncertainties evaluated are muon acceptance, the response functions, and the misidentification of τ_h jets as b-jets.

6.2 The $Z \to \nu\overline{\nu}$ background

There are two techniques to predict the irreducible $Z \to \nu\overline{\nu}$ background which contains real missing energy due to the production of neutrinos. The first is to simply select $Z \to \ell^+\ell^-$ ($\ell \equiv e, \mu$) events and remove both charged leptons to emulate the $Z \to \nu\overline{\nu}$ process. Using these event yields, with corrections, a prediction of the $Z \to \nu\overline{\nu}$ background can be made. However, a significant restraint to this method is the small $Z \to \ell^+\ell^-$ branching fraction, which is needed to correct the event yield for the prediction. The ratio of $Z \to \ell^+\ell^-$ to $Z \to \nu\overline{\nu}$ branching fractions is approximately $\frac{1}{3}$ [67]. This also means the control sample is a few times smaller than the background. The second technique is to use the similarity in radiation from the Z boson and photons and select γ + jets events as a control sample to predict the $Z \to \nu\overline{\nu}$ background. The two processes are not exactly the same of course, as there are threshold effects from the Z boson as well as coupling differences amongst Z bosons and photons.

A Z+jets CS is selected using an alternate trigger than the one used to select signal events. In this region, the `HLT_Mu15_IsoVVVL_PFHT350_v*` and its electron counterpart `HLT_Ele15_IsoVVVL_PFHT350_v*` triggers select for events with at least one muon or electron with $p_T > 15$ GeV and $H_T > 350$ GeV. The γ + jets CS is selected using an alternate trigger as well: here the `HLT_Photon90_CaloIdL_PFHT500_v*` trigger requires an event to have a photon with $p_T > 90$ GeV and $H_T > 500$ GeV.

The prediction method uses the γ + jets CS to estimate the event yields in the 18

signal bins for $N_{\text{b-jet}} = 0$ (recall there are 72 signal bins in total and 4 bins in the $N_{\text{b-jet}}$ search dimension; see also Fig. 5.5). This is done because of the differences in heavy-flavor production between γ + jets and Z+jets processes. A correction is applied, if necessary, by comparing the γ + jets CS bins to the $\text{Z} \to \ell^+\ell^-$ CS event yields in the low-N_{jet} bins to account for any potential physics differences. For the signal bins with $N_{\text{b-jet}} > 0$, the $\text{Z} \to \ell^+\ell^-$ CS is used with some help from simulated events where necessary. The $\text{Z} \to \ell^+\ell^-$ CS suffers from low statistics in the higher signal bins, thus simulated events are used to help the estimates there.

6.2.1 $\text{Z} \to \nu\overline{\nu}$ prediction method for $N_{\text{b-jet}} = 0$

The number of $\text{Z} \to \nu\overline{\nu}$ + jets events in the 18 $N_{\text{b-jet}} = 0$ search bins, $N^{\text{pred}}_{\text{Z}\to\nu\overline{\nu}}$, can be estimated by the number of events in the corresponding search bin of the γ + jets CS, N^{data}_{γ}:

$$N^{\text{pred}}_{\text{Z}\to\nu\overline{\nu}}\Big|_{N_{\text{b-jet}}=0} = \rho \cdot \mathcal{R}_{\text{Z}\to\nu\overline{\nu}/\gamma} \cdot \beta_{\gamma} \cdot N^{\text{data}}_{\gamma}, \tag{6.11}$$

where, β_γ is the purity of the γ + jets CS, and $\mathcal{R}_{\text{Z}\to\nu\overline{\nu}/\gamma}$ is the ratio from the $\text{Z} \to \nu\overline{\nu}$ + jets events to γ + jets events, as taken from simulation. The value of $\mathcal{R}_{\text{Z}\to\nu\overline{\nu}/\gamma}$ depends on the search bin and this can be seen in Fig. 6.8. The factor ρ in Eq. 6.11 is defined as:

$$\rho = \frac{\mathcal{R}^{\text{data}}_{\text{Z}\to\ell^+\ell^-/\gamma}}{\mathcal{R}^{\text{sim}}_{\text{Z}\to\ell^+\ell^-/\gamma}} = \frac{N^{\text{data}}_{\text{Z}\to\ell^+\ell^-}}{N^{\text{data}}_{\gamma}} \cdot \frac{N^{\text{sim}}_{\gamma}}{N^{\text{sim}}_{\text{Z}\to\ell^+\ell^-}}, \tag{6.12}$$

where the $\text{Z} \to \ell^+\ell^-$ CS is used to account for possible differences between simulation ('sim' in Eq. 6.12) and data in the $\mathcal{R}_{\text{Z}\to\nu\overline{\nu}/\gamma}$ ratio. This double ratio is expected to be close to unity, as most data and simulation differences should cancel out, and indeed has a constant value of 0.92. The uncertainty on this value however does depend on N_{jet}, H_{T} and $H^{\text{miss}}_{\text{T}}$, which ranges from 8 to 60%.

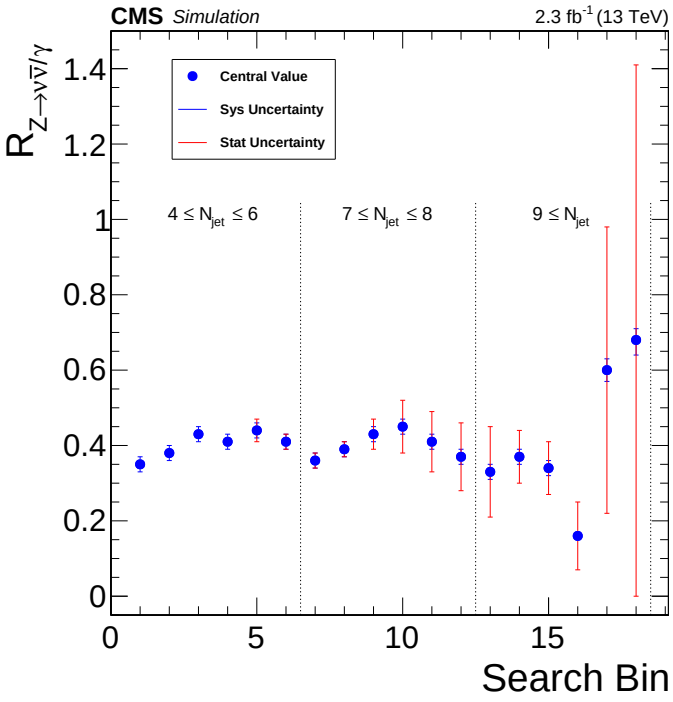

Figure 6.8: The ratio $\mathcal{R}_{Z\to\nu\bar{\nu}/\gamma}$ in the 18 $N_{\text{b-jet}} = 0$ search bins. The six bins within each dashed line refer to the six kinematic regions of H_T and H_T^{miss}, as seen in Fig. 5.5. The red bars represent the statistical uncertainty and the blue bars represent the systematic uncertainties.

The purity of the γ + jets CS is defined as:

$$\beta_\gamma = \frac{N_{\text{prompt}}}{N_{\text{prompt}} + N_{\text{non-prompt}}}, \tag{6.13}$$

which is the fraction of all photons that are prompt. This γ + jets CS purity is found to be dependent on photon p_T, which is approximately the H_T of the event. Accordingly, the values of β_γ are given in Tab. 6.3.

Table 6.3: The purity and absolute uncertainties of the γ + jets CS in bins of H_T.

H_T range [GeV]	Purity
200-500	96.3 ± 0.3 %
500+	90 ± 3 %

6.2.2 $Z \to \nu\overline{\nu}$ prediction method for $N_{\text{b-jet}} > 0$

The prediction in the $N_{\text{b-jet}} > 0$ search bins is given by these relations:

$$\left(N^{\text{pred}}_{Z\to\nu\overline{\nu}}\right)_{j,b,k} = \left(N^{\text{pred}}_{Z\to\nu\overline{\nu}}\right)_{j,0,k} \mathcal{F}_{j,b}; \tag{6.14}$$

$$\mathcal{F}_{j,b} = \left(N^{\text{data}}_{Z\to\ell^+\ell^-} \cdot \beta_{\ell\ell}\right)_{0,b} / \left(N^{\text{data}}_{Z\to\ell^+\ell^-} \cdot \beta_{\ell\ell}\right)_{0,0} \cdot \mathcal{J}_{j,b}; \tag{6.15}$$

$$\mathcal{J}_{j,b} = N^{\text{sim}}_{j,b} / N^{\text{sim}}_{0,b}. \tag{6.16}$$

The j, b, and k are bin indices referring to the N_{jet}, $N_{\text{b-jet}}$, and kinematic variables (see Fig. 5.5), respectively. The first term on the right hand side of Eq. 6.14 is simply the prediction from Eq. 6.11, while the second term is the extrapolation factor (defined in Eq. 6.15) from $Z \to \ell^+\ell^-$ events to predict the $N_{\text{b-jet}} > 0$ regions. The Z purity, $\beta_{\ell\ell}$, is dependent on $N_{\text{b-jet}}$ and its form is given in Tab. 6.4. The $N_{\text{b-jet}}$ distribution depends on N_{jet}, thus, the $\mathcal{J}_{j,b}$ factor is introduced (defined in Eq. 6.16). This factor uses a model estimate, $N^{\text{sim}}_{j,b}$, of the $Z \to \ell^+\ell^-$ simulation as the mean value, as the $Z \to \ell^+\ell^-$ data lacks sufficient statistics. To determine the uncertainty on $\mathcal{J}_{j,b}$, limiting cases of $N^{\text{sim}}_{j,b}$ are taken. At the low end, setting $N^{\text{sim}}_{j,b} = N^{\text{sim}}_{0,b}$ implies $\mathcal{F}_{j,b}$ is independent of N_{jet}. This in turn implies that one can factorize the processes which produce b-quark and other jets. At the high end, one can set $N^{\text{sim}}_{j,b} = \sum_{N_{\text{jet}}\in j, N_{\text{b-jet}}\in b} \mathcal{B}(N_{\text{b-jet}}|N_{\text{jet}}; p)$, where $\mathcal{B}$ is a binomial distribution and p is the probability for a jet to be tagged as a b-jet. If all b-jets are identified incorrectly, i.e. not coming from an actual b-quark, or if the quarks produced in hadron showers do not depend on flavor, then this binomial distribution should be expected. This binomial calculation and factorization then serve as opposite ends of the uncertainty calculation. The probability p is determined from data as 0.062 ± 0.007 and validated in simulation. The full value of $\mathcal{F}_{j,b}$ across the N_{jet} and $N_{\text{b-jet}}$ space can be seen in Tab. 6.5.

Table 6.4: The purity and absolute uncertainties obtained from data. Low data statistics do not allow for separate purity fits for $= 2$ and ≥ 3 $N_{\text{b-jet}}$; thus they are combined for the Z purity estimate.

Sample	0 $N_{\text{b-jet}}$	1 $N_{\text{b-jet}}$	≥ 2 $N_{\text{b-jet}}$
$Z \to \mu^+\mu^-$	0.96 ± 0.06	0.75 ± 0.17	0.64 ± 0.25
$Z \to e^+e^-$	0.98 ± 0.06	0.91 ± 0.18	

Table 6.5: The extrapolation factors for $N_{\text{b-jet}} > 0$ are given with statistical and systematic uncertainties. The first column, Bin, defines the $N_{\text{b-jet}}$ and $N_{\text{b-jet}}$ bin: $4(i-1)+j$, where i (j) is the index of the N_{jet} ($N_{\text{b-jet}}$) bin. The extrapolation factor for each bin, $\mathcal{F}$, is then given with its statistical uncertainty. The systematic uncertainties are the left three columns: the Z purity, $\beta_{\ell\ell}$, to the $N_{\text{b-jet}}$ share in N_{jet} bins, $\mathcal{J}$, and to the kinematic dependence. The symmetric part of the uncertainty on $\mathcal{J}$ comes from statistics of simulated events.

Bin	$\mathcal{F}$	σ_{stat}	$\sigma_{\beta_{\ell\ell}}$	$\sigma_{\mathcal{J}}$	σ_{kin}
1	1.000	0	0	$\pm 0^{+0}_{-0}$	0
2	0.202	0.16	0.15	$\pm 0^{+0}_{-0}$	0.10
3	0.044	0.29	0.38	$\pm 0^{+0}_{-0}$	0.15
4	0.010	0.58	0.38	$\pm 0^{+0}_{-0}$	0.20
5	1.000	0	0	$\pm 0^{+0}_{-0}$	0
6	0.426	0.16	0.15	$\pm 0.06^{+0}_{-0.19}$	0.10
7	0.175	0.29	0.38	$\pm 0.09^{+0.06}_{-0.21}$	0.15
8	0.093	0.58	0.38	$\pm 0.48^{+0}_{-0.42}$	0.20
9	1.000	0	0	$\pm 0^{+0}_{-0}$	0
10	0.731	0.16	0.15	$\pm 0.15^{+0}_{-0.19}$	0.10
11	0.406	0.29	0.38	$\pm 0.26^{+0.06}_{-0.17}$	0.15
12	0.086	0.58	0.38	$\pm 1.00^{+0.62}_{-0.12}$	0.20

6.2.3 $Z \to \nu\overline{\nu}$ background prediction summary

To summarize the $Z \to \nu\overline{\nu}$ background estimate method, the $N_{\text{b-jet}} = 0$ and $N_{\text{b-jet}} > 0$ regions are predicted separately. For the former, the γ + jets CS is used to calculate the background in those 18 search bins and for the latter, the $Z \to \ell^+\ell^-$ CS is used. The γ + jets CS determines the background shape in the N_{jet}, H_{T}, and $H_{\text{T}}^{\text{miss}}$ dimensions and the $Z \to \ell^+\ell^-$ CS determines the background shape in the $N_{\text{b-jet}}$ dimension. Because of limited statistics, the $Z \to \ell^+\ell^-$ sample is integrated over the kinematic variables, H_{T} and $H_{\text{T}}^{\text{miss}}$, and then extrapolated to the $N_{\text{b-jet}} > 0$ regions. A closure test of this method is shown in Fig. 6.9.

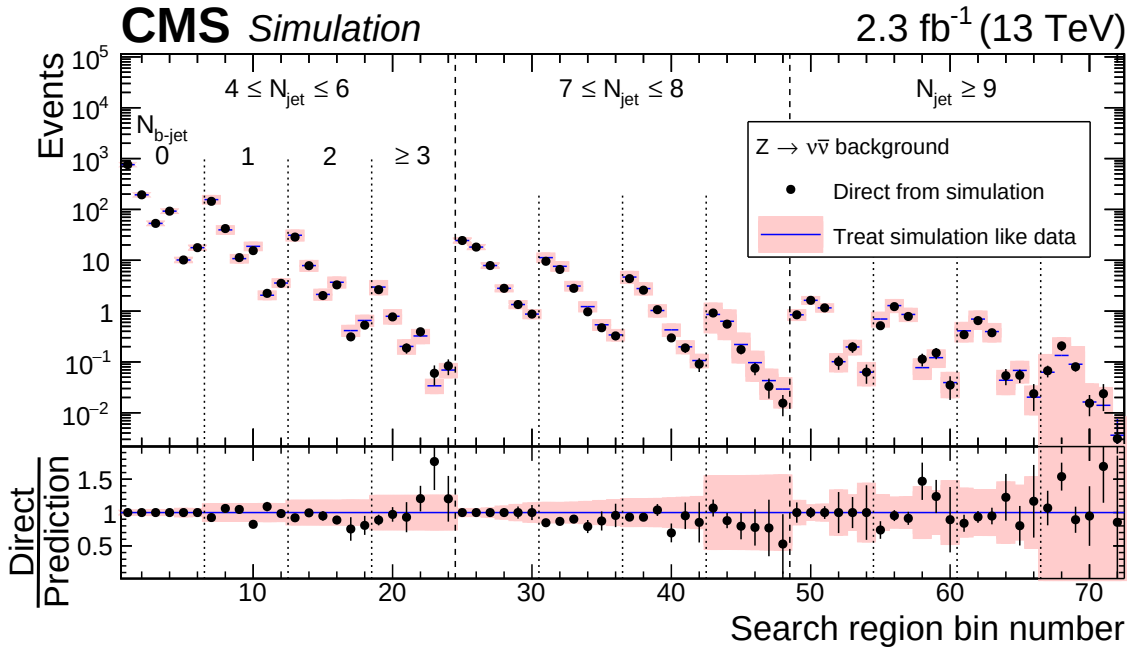

Figure 6.9: Comparison of the $Z \to \nu\overline{\nu}$ prediction to the simulated event expectation in the 72 exclusive search bins. The black points are simulated events and the pink histograms are the predictions from the lost lepton method, both with statistical uncertainties. The six bins within each dashed line refer to the six kinematic regions of H_{T} and $H_{\text{T}}^{\text{miss}}$, as seen in Fig. 5.5. Overall, there is reasonable agreement between the prediction and the expectation.

6.2.4 Method Uncertainties

In addition to the $N_{\text{b-jet}}$ extrapolation related uncertainty previously discussed, additional uncertainties on the method must be considered. The $\rho \cdot \mathcal{R}_{Z\to\nu\overline{\nu}/\gamma}$ term dominates the overall uncertainty, except for in the highest N_{jet} and $N_{\text{b-jet}}$ bins, where the limited statistics of the simulated events as well as the purity on $Z \to \ell^+\ell^-$ becomes prevalent. Furthermore, smaller but non-negligible uncertainties come from: photon reconstruction efficiency, photon and dilepton purities, and systematic uncertainty from the statistical precision of simulated events.

6.3 The QCD multijet background

As described earlier the QCD multijet background arises from the mismeasurement of jet energy, as seen in Fig. 6.10. As such, these events do not contain real missing energy. Thus, events with large jet energy mismeasurement can contribute to the search region. A single mismeasured jet is the major cause of the $H_{\text{T}}^{\text{miss}}$ in such events. For this reason, the $H_{\text{T}}^{\text{miss}}$ direction is often close to a jet. The $\Delta\phi_{\text{min}}$ variable, which is the minimum ϕ difference between $H_{\text{T}}^{\text{miss}}$ and the four highest p_{T} jets, then is sensitive to this background.

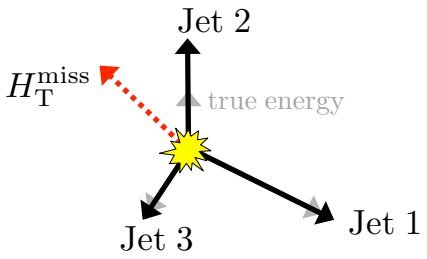

Figure 6.10: A representation of jet mismeasurement in QCD multijet events.

A QCD CS is established by flipping the $\Delta\phi_{\text{min}}$ requirement (i.e $\Delta\phi_1 < 0.5$ or $\Delta\phi_2 < 0.5$ or $\Delta\phi_3 < 0.3$ or $\Delta\phi_4 < 0.3$). The rest of the baseline selection remains the same. The QCD CS is QCD dominated and contains 90% of QCD simulated events. The

background in the search region is modeled quite simply: using the QCD yield in the QCD CS alongside a high/low ratio, R^{QCD}, an extrapolation is made from the QCD CS to the search region. The high/low ratio shows dependence on the search variables, N_{jet}, H_{T}, and $H_{\text{T}}^{\text{miss}}$. The $N_{\text{b-jet}}$ dimension shows major dependence for the high/low ratio, but only within the first N_{jet} bin (i.e. between 4 and 6 jets) for a given value of N_{jet}. To circumvent the $N_{\text{b-jet}}$ dependence, the first N_{jet} bin is subdivided into separate $N_{\text{jet}} = 4$, $N_{\text{jet}} = 5$, and $N_{\text{jet}} = 6$ bins. Further, the first $H_{\text{T}}^{\text{miss}}$ bin (i.e. between 200 and 500 GeV) is subdivided into two bins: 200-300 and 300-500 GeV. Because the QCD background falls quickly in the $H_{\text{T}}^{\text{miss}}$ dimension, subdividing the first $H_{\text{T}}^{\text{miss}}$ bin allows for a better handle on its shape. Thus, the QCD background model uses a set of finer bins than the search region, and the QCD fine binning structure can be seen in Fig. 6.11.

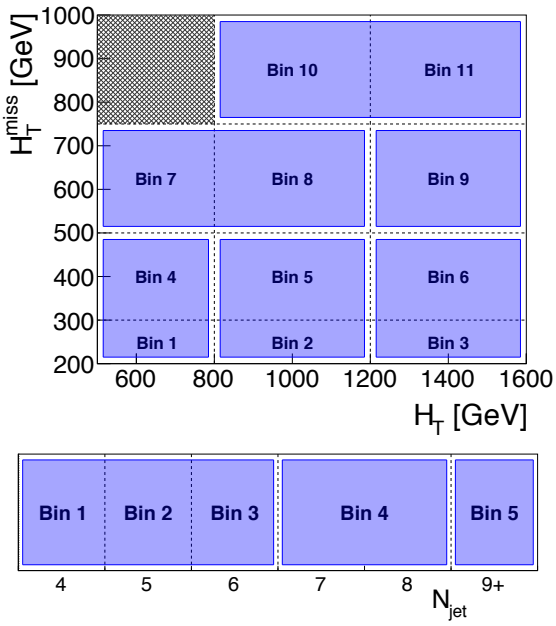

Figure 6.11: The binning in H_{T}, $H_{\text{T}}^{\text{miss}}$ (top) and N_{jet} (bottom) used in the QCD background model. The dotted lines and black bin labels define the fine binning used for the QCD background model. The blue boxes represent the search bins, as can be seen in Fig. 5.5. Note the $N_{\text{b-jet}}$ is not a binned variable in this background estimate.

Fig. 6.12 shows the $\Delta\phi_{\text{min}}$ distributions in bins of H_{T}, $H_{\text{T}}^{\text{miss}}$ and N_{jet} after the baseline selection and exhibits the dependence of the high/low ratio on those search vari-

ables. The dependence of R^{QCD} on H_{T}, $H_{\mathrm{T}}^{\mathrm{miss}}$ and N_{jet} is assumed to be factorizable, i.e., the H_{T} dependence is independent from $H_{\mathrm{T}}^{\mathrm{miss}}$ and N_{jet}, the $H_{\mathrm{T}}^{\mathrm{miss}}$ dependence is independent from H_{T} N_{jet}, and the N_{jet} dependence is independent from H_{T} and $H_{\mathrm{T}}^{\mathrm{miss}}$. Formally, this translates as

$$R^{QCD}_{i,j,k} = K^{QCD}_{H_{\mathrm{T}},i} \cdot S^{QCD}_{H_{\mathrm{T}}^{\mathrm{miss}},j} \cdot S^{QCD}_{N_{\mathrm{jet}},k}, \tag{6.17}$$

where i, j, and k are bin indices for the H_{T}, $H_{\mathrm{T}}^{\mathrm{miss}}$ and N_{jet} dimensions, respectively. The $K^{QCD}_{H_{\mathrm{T}},i}$ parameter is the high/low ratio for H_{T} bin i in the first $H_{\mathrm{T}}^{\mathrm{miss}}$ and N_{jet} bins. The $S^{QCD}_{H_{\mathrm{T}}^{\mathrm{miss}},j}$ parameter is a correction for $H_{\mathrm{T}}^{\mathrm{miss}}$ bin j with respect to the first $H_{\mathrm{T}}^{\mathrm{miss}}$ bin. And similarly, the $S^{QCD}_{N_{\mathrm{jet}},j}$ parameter is a correction for N_{jet} bin k with respect to the first N_{jet} bin.

The factorization assumption of the high/low ratio is modeled and tested by fitting the $R^{QCD}_{i,j,k}$ for the S^{QCD} and K^{QCD} parameters with a χ^2 test using QCD simulated events. This χ^2 fit test outcome can be seen in Fig. 6.13 and Tab. 6.8. Lack of QCD simulated event statistics means some bins do not have any black points. Given this limitation, the central assumption, the factorization of the search variables, is validated because of the general agreement shown in Fig. 6.13.

A further test of the factorization method can be done by adding the $N_{\text{b-jet}}$ dimension back. That is, the term $S^{QCD}_{N_{\text{b-jet}},l}$ can be introduced to Eq. 6.17. Assuming the same factorization as with the other search variables, the fit of Fig. 6.13 with three additional $S^{QCD}_{N_{\text{b-jet}},l}$ parameters is repeated. The $S^{QCD}_{N_{\text{b-jet}},l}$ parameters can be found in Tab. 6.6 As the introduction of the $N_{\text{b-jet}}$ parameters further subdivides the statistics by a factor of four (from 55 bins to 220 bins), within this context, the $S^{QCD}_{N_{\text{b-jet}},l}$ parameters are considered to be effectively equal to unity.

In order to obtain the QCD high/low parameters actually used in the background method, a maximum likelihood analysis is performed on the data using the QCD fine binning

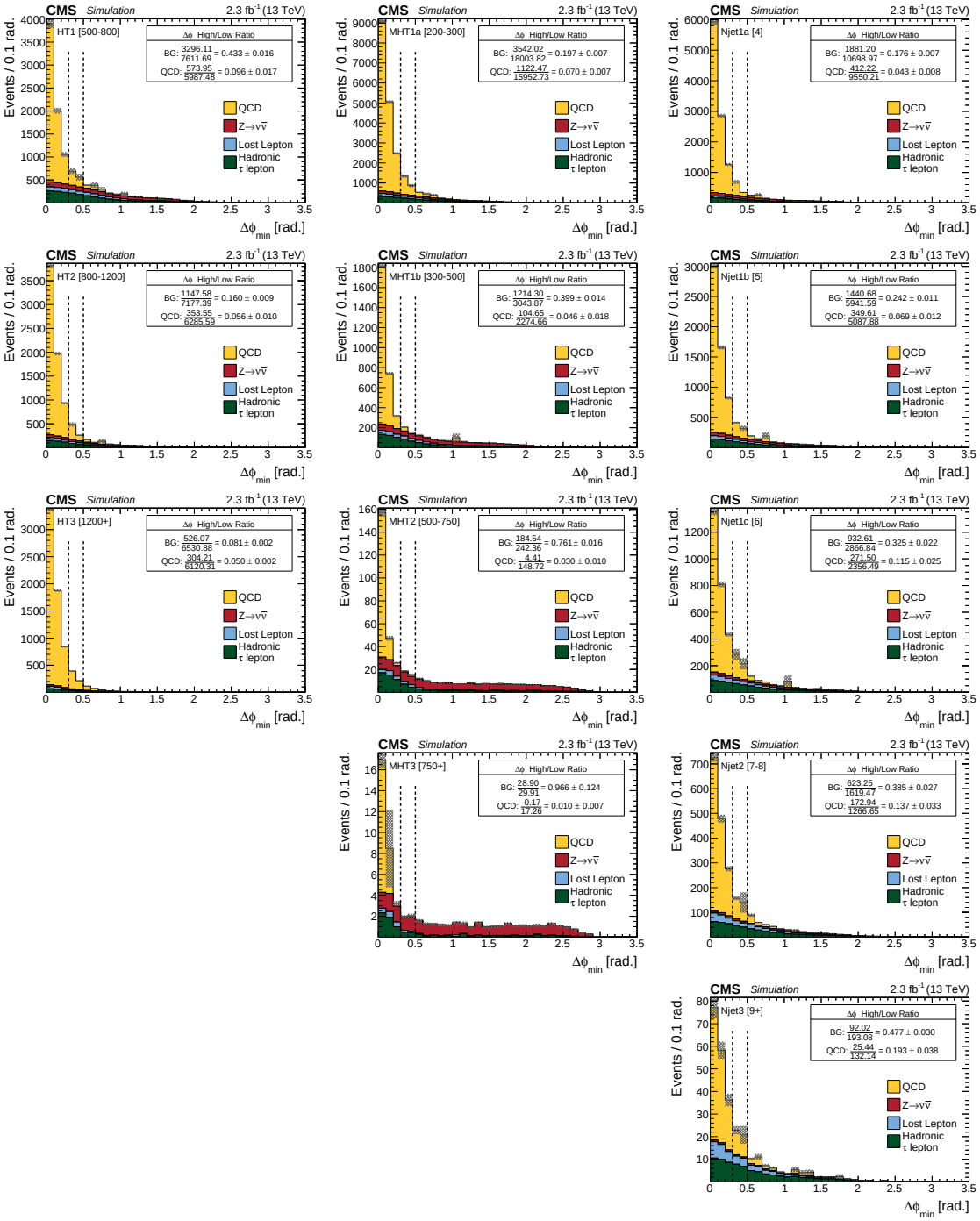

Figure 6.12: Distributions of $\Delta\phi_{\text{min}}$ within the QCD CS in bins of one of the search variables, integrated over the others. The left column is the three H_{T} bins, the middle column is the four $H_{\text{T}}^{\text{miss}}$ bins, and the right column is the five N_{jet} bins.

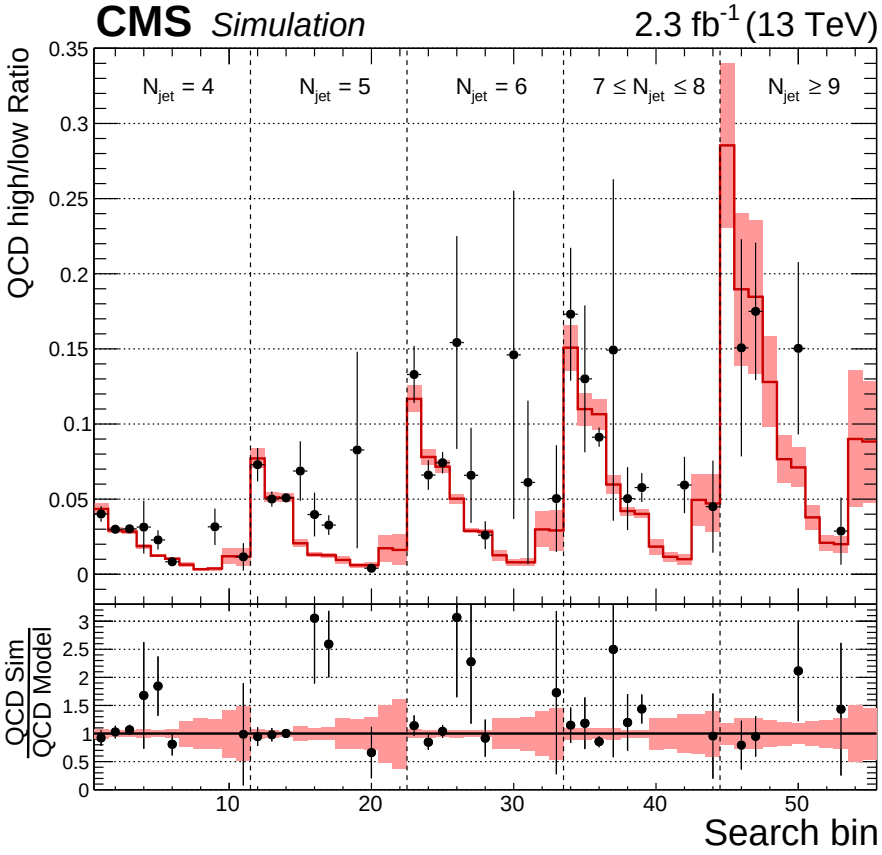

Figure 6.13: The QCD high/low ratio fit results. The black points are the simulated QCD event ratios while the red shaded regions represent the χ^2 fit result. The plot is split by five dashed sections, which correspond to the five N_{jet} bins within the QCD model, increasing to the right. Within each N_{jet} bin, there are the 11 kinematic bins within the QCD model (i.e. H_{T} and $H_{\text{T}}^{\text{miss}}$), as in Fig. 6.11.

structure. The likelihood fit includes both the QCD CS (the 'low-$\Delta\phi_{\text{min}}$' region) and the search region (the 'high-$\Delta\phi_{\text{min}}$' region). As can be seen in Fig. 6.12 and in particular Fig. 6.14, there is non-negligible contributions of the other three backgrounds in the QCD CS. That is, the hadronic τ decay, lost lepton, and $\text{Z} \to \nu\overline{\nu}$ backgrounds must also be estimated in the QCD CS using the standard techniques for those backgrounds, but using an inverted $\Delta\phi_{\text{min}}$ requirement. Using the nominal background estimates in the search region as well as in the QCD CS, the QCD contribution can then be determined.

Due to the current size of the dataset, the likelihood fit is unable to establish the

Table 6.6: The model parameters for $S^{QCD}_{N_{\text{b-jet}}}$ when the $N_{\text{b-jet}}$ parameter is included in the QCD background estimate.

QCD Parameter	Bin Range	χ^2 Fit Value
$S^{QCD}_{N_{\text{b-jet}},1}$	$N_{\text{b-jet}} = 0$	1 (fixed)
$S^{QCD}_{N_{\text{b-jet}},2}$	$N_{\text{b-jet}} = 1$	0.83 ± 0.06
$S^{QCD}_{N_{\text{b-jet}},3}$	$N_{\text{b-jet}} = 2$	0.91 ± 0.11
$S^{QCD}_{N_{\text{b-jet}},4}$	$N_{\text{b-jet}} \geq 3$	0.73 ± 0.11

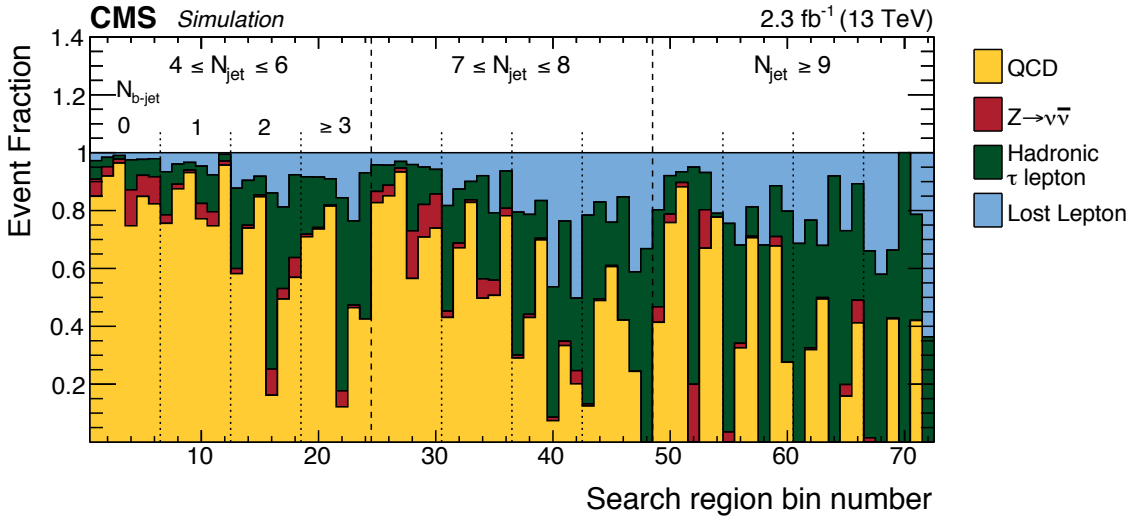

Figure 6.14: Plot of the relative background contributions in the inverted $\Delta\phi_{\text{min}}$ region. The six bins within each dashed line refer to the six kinematic regions of H_{T} and $H_{\text{T}}^{\text{miss}}$, as seen in Fig. 5.5.

$H_{\text{T}}^{\text{miss}}$ dependence of the QCD background in data. Instead, the $H_{\text{T}}^{\text{miss}}$ QCD parameters are constrained by the values calculated from simulation. This procedure is done by the following: generator-level jets are matched to reconstructed-level jets. A 'bad' jet is the one in each event with the greatest absolute difference in generator-level p_{T} and reconstructed-level p_{T}. Two event categories are then made, those where the 'bad' jet is in the $\Delta\phi_{\text{min}}$ calculation and those where the 'bad' jet is not in the $\Delta\phi_{\text{min}}$ calculation. Then, the contributions from these two event categories to the QCD high/low ratios as a function of $H_{\text{T}}^{\text{miss}}$ is made: Fig. 6.15. The event category where the 'bad' jet is not in the $\Delta\phi_{\text{min}}$ calculation

only occurs 2% of the time and is independent of $H_{\mathrm{T}}^{\mathrm{miss}}$. Given Fig. 6.15 and assuming a generous 100% uncertainty on the component where the 'bad' jet is not in the $\Delta\phi_{\mathrm{min}}$ calculation, the $H_{\mathrm{T}}^{\mathrm{miss}}$ parameters can be determined, as shown in Tab. 6.7.

Table 6.7: The model parameters for $S_{H_{\mathrm{T}}^{\mathrm{miss}}}^{QCD}$.

QCD Parameter	Bin Range	Value
$S_{H_{\mathrm{T}}^{\mathrm{miss}},1}^{QCD}$	200 to 300 GeV	1 (fixed)
$S_{H_{\mathrm{T}}^{\mathrm{miss}},2}^{QCD}$	300 to 500 GeV	0.50 ± 0.25
$S_{H_{\mathrm{T}}^{\mathrm{miss}},3}^{QCD}$	500 to 750 GeV	0.50 ± 0.50
$S_{H_{\mathrm{T}}^{\mathrm{miss}},4}^{QCD}$	$\geq$ 750 GeV	0.50 ± 0.50

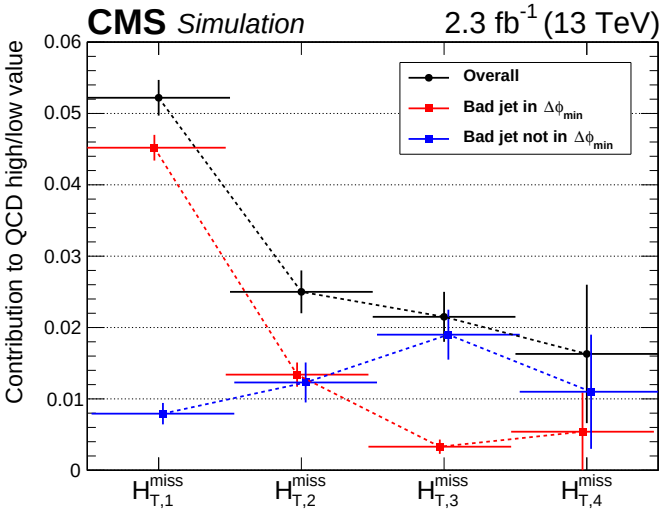

Figure 6.15: Plot of the contribution to the QCD high/low ratio as a function of $H_{\mathrm{T}}^{\mathrm{miss}}$, in simulation. The contributions are split by whether the jet with the worst p_{T} reconstruction (largest absolute generated minus reconstruction p_{T} ($|\text{gen } p_{\mathrm{T}} - \text{reco } p_{\mathrm{T}}|$) difference) is or is not (red or blue, respectively) included in the leading four p_{T}-ranked jets.

As a test of the likelihood method, simulated events are fitted for the QCD high/low parameters. These fit values can be found in Tab. 6.8. These likelihood fit values from simulation agree with χ^2 fit values of the QCD simulation. The likelihood fit values from data are also given in Tab. 6.8 as well as Fig. 6.16. These are the parameters used in

the QCD background estimation.

Table 6.8: Model parameters for the QCD $\Delta\phi_{\text{min}}$ background evaluation. The χ^2 fit column gives the results of the direct fit of the QCD simulation for the high/low ratio parameters, which is shown in Figure 6.13. The "Sim Likelihood fit" column gives the results of the likelihood fit of a 2.3 fb^{-1} test dataset (simulation) where the observed counts are set to the expected number of events from simulation, including all components (QCD, hadronic τ decay, lost lepton, and Z $\rightarrow \nu\overline{\nu}$). The last column gives the likelihood fit results for the 2.3 fb^{-1} data sample. The likelihood fit is unable to determine the last three $H_{\text{T}}^{\text{miss}}$ parameters so those parameters are constrained to values derived from the QCD simulation. The fitted parameters are plotted in Fig 6.16.

QCD Parameter	Bin range	χ^2 fit	Likelihood fit	
			Sim	Data
$K^{QCD}_{H_{\text{T}},1}$	500 to 800 GeV	0.043 ± 0.004	0.036 ± 0.025	0.048 ± 0.024
$K^{QCD}_{H_{\text{T}},2}$	800 to 1200 GeV	0.029 ± 0.003	0.031 ± 0.007	0.023 ± 0.007
$K^{QCD}_{H_{\text{T}},3}$	>1200 GeV	0.029 ± 0.002	0.032 ± 0.005	0.028 ± 0.006
$S^{QCD}_{H_{\text{T}}^{\text{miss}},1}$	200 to 300 GeV	1 (fixed)	1 (fixed)	1 (fixed)
$S^{QCD}_{H_{\text{T}}^{\text{miss}},2}$	300 to 500 GeV	0.423 ± 0.047	not in fit	not in fit
$S^{QCD}_{H_{\text{T}}^{\text{miss}},3}$	500 to 750 GeV	0.116 ± 0.042	not in fit	not in fit
$S^{QCD}_{H_{\text{T}}^{\text{miss}},4}$	>750 GeV	0.471 ± 0.204	not in fit	not in fit
$S^{QCD}_{N_{\text{jet}},1}$	= 4	1 (fixed)	1 (fixed)	1 (fixed)
$S^{QCD}_{N_{\text{jet}},2}$	= 5	1.81 ± 0.15	1.62 ± 0.29	1.91 ± 0.44
$S^{QCD}_{N_{\text{jet}},3}$	= 6	2.68 ± 0.24	2.36 ± 0.48	2.30 ± 0.65
$S^{QCD}_{N_{\text{jet}},4}$	7 to 8	3.51 ± 0.32	3.05 ± 0.74	3.59 ± 1.05
$S^{QCD}_{N_{\text{jet}},5}$	≥ 9	6.44 ± 1.35	4.89 ± 2.30	3.30 ± 1.84

6.3.1 QCD final background prediction

Once the QCD high/low ratio parameters have been obtained, the 72 search bins are used for the final QCD background prediction. The finer bins of the QCD method are combined back into the search bins by computing a weighted average of the QCD high/low ratios. This ratio for each search bin is then used in conjunction with the QCD CS to

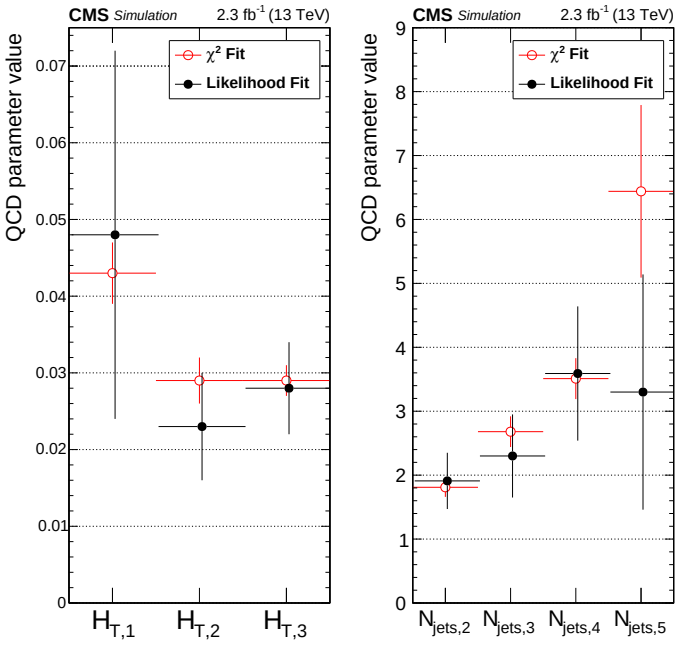

Figure 6.16: QCD background model parameters determined a binned likelihood of data (solid black points) versus the χ^2 fit from QCD simulation (open red points). The numerical values can be found in Tab. 6.8.

make the prediction. A closure test, similar to the other background estimates, is given in Fig. 6.17.

6.3.2 Method Uncertainties

In the lowest $H_{\mathrm{T}}^{\mathrm{miss}}$ search bin, the dominant uncertainty on the prediction is uncertainty in the $K_{H_{\mathrm{T}},i}^{QCD}$ and $S_{N_{\mathrm{jet}},k}^{QCD}$ model parameters. These parameters, in turn, are largely due to the uncertainties in the non-QCD backgrounds in the signal region. For the higher $H_{\mathrm{T}}^{\mathrm{miss}}$ search bins, the dominant uncertainty is the uncertainty in the $S_{H_{\mathrm{T}}^{\mathrm{miss}},j}^{QCD}$ parameter coupled with the low statistics of the QCD CS.

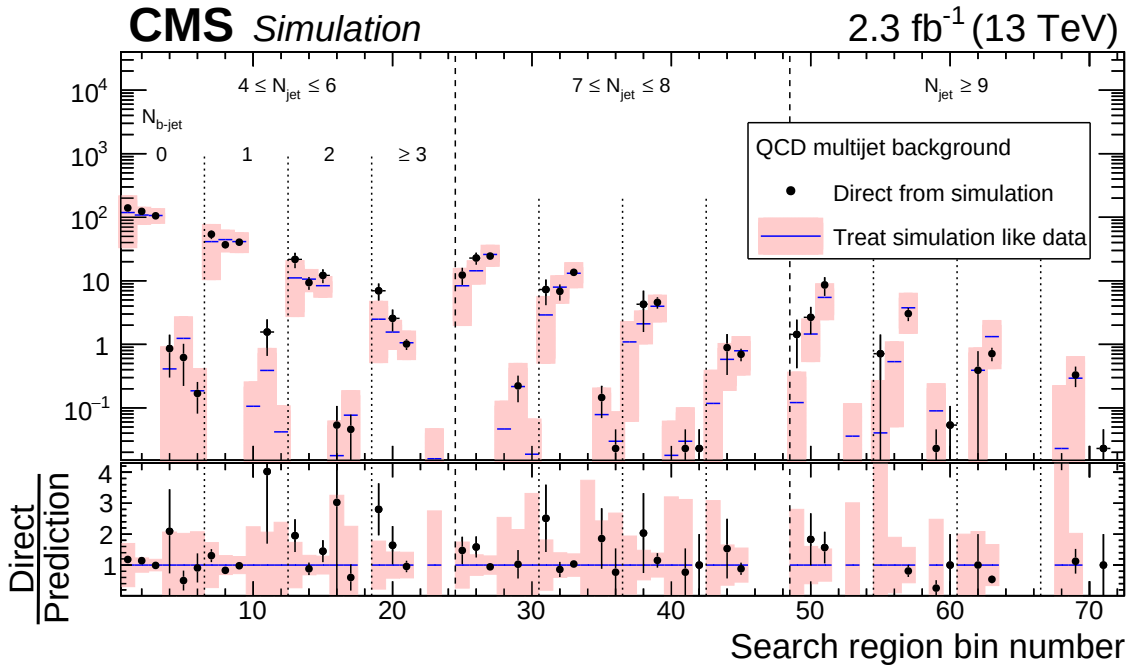

Figure 6.17: Comparison of the QCD prediction to the simulated event expectation in the 72 exclusive search bins. The black points are simulated events and the pink histograms are the predictions from the lost lepton method, both with statistical uncertainties. The six bins within each dashed line refer to the six kinematic regions of H_{T} and $H_{\mathrm{T}}^{\mathrm{miss}}$, as seen in Fig. 5.5. Overall, there is reasonable agreement between the prediction and the expectation. Bins without any markers contain no QCD CS events.

Chapter 7

Results and Discussion

All four background methods, lost lepton, τ_{h}, $\mathrm{Z} \to \nu\overline{\nu}$, and QCD, are combined to form the total background prediction and compared to the data. The final results and the interpretation of the results are then given in this chapter.

7.1 Observations and results

The total observed event counts in the 72 search bins are compared to the combined background predictions in both graphical and tabular form. Fig. 7.1 shows the full results as a plot. The observed event counts appear to be in good agreement to within uncertainties with the data-driven standard model background prediction and no excess is seen in data: no evidence for new physics or SUSY is found. An alternate presentation of the observed and predicted event counts are given in tabular form in Tab. 7.1, 7.2, and 7.3. These tables are separated by the three N_{jet} bins: Tab. 7.1 contains events for $4 \leq N_{\mathrm{jet}} \leq 6$ (the leftmost section of Fig. 7.1), Tab. 7.2 contains events for $7 \leq N_{\mathrm{jet}} \leq 8$ (the center section of Fig. 7.1), and Tab. 7.3 contains events for $N_{\mathrm{jet}} \geq 9$ (the rightmost section of Fig. 7.1).

One-dimensional projections of the results in the H_{T} or $H_{\mathrm{T}}^{\mathrm{miss}}$ plane are shown in Fig. 7.2. The search region intervals are selected in these events to be purposefully sensitive to the scenario in question. In each plot, the example distributions show two signal scenarios

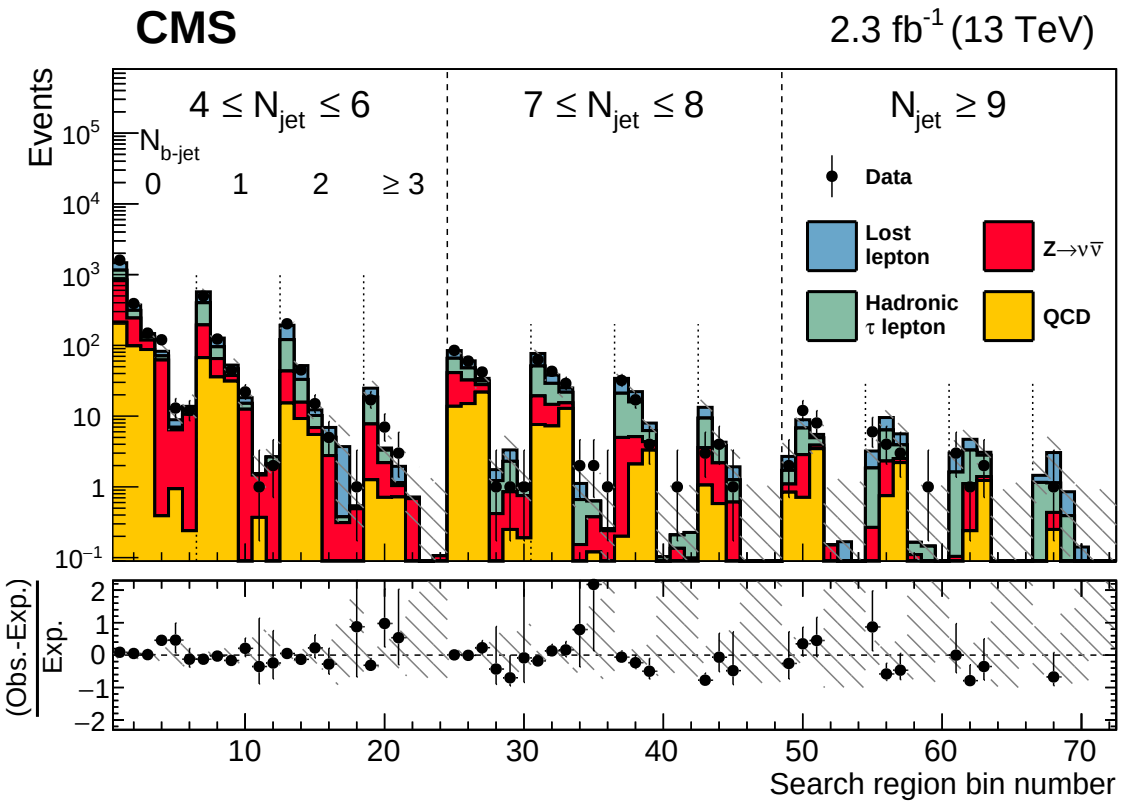

Figure 7.1: Observed number of events compared to the background predictions in all 72 search bins.

that were not previously excluded by earlier studies [64, 65], but these scenarios are now comfortably excluded by this analysis. An event display can be seen in Fig. 7.3 which shows the content of a signal region event.

Table 7.1: Observed number of events and background predictions in the $4 \leq N_{\text{jet}} \leq 6$ search bins.

Bin	$H_{\text{T}}^{\text{miss}}$ [GeV]	H_{T} [GeV]	$N_{\text{b-jet}}$	Lost-e/μ	τ_{h}	$\text{Z} \to \nu\overline{\nu}$	QCD	Total Pred.	Obs.
1	200-500	500-800	0	$318.76^{+11.84+28.74}_{-11.82-27.67}$	$310.30^{+10.78+19.37}_{-10.77-18.87}$	$631.79^{+13.20+102.80}_{-13.20-81.76}$	$212.06^{+3.71+116.20}_{-3.64-116.20}$	$1472.91^{+26.45+158.72}_{-26.42-145.98}$	1602
2	200-500	800-1200	0	$59.15^{+4.33+5.47}_{-4.29-5.28}$	$69.08^{+5.21+5.67}_{-5.19-5.59}$	$144.92^{+6.29+25.92}_{-6.29-20.42}$	$98.29^{+1.77+35.77}_{-1.74-35.77}$	$371.44^{+11.57+44.84}_{-11.51-41.90}$	390
3	200-500	1200+	0	$13.84^{+2.25+1.38}_{-2.17-1.30}$	$14.38^{+2.57+1.56}_{-2.53-1.51}$	$31.36^{+2.95+11.93}_{-2.95-8.33}$	$87.33^{+1.88+25.47}_{-1.84-25.47}$	$146.91^{+5.96+28.20}_{-5.85-26.87}$	149
4	500-750	500-1200	0	$11.49^{+1.93+1.57}_{-1.84-1.53}$	$8.92^{+1.72+1.33}_{-1.66-1.32}$	$61.62^{+4.41+18.46}_{-4.41-13.29}$	$0.39^{+0.12+0.44}_{-0.09-0.30}$	$82.41^{+5.73+18.57}_{-5.64-13.45}$	120
5	500-750	1200+	0	$1.95^{+1.04+0.50}_{-0.90-0.50}$	$0.56^{+0.52+0.15}_{-0.25-0.15}$	$5.45^{+1.32+2.12}_{-1.32-1.51}$	$0.94^{+0.17+0.98}_{-0.14-0.80}$	$8.89^{+2.05+2.39}_{-1.76-1.79}$	13
6	750+	800+	0	$1.39^{+0.93+0.24}_{-0.77-0.23}$	$1.77^{+0.99+0.34}_{-0.88-0.33}$	$10.35^{+1.80+5.81}_{-1.80-4.06}$	$0.24^{+0.09+0.26}_{-0.07-0.17}$	$13.75^{+2.64+5.83}_{-2.45-4.08}$	12
7	200-500	500-800	1	$171.23^{+8.42+16.95}_{-8.39-16.43}$	$205.71^{+8.53+12.98}_{-8.52-12.60}$	$127.47^{+20.90+30.82}_{-20.90-28.14}$	$67.01^{+2.17+39.26}_{-2.10-39.26}$	$571.42^{+27.00+54.04}_{-26.97-52.55}$	499
8	200-500	800-1200	1	$31.37^{+3.98+2.95}_{-3.94-2.86}$	$30.41^{+3.19+2.01}_{-3.16-1.93}$	$29.24^{+4.92+7.40}_{-4.92-6.66}$	$35.79^{+1.13+14.96}_{-1.09-14.96}$	$126.81^{+8.77+17.04}_{-8.71-16.73}$	123
9	200-500	1200+	1	$6.29^{+1.77+0.84}_{-1.64-0.82}$	$8.86^{+2.08+0.90}_{-2.03-0.83}$	$6.33^{+1.19+2.66}_{-1.19-2.03}$	$31.20^{+1.18+11.20}_{-1.13-11.20}$	$52.67^{+4.20+11.57}_{-4.02-11.44}$	44
10	500-750	500-1200	1	$3.07^{+1.17+0.60}_{-1.00-0.59}$	$2.64^{+0.96+0.49}_{-0.85-0.48}$	$12.43^{+2.21+4.34}_{-2.21-3.48}$	$0.07^{+0.04+0.09}_{-0.02-0.05}$	$18.21^{+3.07+4.40}_{-2.88-3.57}$	22
11	500-750	1200+	1	$0.00^{+0.52+0.00}_{-0.00-0.00}$	$0.07^{+0.46+0.02}_{-0.04-0.02}$	$1.10^{+0.32+0.47}_{-0.32-0.36}$	$0.37^{+0.12+0.41}_{-0.09-0.28}$	$1.54^{+1.04+0.62}_{-0.34-0.46}$	1
12	750+	800+	1	$0.00^{+0.50+0.00}_{-0.00-0.00}$	$0.54^{+0.56+0.13}_{-0.32-0.13}$	$2.09^{+0.50+1.23}_{-0.50-0.90}$	$0.02^{+0.06+0.05}_{-0.00-0.02}$	$2.64^{+1.18+1.24}_{-0.59-0.91}$	2
13	200-500	500-800	2	$71.85^{+6.08+7.16}_{-6.05-6.67}$	$77.18^{+4.98+5.48}_{-4.96-5.34}$	$28.08^{+8.07+12.45}_{-8.07-12.14}$	$15.29^{+1.11+9.10}_{-1.04-9.10}$	$192.40^{+13.73+17.63}_{-13.69-17.41}$	202
14	200-500	800-1200	2	$18.80^{+4.79+2.53}_{-4.75-2.20}$	$17.30^{+2.67+1.29}_{-2.63-1.25}$	$6.44^{+1.87+2.90}_{-1.87-2.81}$	$9.25^{+0.62+3.94}_{-0.58-3.94}$	$51.80^{+7.71+5.51}_{-7.63-5.46}$	45
15	200-500	1200+	2	$2.06^{+1.20+0.23}_{-0.98-0.22}$	$3.31^{+1.28+0.34}_{-1.20-0.32}$	$1.39^{+0.42+0.78}_{-0.42-0.68}$	$5.50^{+0.53+2.08}_{-0.48-2.08}$	$12.26^{+2.58+2.26}_{-2.27-2.22}$	15
16	500-750	500-1200	2	$1.90^{+1.84+0.65}_{-1.72-0.17}$	$2.26^{+0.94+0.86}_{-0.82-0.86}$	$2.74^{+0.81+1.40}_{-0.81-1.27}$	$0.03^{+0.02+0.04}_{-0.01-0.02}$	$6.92^{+2.90+1.65}_{-2.67-1.54}$	5
17	500-750	1200+	2	$3.33^{+3.37+1.35}_{-3.33-0.00}$	$0.07^{+0.46+0.02}_{-0.05-0.01}$	$0.24^{+0.09+0.14}_{-0.09-0.12}$	$0.07^{+0.08+0.09}_{-0.04-0.03}$	$3.71^{+3.83+0.16}_{-3.38-0.12}$	0
18	750+	800+	2	$0.00^{+0.46+0.00}_{-0.00-0.00}$	$0.04^{+0.46+0.02}_{-0.03-0.01}$	$0.46^{+0.15+0.32}_{-0.15-0.26}$	$0.03^{+0.06+0.04}_{-0.02-0.01}$	$0.53^{+0.93+0.32}_{-0.16-0.26}$	1
19	200-500	500-800	3+	$6.27^{+1.76+0.79}_{-1.65-0.78}$	$10.82^{+2.17+1.66}_{-2.12-1.62}$	$6.48^{+3.77+3.00}_{-3.77-2.71}$	$1.26^{+0.38+0.90}_{-0.29-0.90}$	$24.83^{+5.46+3.61}_{-5.34-3.37}$	17
20	200-500	800-1200	3+	$0.24^{+0.67+0.03}_{-0.24-0.00}$	$1.10^{+0.61+0.15}_{-0.40-0.14}$	$1.49^{+0.87+0.70}_{-0.87-0.62}$	$0.71^{+0.20+0.39}_{-0.16-0.39}$	$3.54^{+1.56+0.81}_{-1.09-0.75}$	7
21	200-500	1200+	3+	$0.80^{+0.91+0.13}_{-0.57-0.13}$	$0.11^{+0.46+0.02}_{-0.05-0.02}$	$0.32^{+0.19+0.19}_{-0.19-0.13}$	$0.72^{+0.23+0.37}_{-0.18-0.37}$	$1.95^{+1.40+0.43}_{-0.67-0.41}$	3
22	500-750	500-1200	3+	$0.00^{+0.63+0.00}_{-0.00-0.00}$	$0.03^{+0.46+0.01}_{-0.01-0.01}$	$0.63^{+0.37+0.33}_{-0.37-0.26}$	$0.05^{+0.11+0.08}_{-0.04-0.01}$	$0.71^{+1.15+0.34}_{-0.37-0.26}$	0
23	500-750	1200+	3+	$0.00^{+0.77+0.00}_{-0.00-0.00}$	$0.00^{+0.46+0.00}_{-0.00-0.00}$	$0.06^{+0.04+0.03}_{-0.04-0.02}$	$0.00^{+0.05+0.01}_{-0.00-0.00}$	$0.06^{+1.23+0.03}_{-0.04-0.02}$	0
24	750+	800+	3+	$0.00^{+0.58+0.00}_{-0.00-0.00}$	$0.00^{+0.46+0.00}_{-0.00-0.00}$	$0.11^{+0.06+0.08}_{-0.06-0.04}$	$0.00^{+0.04+0.02}_{-0.00-0.00}$	$0.11^{+1.04+0.08}_{-0.06-0.04}$	0

Table 7.2: Observed number of events and background predictions in the $7 \leq N_{\text{jet}} \leq 8$ search bins.

Bin	$H_{\text{T}}^{\text{miss}}$ [GeV]	H_{T} [GeV]	$N_{\text{b-jet}}$	Lost-e/μ	τ_{h}	$\text{Z} \to \nu\bar{\nu}$	QCD	Total Pred.	Obs.
25	200-500	500-800	0	$18.78^{+3.08+2.31}_{-3.05-2.20}$	$24.50^{+2.68+2.02}_{-2.64-2.00}$	$27.40^{+2.78+6.72}_{-2.78-5.14}$	$13.75^{+1.68+8.72}_{-1.50-8.72}$	$84.42^{+6.61+11.40}_{-6.51-10.55}$	85
26	200-500	800-1200	0	$12.53^{+1.83+2.19}_{-1.79-2.17}$	$15.60^{+2.26+1.27}_{-2.22-1.25}$	$17.29^{+2.25+4.19}_{-2.25-3.17}$	$15.03^{+1.14+7.08}_{-1.06-7.08}$	$60.46^{+4.81+8.60}_{-4.72-8.15}$	60
27	200-500	1200+	0	$2.88^{+1.15+0.32}_{-1.07-0.31}$	$3.50^{+1.29+0.31}_{-1.20-0.30}$	$6.03^{+1.29+2.34}_{-1.29-1.66}$	$21.78^{+1.50+8.94}_{-1.40-8.94}$	$34.19^{+3.14+9.25}_{-2.96-9.10}$	42
28	500-750	500-1200	0	$0.53^{+0.45+0.14}_{-0.26-0.13}$	$0.81^{+0.66+0.19}_{-0.47-0.19}$	$0.36^{+0.36+0.12}_{-0.36-0.00}$	$0.06^{+0.10+0.09}_{-0.04-0.02}$	$1.75^{+1.17+0.28}_{-0.82-0.23}$	1
29	500-750	1200+	0	$1.03^{+0.88+0.33}_{-0.80-0.24}$	$1.44^{+0.93+0.29}_{-0.80-0.29}$	$0.60^{+0.43+0.26}_{-0.43-0.18}$	$0.25^{+0.17+0.29}_{-0.11-0.14}$	$3.33^{+1.87+0.54}_{-1.66-0.43}$	1
30	750+	800+	0	$0.17^{+0.38+0.09}_{-0.17-0.00}$	$0.17^{+0.49+0.11}_{-0.17-0.00}$	$0.56^{+0.40+0.34}_{-0.40-0.16}$	$0.19^{+0.15+0.22}_{-0.09-0.10}$	$1.09^{+0.97+0.41}_{-0.53-0.19}$	1
31	200-500	500-800	1	$25.79^{+2.93+3.13}_{-2.90-3.04}$	$31.75^{+2.96+2.34}_{-2.93-2.30}$	$11.68^{+2.24+3.63}_{-2.24-3.82}$	$7.61^{+1.31+5.13}_{-1.13-5.13}$	$76.83^{+6.44+7.35}_{-6.34-7.44}$	63
32	200-500	800-1200	1	$9.01^{+1.63+1.28}_{-1.58-1.10}$	$14.38^{+2.02+1.35}_{-1.97-1.34}$	$7.37^{+1.54+2.27}_{-1.54-2.39}$	$7.26^{+0.83+3.76}_{-0.74-3.76}$	$38.03^{+4.05+4.72}_{-3.94-4.78}$	43
33	200-500	1200+	1	$3.25^{+1.12+0.36}_{-1.01-0.34}$	$6.33^{+1.49+0.67}_{-1.42-0.66}$	$2.57^{+0.69+1.11}_{-0.69-0.99}$	$12.84^{+1.16+5.91}_{-1.07-5.91}$	$24.99^{+2.94+6.06}_{-2.75-6.04}$	29
34	500-750	500-1200	1	$0.46^{+0.49+0.11}_{-0.27-0.11}$	$0.51^{+0.55+0.11}_{-0.29-0.11}$	$0.15^{+0.16+0.06}_{-0.15-0.00}$	$0.00^{+0.11+0.03}_{-0.00-0.00}$	$1.12^{+1.06+0.17}_{-0.58-0.16}$	2
35	500-750	1200+	1	$0.00^{+0.40+0.00}_{-0.00-0.00}$	$0.25^{+0.49+0.05}_{-0.18-0.05}$	$0.26^{+0.19+0.12}_{-0.19-0.07}$	$0.12^{+0.14+0.15}_{-0.07-0.05}$	$0.63^{+0.92+0.20}_{-0.27-0.10}$	2
36	750+	800+	1	$0.00^{+0.45+0.00}_{-0.00-0.00}$	$0.02^{+0.46+0.01}_{-0.01-0.00}$	$0.24^{+0.17+0.15}_{-0.17-0.07}$	$0.00^{+0.08+0.02}_{-0.00-0.00}$	$0.25^{+0.93+0.15}_{-0.17-0.07}$	1
37	200-500	500-800	2	$13.15^{+2.16+1.54}_{-2.11-1.51}$	$16.03^{+1.87+1.20}_{-1.81-1.18}$	$4.79^{+1.46+2.36}_{-1.46-2.43}$	$0.20^{+0.34+0.59}_{-0.05-0.15}$	$34.17^{+4.29+3.10}_{-4.18-3.10}$	32
38	200-500	800-1200	2	$6.33^{+1.29+0.74}_{-1.22-0.71}$	$10.73^{+1.82+0.89}_{-1.76-0.88}$	$3.03^{+0.95+1.48}_{-0.95-1.53}$	$2.10^{+0.47+1.16}_{-0.39-1.16}$	$22.19^{+3.29+2.20}_{-3.15-2.23}$	17
39	200-500	1200+	2	$1.73^{+0.79+0.20}_{-0.62-0.19}$	$1.89^{+0.88+0.18}_{-0.75-0.18}$	$1.06^{+0.38+0.61}_{-0.38-0.58}$	$3.30^{+0.61+1.61}_{-0.52-1.61}$	$7.97^{+1.81+1.74}_{-1.51-1.73}$	4
40	500-750	500-1200	2	$0.00^{+0.39+0.00}_{-0.00-0.00}$	$0.04^{+0.46+0.01}_{-0.02-0.01}$	$0.06^{+0.07+0.03}_{-0.06-0.00}$	$0.00^{+0.11+0.03}_{-0.00-0.00}$	$0.10^{+0.86+0.05}_{-0.06-0.01}$	0
41	500-750	1200+	2	$0.00^{+0.43+0.00}_{-0.00-0.00}$	$0.07^{+0.47+0.04}_{-0.07-0.00}$	$0.11^{+0.08+0.06}_{-0.08-0.02}$	$0.03^{+0.10+0.05}_{-0.03-0.00}$	$0.21^{+0.90+0.08}_{-0.11-0.03}$	1
42	750+	800+	2	$0.00^{+0.34+0.00}_{-0.00-0.00}$	$0.13^{+0.48+0.06}_{-0.13-0.00}$	$0.10^{+0.07+0.07}_{-0.07-0.02}$	$0.00^{+0.08+0.02}_{-0.00-0.00}$	$0.23^{+0.82+0.08}_{-0.15-0.02}$	0
43	200-500	500-800	3+	$3.93^{+1.25+0.46}_{-1.16-0.45}$	$5.78^{+1.31+0.68}_{-1.23-0.67}$	$2.54^{+1.50+1.76}_{-1.50-1.04}$	$1.06^{+0.60+0.88}_{-0.40-0.66}$	$13.31^{+3.03+2.13}_{-2.85-1.47}$	3
44	200-500	800-1200	3+	$0.44^{+0.49+0.05}_{-0.25-0.05}$	$1.66^{+0.76+0.26}_{-0.60-0.26}$	$1.60^{+0.96+1.11}_{-0.96-0.65}$	$0.58^{+0.30+0.40}_{-0.21-0.37}$	$4.28^{+1.60+1.21}_{-1.30-0.79}$	4
45	200-500	1200+	3+	$0.66^{+0.72+0.12}_{-0.52-0.12}$	$0.65^{+0.61+0.10}_{-0.40-0.10}$	$0.56^{+0.35+0.42}_{-0.35-0.21}$	$0.05^{+0.18+0.11}_{-0.00-0.05}$	$1.92^{+1.39+0.46}_{-0.99-0.27}$	1
46	500-750	500-1200	3+	$0.00^{+0.52+0.00}_{-0.00-0.00}$	$0.00^{+0.46+0.00}_{-0.00-0.00}$	$0.03^{+0.04+0.02}_{-0.03-0.00}$	$0.04^{+0.09+0.06}_{-0.03-0.01}$	$0.07^{+0.98+0.06}_{-0.05-0.01}$	0
47	500-750	1200+	3+	$0.00^{+0.47+0.00}_{-0.00-0.00}$	$0.00^{+0.46+0.00}_{-0.00-0.00}$	$0.06^{+0.05+0.04}_{-0.05-0.00}$	$0.00^{+0.09+0.01}_{-0.00-0.00}$	$0.06^{+0.94+0.04}_{-0.05-0.00}$	0
48	750+	800+	3+	$0.00^{+0.61+0.00}_{-0.00-0.00}$	$0.01^{+0.46+0.01}_{-0.01-0.00}$	$0.05^{+0.05+0.05}_{-0.05-0.00}$	$0.00^{+0.08+0.02}_{-0.00-0.00}$	$0.06^{+1.07+0.05}_{-0.05-0.00}$	0

Table 7.3: Observed number of events and background predictions in the $N_{\text{jet}} \geq 9$ search bins.

Bin	$H_{\text{T}}^{\text{miss}}$ [GeV]	H_{T} [GeV]	$N_{\text{b-jet}}$	Lost-e/μ	τ_{h}	$\text{Z} \to \nu\bar{\nu}$	QCD	Total Pred.	Obs.
49	200-500	500-800	0	$0.99^{+0.59+0.21}_{-0.45-0.21}$	$0.61^{+0.52+0.09}_{-0.23-0.09}$	$0.26^{+0.26+0.12}_{-0.26-0.00}$	$0.84^{+0.49+0.77}_{-0.32-0.52}$	$2.69^{+1.24+0.81}_{-0.80-0.57}$	2
50	200-500	800-1200	0	$2.12^{+0.72+0.33}_{-0.62-0.33}$	$3.92^{+1.17+0.41}_{-1.08-0.41}$	$2.14^{+0.81+0.81}_{-0.81-0.64}$	$0.71^{+0.29+0.54}_{-0.21-0.50}$	$8.89^{+2.08+1.11}_{-1.90-0.97}$	12
51	200-500	1200+	0	$0.58^{+0.54+0.08}_{-0.35-0.08}$	$1.05^{+0.76+0.16}_{-0.61-0.15}$	$0.42^{+0.30+0.18}_{-0.30-0.12}$	$3.46^{+0.59+2.31}_{-0.51-2.31}$	$5.51^{+1.46+2.32}_{-1.12-2.32}$	8
52	500-750	500-1200	0	$0.00^{+0.34+0.00}_{-0.00-0.00}$	$0.00^{+0.46+0.00}_{-0.00-0.00}$	$0.15^{+0.15+0.11}_{-0.15-0.00}$	$0.00^{+0.10+0.04}_{-0.00-0.00}$	$0.15^{+0.82+0.11}_{-0.15-0.00}$	0
53	500-750	1200+	0	$0.14^{+0.36+0.05}_{-0.14-0.00}$	$0.02^{+0.46+0.01}_{-0.02-0.00}$	$0.00^{+0.76+0.00}_{-0.00-0.00}$	$0.00^{+0.08+0.04}_{-0.00-0.00}$	$0.17^{+1.13+0.04}_{-0.17-0.00}$	0
54	750+	800+	0	$0.00^{+0.28+0.00}_{-0.00-0.00}$	$0.00^{+0.46+0.00}_{-0.00-0.00}$	$0.00^{+0.79+0.00}_{-0.00-0.00}$	$0.00^{+0.07+0.04}_{-0.00-0.00}$	$0.00^{+1.09+0.04}_{-0.00-0.00}$	0
55	200-500	500-800	1	$1.36^{+0.66+0.20}_{-0.53-0.19}$	$1.58^{+0.71+0.19}_{-0.54-0.19}$	$0.19^{+0.19+0.10}_{-0.19-0.00}$	$0.08^{+0.20+0.13}_{-0.07-0.01}$	$3.21^{+1.39+0.31}_{-1.08-0.27}$	6
56	200-500	800-1200	1	$3.19^{+0.99+0.53}_{-0.91-0.52}$	$4.05^{+1.17+0.37}_{-1.08-0.36}$	$1.57^{+0.64+0.70}_{-0.64-0.67}$	$0.75^{+0.30+0.58}_{-0.22-0.53}$	$9.55^{+2.27+1.11}_{-2.10-1.06}$	4
57	200-500	1200+	1	$1.70^{+0.85+0.25}_{-0.73-0.25}$	$1.41^{+0.79+0.25}_{-0.65-0.25}$	$0.31^{+0.22+0.15}_{-0.22-0.08}$	$2.20^{+0.49+1.56}_{-0.40-1.56}$	$5.62^{+1.72+1.61}_{-1.45-1.60}$	3
58	500-750	500-1200	1	$0.00^{+0.40+0.00}_{-0.00-0.00}$	$0.05^{+0.46+0.02}_{-0.05-0.00}$	$0.11^{+0.11+0.08}_{-0.11-0.00}$	$0.00^{+0.10+0.03}_{-0.00-0.00}$	$0.16^{+0.87+0.09}_{-0.12-0.00}$	0
59	500-750	1200+	1	$0.00^{+0.41+0.00}_{-0.00-0.00}$	$0.15^{+0.48+0.04}_{-0.14-0.00}$	$0.00^{+0.66+0.00}_{-0.00-0.00}$	$0.00^{+0.08+0.02}_{-0.00-0.00}$	$0.15^{+1.11+0.02}_{-0.14-0.00}$	1
60	750+	800+	1	$0.00^{+0.33+0.00}_{-0.00-0.00}$	$0.00^{+0.46+0.00}_{-0.00-0.00}$	$0.00^{+0.68+0.00}_{-0.00-0.00}$	$0.00^{+0.07+0.02}_{-0.00-0.00}$	$0.00^{+1.05+0.02}_{-0.00-0.00}$	0
61	200-500	500-800	2	$1.38^{+0.74+0.18}_{-0.62-0.17}$	$1.51^{+0.77+0.15}_{-0.61-0.15}$	$0.10^{+0.11+0.07}_{-0.10-0.00}$	$0.00^{+0.20+0.08}_{-0.00-0.00}$	$3.00^{+1.53+0.25}_{-1.23-0.23}$	3
62	200-500	800-1200	2	$1.39^{+0.68+0.20}_{-0.57-0.20}$	$2.20^{+0.92+0.20}_{-0.80-0.20}$	$0.87^{+0.41+0.54}_{-0.41-0.46}$	$0.24^{+0.20+0.23}_{-0.12-0.12}$	$4.70^{+1.67+0.65}_{-1.43-0.55}$	1
63	200-500	1200+	2	$0.28^{+0.48+0.04}_{-0.20-0.04}$	$1.40^{+0.83+0.19}_{-0.70-0.19}$	$0.17^{+0.13+0.11}_{-0.13-0.04}$	$1.23^{+0.40+0.90}_{-0.31-0.90}$	$3.09^{+1.39+0.93}_{-0.96-0.92}$	2
64	500-750	500-1200	2	$0.00^{+0.36+0.00}_{-0.00-0.00}$	$0.00^{+0.46+0.00}_{-0.00-0.00}$	$0.06^{+0.06+0.05}_{-0.06-0.00}$	$0.00^{+0.10+0.03}_{-0.00-0.00}$	$0.06^{+0.83+0.06}_{-0.06-0.00}$	0
65	500-750	1200+	2	$0.00^{+0.45+0.00}_{-0.00-0.00}$	$0.01^{+0.46+0.00}_{-0.01-0.00}$	$0.00^{+0.52+0.00}_{-0.00-0.00}$	$0.00^{+0.08+0.02}_{-0.00-0.00}$	$0.01^{+1.05+0.02}_{-0.01-0.00}$	0
66	750+	800+	2	$0.00^{+0.43+0.00}_{-0.00-0.00}$	$0.00^{+0.46+0.00}_{-0.00-0.00}$	$0.00^{+0.52+0.00}_{-0.00-0.00}$	$0.00^{+0.07+0.02}_{-0.00-0.00}$	$0.00^{+1.04+0.02}_{-0.00-0.00}$	0
67	200-500	500-800	3+	$0.30^{+0.48+0.05}_{-0.21-0.05}$	$1.13^{+0.79+0.16}_{-0.64-0.16}$	$0.02^{+0.03+0.03}_{-0.02-0.00}$	$0.00^{+0.20+0.05}_{-0.00-0.00}$	$1.46^{+1.28+0.18}_{-0.85-0.17}$	0
68	200-500	800-1200	3+	$1.92^{+1.38+0.33}_{-1.33-0.32}$	$0.70^{+0.60+0.09}_{-0.38-0.09}$	$0.18^{+0.13+0.24}_{-0.13-0.06}$	$0.25^{+0.20+0.23}_{-0.11-0.14}$	$3.06^{+1.99+0.47}_{-1.72-0.37}$	1
69	200-500	1200+	3+	$0.46^{+0.64+0.06}_{-0.46-0.00}$	$0.32^{+0.54+0.05}_{-0.28-0.04}$	$0.04^{+0.03+0.05}_{-0.03-0.00}$	$0.03^{+0.09+0.06}_{-0.03-0.00}$	$0.85^{+1.19+0.09}_{-0.75-0.04}$	0
70	500-750	500-1200	3+	$0.13^{+0.47+0.05}_{-0.13-0.00}$	$0.00^{+0.46+0.00}_{-0.00-0.00}$	$0.01^{+0.02+0.02}_{-0.01-0.00}$	$0.00^{+0.10+0.02}_{-0.00-0.00}$	$0.14^{+0.93+0.03}_{-0.13-0.00}$	0
71	500-750	1200+	3+	$0.00^{+0.41+0.00}_{-0.00-0.00}$	$0.00^{+0.46+0.00}_{-0.00-0.00}$	$0.00^{+0.30+0.00}_{-0.00-0.00}$	$0.00^{+0.08+0.01}_{-0.00-0.00}$	$0.00^{+0.92+0.01}_{-0.00-0.00}$	0
72	750+	800+	3+	$0.00^{+0.44+0.00}_{-0.00-0.00}$	$0.00^{+0.46+0.00}_{-0.00-0.00}$	$0.00^{+0.28+0.00}_{-0.00-0.00}$	$0.00^{+0.07+0.02}_{-0.00-0.00}$	$0.00^{+0.95+0.02}_{-0.00-0.00}$	0

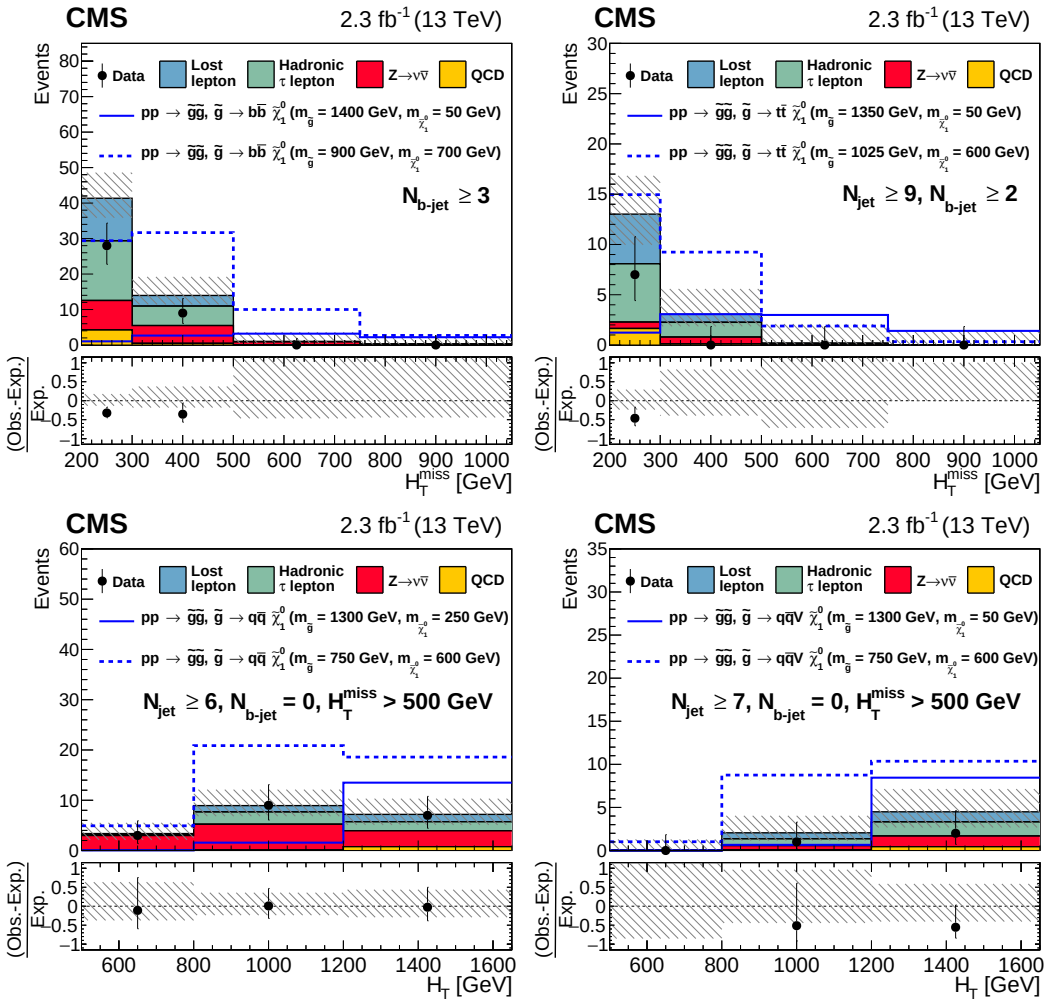

Figure 7.2: Observed numbers of events and corresponding background predictions for intervals of the search region phase space particularly sensitive to the (top left) T1bbbb, (top right) T1tttt, (bottom left) T1qqqq, and (bottom right) T5qqqqVV scenarios. The selection requirements are given in the figure legends with the hatched regions showing the total uncertainties in the background predictions. The (unstacked) results for two example signal scenarios are shown in each case. Note that for purposes of presentation, the $H_{\mathrm{T}}^{\mathrm{miss}}$ variable uses the QCD fine binning structure with 4 bins.

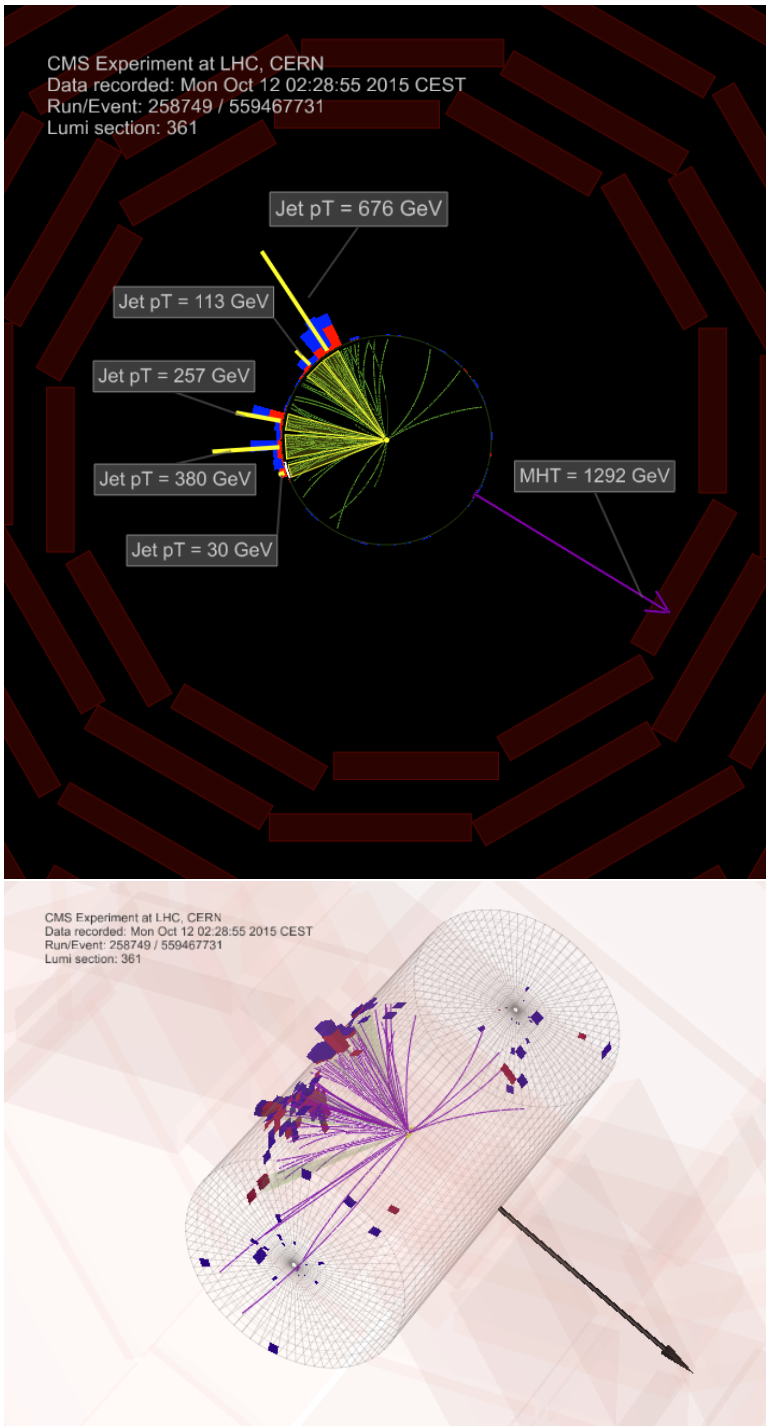

Figure 7.3: The event display of an event which has the largest $H_{\mathrm{T}}^{\mathrm{miss}}$ of any event in the signal region. Two views are shown, the r$-\phi$ plane on the top and a 3-D view on the bottom. Jets are marked in yellow, ECAL deposits in red, HCAL deposits in blue, tracks in green, and $H_{\mathrm{T}}^{\mathrm{miss}}$ in purple. Note that the tracks have a 1.5 GeV threshold in order to be shown.

7.2 Signal Systematic Uncertainties

The exclusion limits are set using simulated signal events, but potential signal would be measured not simulated. Recall the four signal models considered in this analysis are the T1bbbb, T1tttt, T1qqqq, and T5qqqqVV samples, given in Sec. 5.1.3. Then data and simulation differences must be accounted for in these signal events. An array of uncertainties are considered and evaluated. These uncertainties are fully summarized in Tab. 7.4.

Plots of the signal selection efficiency times the signal acceptance for the four signal scenarios are given in Fig. 7.4. These plots show sensitivity to a wide array of points within a SMS scenario, as this analysis can probe model points with large and small gluino and LSP mass differences. In all four models there is a drop in efficiency as the diagonal (i.e. the as the difference between gluino and LSP mass decreases) is approached. This is because as the difference between the gluino and LSP mass becomes smaller, the $H_{\mathrm{T}}^{\mathrm{miss}}$ spectrum becomes softer. This softer spectrum means the minimum $H_{\mathrm{T}}^{\mathrm{miss}}$ requirement applied in the analysis will reject a greater proportion of events. One reason the $H_{\mathrm{T}}^{\mathrm{miss}}$ spectrum drops is because the available energy for the LSP also becomes smaller. This means its momentum will also be smaller, implying the missing energy of the event will also be reduced.

Table 7.4: Summary of systematic uncertainties with the results averaged over all search bins. The variations, in the second column, correspond to different signal models and choices of the gluino and LSP masses. The last column shows how the signal is affected: the signal event selection efficiency and signal distribution shape, i.e. causing events to migrate from one signal bin to another.

Item	Relative Uncertainty (%)	Signal Effect
Luminosity: Accounting for the integrated luminosity measurement uncertainty	4.6	efficiency
Isolated track veto: Accounting for isolated track and lepton veto efficiency uncertainties	2.0	efficiency
Jet ID: Accounting for efficiency of the jet quality event cut	1.0	efficiency
***b*-tag efficiency**: Accounting for efficiency of tagging and mistagging of b-jets.	-	shape
Trigger efficiency: Accounting for the trigger efficiency measured in data	0.5-1.1	efficiency & shape
Pileup reweighting: Accounting for Pileup reweighting correction uncertainties owing to differences in actual and observed number of interactions per event	0.1-0.5	efficiency & shape
QCD Scales: Accounting for renormalization and factorization scale uncertainties	0.1-3.0	efficiency & shape
Initial State Radiation: Accounting for the uncertainty related to initial-state radiation (ISR) modeling	0.02-10.0	efficiency & shape
Jet energy scale: Accounting for the uncertainty related to jet energy corrections, dependent on jet p_T and η	0.5-4.0	efficiency & shape
Simulation statistics: Accounting for the statistical precision of the signal simulation	-	shape
Total	1.5-11.0	

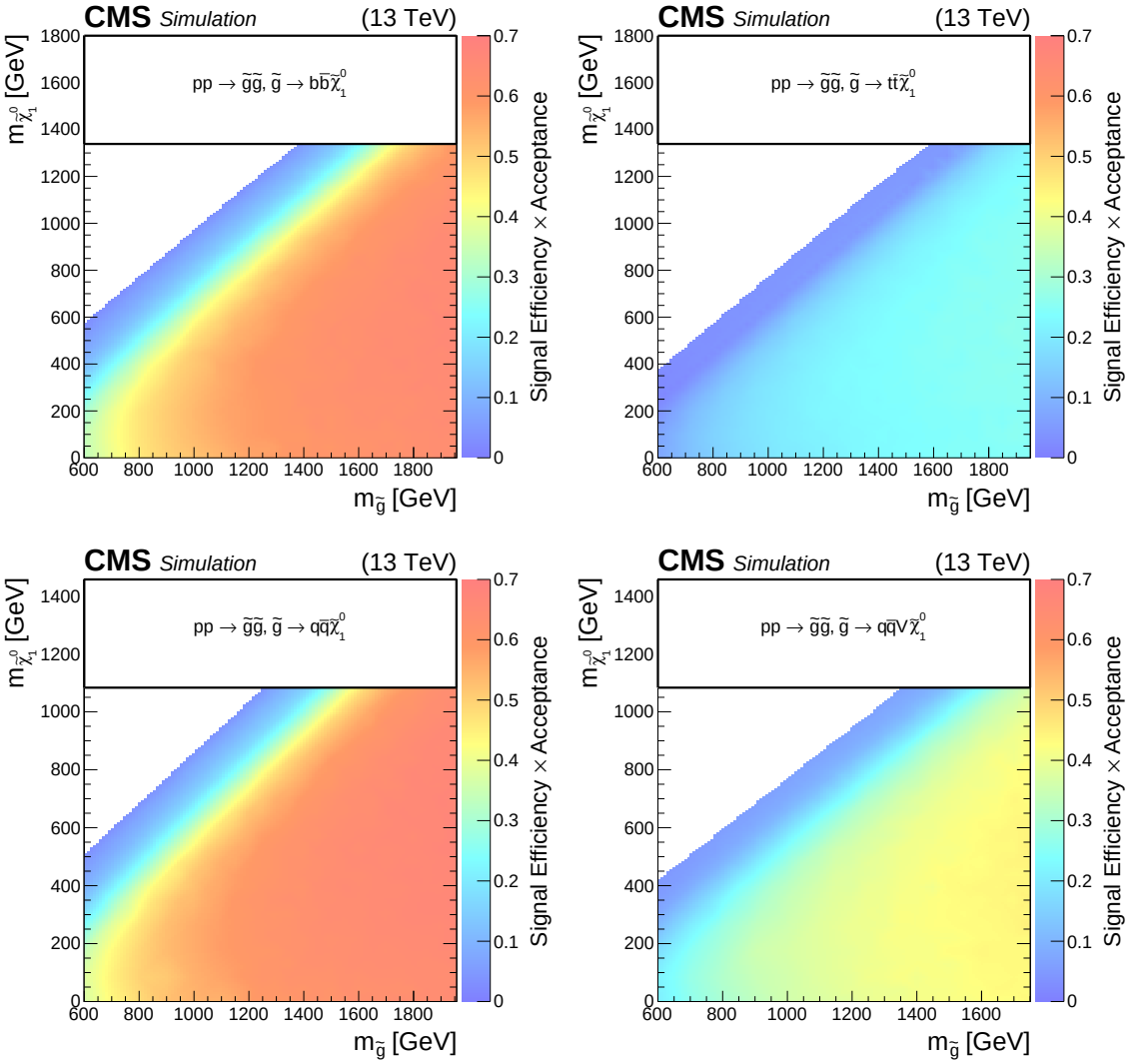

Figure 7.4: Plots of the signal efficiency after the baseline selection for the four SMS scenarios: T1bbbb (top left), T1tttt (top right), T1qqqq (bottom left), and T5qqqqVV (bottom right).

7.3 Interpretation of results

Because no evidence of SUSY is found in the analysis, it is prudent to use a statistical model to exclude or limit the available parameter space in SUSY. The SMS models are used in this context. The statistical methodology used is taken from the one jointly developed by CMS and ATLAS: a modified-frequentist CL_s method with one-sided profile likelihood test statistic [68–70].

7.3.1 Statistical Procedure

The signal strength, μ, is the scale for the signal cross section for each SUSY model. When μ is set to 1, this means the signal cross section is set to the predicted cross section. The uncertainties in the signal region yields and background predictions are handled by nuisance parameters, θ. Because the true value of θ, $\tilde{\theta}$, is unknown, probability density functions (pdfs) of the form $p(\tilde{\theta}|\theta)$ are used to describe them. The likelihood, $\mathcal{L}$, is then a function of the signal strength, μ, the uncertainty nuisance parameters, θ, and the observed data, n, and has the functional form:

$$\mathcal{L}(n|\mu,\theta) = \mathrm{P}(n|\mu\cdot\mathrm{s}(\theta)+\mathrm{b}(\theta))\cdot p(\tilde{\theta}|\theta). \tag{7.1}$$

The $\mathrm{P}(n|\mu\cdot\mathrm{s}(\theta)+\mathrm{b}(\theta))$ pdf term is the product of Poisson probabilities to observe n events given the signal and background yields $\mu\cdot\mathrm{s}$ and b respectively in each search region of the analysis. A test statistic, $\tilde{\mathrm{q}}_\mu$, is constructed to compare the compatibility of data with the 'signal+background' or 'background-only' hypotheses:

$$\tilde{\mathrm{q}}_\mu = -2\ln\frac{\mathcal{L}(n|\mu,\hat{\theta}_\mu)}{\mathcal{L}(n|\hat{\mu},\hat{\theta})}, \quad \text{with } 0 \geq \tilde{\mu} \geq \mu. \tag{7.2}$$

The $\hat{\mu}$ and $\hat{\theta}$ parameters refer to the global maximum likelihood, while $\hat{\theta}_\mu$ maximizes the likelihood for a given μ. In order to force the one-sided, or asymptotic, confidence limits, $\tilde{\mu} \geq \mu$ is required. For a given μ, $\tilde{\mathrm{q}}_\mu^{obs}$ is determined and $\hat{\theta}_0^{obs}$ and $\hat{\theta}_\mu^{obs}$ are the values for

the 'background-only' $\mu = 0$ and the 'signal+background' hypothesis, respectively, which maximize the likelihood. The Poisson pdfs, $\mathrm{P}(n|\mu \cdot \mathrm{s}(\theta) + \mathrm{b}(\theta))$, are used to generate toy Monte Carlo simulated events assuming μ for the 'signal+background' hypothesis and $\mu = 0$ for the 'background-only' hypothesis. The probabilities then to obtain larger test statistic, $\tilde{\mathrm{q}}_\mu$, than the observed one, $\tilde{\mathrm{q}}_\mu^{obs}$, for the 'signal+background' and 'background-only' hypotheses are

$$\mathrm{CL}_{s+b} = \mathrm{P}(\tilde{\mathrm{q}}_\mu > \tilde{\mathrm{q}}_\mu^{obs}|\mu \cdot \mathrm{s} + \mathrm{b}) \text{ and} \tag{7.3}$$

$$\mathrm{CL}_b = \mathrm{P}(\tilde{\mathrm{q}}_\mu > \tilde{\mathrm{q}}_\mu^{obs}|\mathrm{b}). \tag{7.4}$$

Finally, the CL_s can be obtained from the ratio

$$\mathrm{CL}_s = \frac{\mathrm{CL}_{s+b}}{\mathrm{CL}_b} \leq (1 - 95\%) = 0.05, \tag{7.5}$$

which is the oft-quoted 95% confidence upper limit. For each signal model, the inequality is solved for μ. If a signal has $\mu \leq 1$, that signal is said then to be excluded at 95% confidence level. By scanning over the two-dimensional mass plane of SMS models, the contour line with $\mu = 1$ is the 'limit' and marks the edge of the excluded region.

It is worth noting the signal contamination of the control samples is evaluated by reducing the efficiency of the signal model under analysis. This is done to account for the fact that the SM background estimation could be affected by the potential signal contamination in the data control samples used in the background estimation techniques.

7.3.2 Exclusion Limits

Presented in Fig. 7.5, 7.6, 7.7, and 7.8, are the 95% CL exclusion limits in the two-dimensional gluino mass-neutralino mass space. Given a nearly massless neutralino, the assumed LSP, gluinos are excluded with masses below 1600, 1550, 1440, and 1450 GeV, for

the T1bbbb, T1tttt, T1qqqq, and T5qqqqVV scenarios, respectively. This represents a large increase in the limits obtained from the previous iterations of this analysis. Previously, the three T1 models had a gluino mass limit around 1150 GeV for a nearly massless neutralino [64, 65]. For the T5qqqqVV model, the gluino mass limit was 1280 GeV for a nearly massless neutralino [65]. The reason for the much better performance is because of the enhanced signal cross section compared to background cross sections. For instance, the $t\bar{t}$ cross section, which is a dominant background in this analysis, increases by a factor of 4. But for a gluino mass of 1500 GeV, the cross section increases by a factor of 30.

Additional signal scenarios to the four already discussed have been interpreted as well. These supplementary signal scenarios are described and shown in App. C.

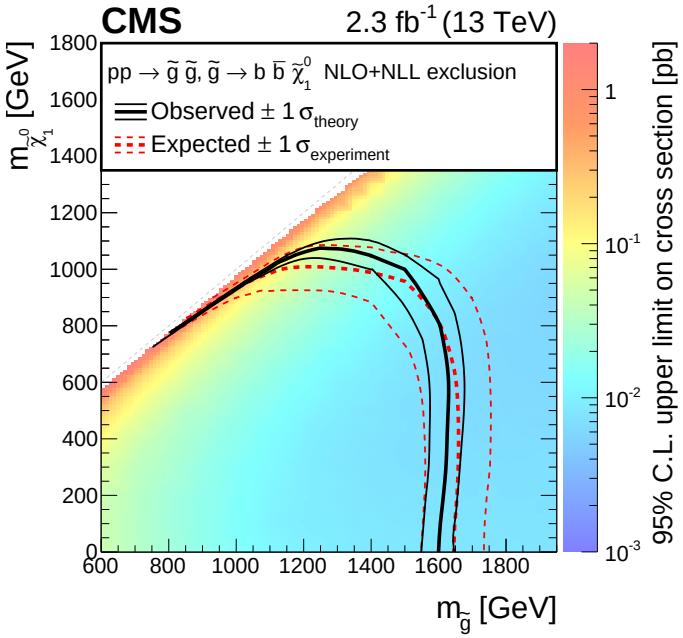

Figure 7.5: The observed and expected upper limits exclusion at 95% confidence level for the T1bbbb scenario.

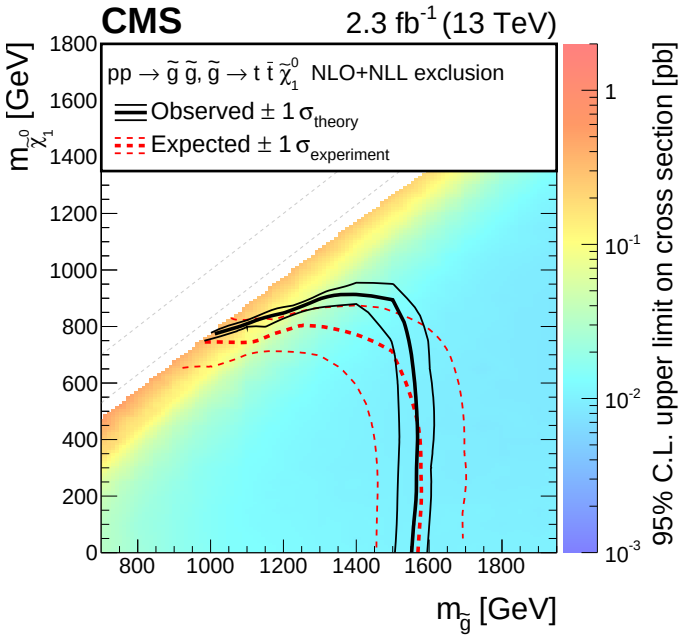

Figure 7.6: The observed and expected upper limits exclusion at 95% confidence level for the T1tttt scenario.

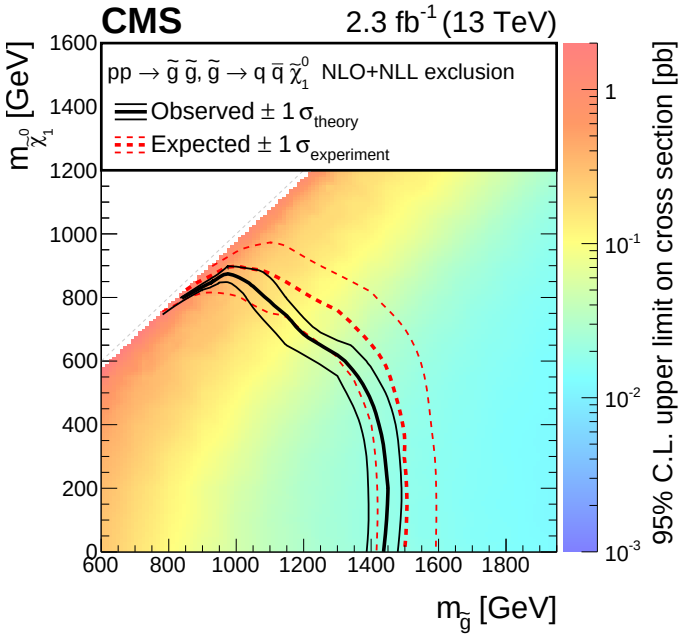

Figure 7.7: The observed and expected upper limits exclusion at 95% confidence level for the T1qqqq scenario.

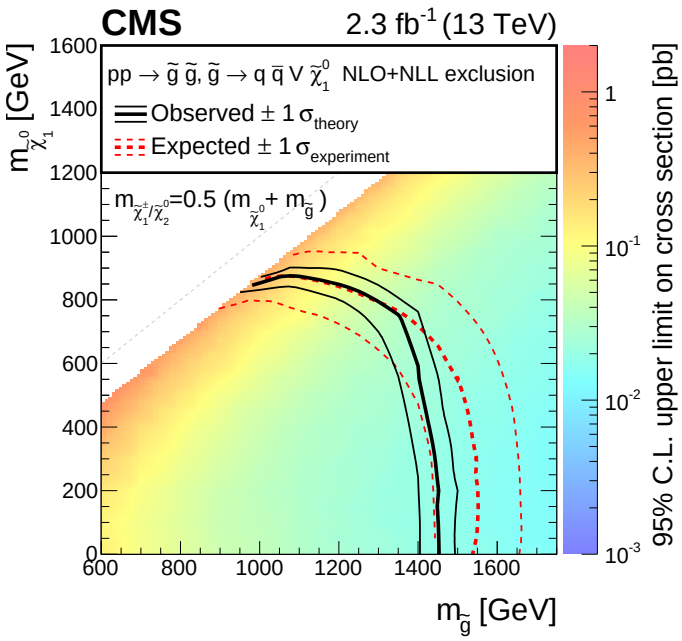

Figure 7.8: The observed and expected upper limits exclusion at 95% confidence level for the T5qqqqVV scenario.

Chapter 8

Conclusions

This dissertation was only made possible by the fantastic effort and work of the LHC and its accelerator staff. In addition, the tremendous accomplishments achieved by all CMS collaborators cannot be understated. The results from the early running periods of the LHC is certainly highlighted by the discovery of a new boson compatible with the Higgs boson by the CMS and ATLAS experiments. Other results from CMS include measurement of a rare B_s^0 decay to $\mu^+\mu^-$ [71] and a new excited bottom baryon, Ξ_b^{*0} [72]. The LHC has provided excellent conditions in the search for new physics phenomena.

As this dissertation has presented, a search for SUSY was performed [63]. This search analyzed pp collision data at $\sqrt{s} = 13$ TeV collected in 2015 by the CMS experiment. The data corresponds to an integrated luminosity of $2.3\,\text{fb}^{-1}$.

Events were selected in hadronic final states only, rejecting all events with identified, isolated electrons or muons and isolated charged tracks. Events must also have at least four jets, large missing transverse momentum (H_T^miss), and large scalar sum of jet transverse momenta (H_T). The dominant backgrounds for this search are top quark and W boson plus jets processes, Z boson plus jets processes, and QCD multijet processes. These backgrounds are estimated using data-driven techniques from data control samples. Events are analyzed and binned in four dimensions: the number of jets, H_T, H_T^miss, and the number of bottom quark tagged jets.

Within uncertainties, the background predictions agreed with the observed event counts. Because of this, the results are interpreted with simplified models with generic topologies corresponding to gluino pair production. The gluino decay chain ends in the production of an undetected LSP: the neutralino, $\widetilde{\chi}_1^0$. In the T1bbbb model, the gluino decays to a bottom quark-antiquark pair, in the T1tttt model, the gluino decays to a top quark-antiquark pair, and in the T1qqqq model, the gluino decays to a light-flavored quark-antiquark pair. For all three of these models, the gluino decay to quark pairs occurs via an off-shell squark. In the T5qqqqVV model, the gluino decays to a light-flavored quark-antiquark pair and either the next-to-lightest neutralino, $\widetilde{\chi}_2^0$, or to the lightest-chargino $\widetilde{\chi}^{\pm}$, with the $\widetilde{\chi}_2^0$ ($\widetilde{\chi}^{\pm}$) decaying to the LSP and Z ($\mathrm{W}^{\pm}$). For the simplified models considered, the exclusion limits are significantly extended. Assuming a nearly massless LSP, gluinos are excluded with masses below 1600, 1550, 1440, and 1450 GeV for the T1bbbb, T1tttt, T1qqqq, and T5qqqqVV signal scenarios, respectively.

Part IV

Acronyms, Appendix, Bibliography, and Glossary

Acronyms

ALICE A Large Ion Collider Experiment. 16, 18

ATLAS A Toroidal LHC ApparatuS. 12, 16, 18, 100, 105

BPix Pixel barrel detector. 25

CERN European Organization for Nuclear Research. 12, 15, 36

CHS charged-hadron subtraction. 44

CMS Compact Muon Solenoid. 12, 13, 15, 16, 18–25, 27, 28, 30, 31, 33–39, 45, 49, 50, 100, 105

CS Control Sample. 64, 69, 74, 80

CSC Cathode Strip Chamber. 32

CSVv2 combined secondary vertex version2. 45, 46, 54

DT Drift Tube. 32

ECAL Electromagnetic Calorimeter. 26–30, 36, 37, 40–43, 96, 122, 123

EM electromagnetic. 26, 27

EVF event filter farm. 34

FPix Pixel forward detector. 25

GSF Gaussian sum filter. 42

HB Hadron Barrel. 29, 118, 119, 122, 123

HBHE Hadron barrel and endcap detectors. 118

HCAL Hadron Calorimeter. 29–31, 36, 37, 40, 42, 96, 118–125, 127

HE Hadron Endcap. 29, 118, 122–124

HF Hadron Forward. 29, 30, 118, 122

HLT High Level Trigger. 34–36

HO Hadron Outer. 29

HPD hybrid photodiode. 118

IVF Inclusive Vertex Fitter. 45

L1 Level 1 trigger. 34, 118, 125

L1CT Layer 1 Calo Trigger. 34, 118, 121

LEP Large Electron-Positron Collider. 12

LHC Large Hadron Collider. 12, 15–19, 22, 24, 49, 105

LHCb Large Hadron Collider beauty experiment. 16, 18

LSP lightest supersymmetric particle. 9, 12, 51, 52, 56, 58, 97, 98, 101, 106, 132, 134

LUT Look-Up Table. 119, 121

MSSM Minimal Supersymmetric Standard Model. 8, 9

OOTPU Out-Of-Time Pile-Up. 125, 127

PDF parton distribution function. 69

pdf probability density function. 100

PF Particle Flow. 39–41, 43, 44, 46, 47, 54, 66

PMT photomultiplier tube. 30, 118

PU Pile-Up. 19, 44, 51

PV primary vertex. 39, 41, 43, 45, 123

QCD Quantum Chromodynamics. 46, 50, 52, 53, 56, 57, 61–63, 80–82, 84–90, 95, 129

QIE Charge Integrator. 118, 119, 121

RF radio-frequency. 16

RH Reconstructed Hit. 122–124

RPC Resistive Plate Chamber. 32, 33

SM Standard Model. 4–7, 9, 15

SMS Simplified Model Spectra. 12, 13, 51, 97, 99–101, 132, *Glossary:* SMS

SUSY SUper SYmmetry. 7, 9–12, 15, 20, 45, 49, 55, 90, 100

TEC Tracker End Cap. 26

TIB Tracker Inner Barrel. 26

TID Tracker Inner Disk. 26

TOB Tracker Outer Barrel. 26

TP Trigger Primitive. 118–125, 127

TPG Trigger Primitive Generator. 34, 118, 127

TS Time Slice. 120

Glossary

χ^2 test A statistical test applied to two sets of data to determine the probability the difference between the two were by chance. 39, 82

boson A particle that follows Bose-Einstein statistics and has whole integer spin. 5, 105

fermion A particle that follows Fermi-Dirac statistics and has half integer spin. 5

gluon Fundamental boson force carriers for the strong nuclear force. There are eight types or colored gluons. 11, 43, 45

jet A narrow shower of particles produced from gluons and quarks decaying to particle-antiparticle pairs, a process also known as hadronization. 11

lepton Part of a fundamental group of fermions in the Standard Model. There are six types in three two-member families: $(e\nu_e)$, (μ, ν_μ), and (τ, ν_τ). 4

maximum likelihood A statistical method to estimate parameters of a model. Given a model for a set of data, the method selects the parameter models which maximize the likelihood function. 82, 84, 86–88

parton The initial particle coming from a hard scattering event which forms a jet in the final detector state. Usually a quark or gluon. 24, 43, 44

quark Part of a fundamental group of fermions in the Standard Model. There are six types in three two-member families:

(ub), (sc), and (tb). 4, 43

SMS A Simplified Model Spectra (SMS) is defined by a limited set of hypothetical particles and their sequence of production and decay. The free parameters are the particle masses and branching ratios. 12

T1bbbb A SMS signal model whose final state contains $b\bar{b}b\bar{b}$ and two LSPs. 52, 95, 97, 99, 102, 106

T1qqqq A SMS signal model whose final state contains $q\bar{q}q\bar{q}$ and two LSPs, where q is a first or second generation quark. 52, 95, 97, 99, 102, 103, 106

T1tttt A SMS signal model whose final state contains $t\bar{t}t\bar{t}$ and two LSPs. 52, 95, 97, 99, 102, 103, 106

T5qqqqVV A SMS signal model whose final state contains $q\bar{q}q\bar{q}$, two LSPs and two Z or W bosons, where q is a first or second generation quark. 52, 95, 97, 99, 102, 104

Bibliography

[1] E. Hubble, "The Exploration of Space", *Harper's Magazine* **158** (1929) 732. [2]

[2] J. Thomson, "Cathode Rays", *Philosophical Magazine* **44** (1897). [2]

[3] H. Spiesberger, M. Spira, and P. M. Zerwas, "The Standard model: Physical basis and scattering experiments", (2000) arXiv:hep-ph/0011255. [4]

[4] F. Englert and R. Brout, "Broken Symmetry and the Mass of Gauge Vector Mesons", *Phys. Rev. Lett.* **13** (Aug, 1964) 321–323, doi:10.1103/PhysRevLett.13.321. [5]

[5] UA1 Collaboration, "Experimental Observation of Lepton Pairs of Invariant Mass Around 95 GeV/c^2 at the CERN SPS Collider", *Phys. Lett.* **B126** (1983) 398–410, doi:10.1016/0370-2693(83)90188-0. [5]

[6] UA2 Collaboration, "Evidence for $Z^0 \to e^+e^-$ at the CERN $\bar{p}p$ Collider", *Phys. Lett.* **B129** (1983) 130–140, doi:10.1016/0370-2693(83)90744-X. [5]

[7] J. Bagdonaite et al., "A Stringent Limit on a Drifting Proton-to-Electron Mass Ratio from Alcohol in the Early Universe", *Science* **339** (2013), no. 6115, 46–48, doi:10.1126/science.1224898. [5]

[8] SLD Electroweak Group, DELPHI, ALEPH, SLD, SLD Heavy Flavour Group, OPAL, LEP Electroweak Working Group, L3 Collaboration, "Precision electroweak measurements on the Z resonance", *Phys. Rept.* **427** (2006) 257–454, doi:10.1016/j.physrep.2005.12.006, arXiv:hep-ex/0509008. [5]

[9] G. S. Guralnik, C. R. Hagen, and T. W. B. Kibble, "Global Conservation Laws and Massless Particles", *Phys. Rev. Lett.* **13** (Nov, 1964) 585–587, doi:10.1103/PhysRevLett.13.585. [5]

[10] P. W. Higgs, "Broken Symmetries and the Masses of Gauge Bosons", *Phys. Rev. Lett.* **13** (Oct, 1964) 508–509, doi:10.1103/PhysRevLett.13.508. [5]

[11] ATLAS Collaboration, "Observation of a new particle in the search for the Standard Model Higgs boson with the ATLAS detector at the LHC", *Phys. Lett.* **B716** (2012) 1–29, doi:10.1016/j.physletb.2012.08.020, arXiv:1207.7214. [5]

[12] CMS Collaboration, "Observation of a new boson at a mass of 125 GeV with the CMS experiment at the LHC", *Phys. Lett.* **B716** (2012) 30–61, doi:10.1016/j.physletb.2012.08.021, arXiv:1207.7235. [5]

[13] J. Maxwell, "On physical lines of force", *Philosophical Magazine* **90** (2010), no. sup1, 11–23, doi:10.1080/14786431003659180. [6]

[14] S. P. Martin, "A Supersymmetry primer", doi:10.1142/9789812839657_0001,10.1142/9789814307505_0001, arXiv:hep-ph/9709356. [Adv. Ser. Direct. High Energy Phys. 18, 1 (1998)]. [7]

[15] K. Freese, "Can scalar neutrinos or massive Dirac neutrinos be the missing mass?", *Physics Letters B* **167** (1986), no. 3, 295 – 300, doi:10.1016/0370-2693(86)90349-7. [7]

[16] V. C. Rubin and W. K. Ford, Jr., "Rotation of the Andromeda Nebula from a Spectroscopic Survey of Emission Regions", *Astrophysics. J.* **159** (February, 1970) 379, doi:10.1086/150317. [7]

[17] AMS Collaboration, "First Result from the Alpha Magnetic Spectrometer on the International Space Station: Precision Measurement of the Positron Fraction in Primary Cosmic Rays of 0.5 - 350 GeV", *Phys. Rev. Lett.* **110** (2013) 141102, doi:10.1103/PhysRevLett.110.141102. [7]

[18] M. Drees, "An Introduction to supersymmetry", in *Current topics in physics. Proceedings, Inauguration Conference of the Asia-Pacific Center for Theoretical Physics (APCTP), Seoul, Korea, June 4-10, 1996. Vol. 1, 2.* 1996. arXiv:hep-ph/9611409. [7 and 8]

[19] S. Dimopoulos and H. Georgi, "Softly Broken Supersymmetry and SU(5)", *Nucl. Phys.* **B193** (1981) 150, doi:10.1016/0550-3213(81)90522-8. [7 and 8]

[20] P. Pralavorio, "Particle Physics and Cosmology", in *100e Ecole d'Ete de Physique: Post-Planck Cosmology Les Houches, France, July 8-August 2, 2013*, pp. 353–405. 2015. arXiv:1311.1769. doi:10.1093/acprof:oso/9780198728856.003.0008. [9]

[21] H. K. Dreiner, "An Introduction to explicit R-parity violation", doi:10.1142/9789814307505_0017, arXiv:hep-ph/9707435. [Adv. Ser. Direct. High Energy Phys. 21, 565 (2010)]. [8]

[22] K. A. Intriligator and N. Seiberg, "Lectures on Supersymmetry Breaking", *Class. Quant. Grav.* **24** (2007) S741–S772, doi:10.1088/0264-9381/24/21/S02,10.1016/S0924-8099(08)80020-0, arXiv:hep-ph/0702069. [125 (2007)]. [10]

[23] S. Ask, "A Review of the supersymmetry searches at LEP", in *38th Rencontres de Moriond on Electroweak Interactions and Unified Theories Les Arcs, France, March 15-22, 2003.* 2003. arXiv:hep-ex/0305007. [12]

[24] CDF and D0 Collaborations, "SUSY Searches at the Tevatron", in *Hadron collider physics. Proceedings, 19th Symposium, HCP2008, Galena, USA, May 27-31, 2008.* 2008. arXiv:0808.0728. [12]

[25] CMS Collaboration, "Summary of comparison plots in simplified models spectra for the 8 TeV dataset". https://twiki.cern.ch/twiki/pub/CMSPublic/PhysicsResultsSUS/barplot_ICHEP2014_2.pdf. Accessed: 2015-11-03. [13]

[26] L. R. Evans and P. Bryant, "LHC Machine", *J. Instrum.* **3** (2008) S08001. 164 p. This report is an abridged version of the LHC Design Report (CERN-2004-003). [15]

[27] "CERN Accelerator Complex". http://public-archive.web.cern.ch/public-archive/Objects/Research/AccComplex0700829.gif. Accessed: 2015-11-30. [17]

[28] CMS Collaboration, "The CMS experiment at the CERN LHC", *JINST* **3** (2008) S08004, doi:10.1088/1748-0221/3/08/S08004. [16 and 19]

[29] ATLAS Collaboration, "The ATLAS Experiment at the CERN Large Hadron Collider", *JINST* **3** (2008) S08003, doi:10.1088/1748-0221/3/08/S08003. [16]

[30] LHCb Collaboration, "The LHCb Detector at the LHC", *JINST* **3** (2008) S08005, doi:10.1088/1748-0221/3/08/S08005. [16]

[31] ALICE Collaboration, "The ALICE experiment at the CERN LHC", *JINST* **3** (2008) S08002, doi:10.1088/1748-0221/3/08/S08002. [16]

[32] CERN, "Overall view of the LHC experiments". http://atlas.ch/atlas_photos/selected-photos/lhc/9906026_01_layout_sch.jpg. Accessed: 2015-11-20. [18]

[33] CMS Collaboration, "CMS Luminosity - Public Results". http://cms-service-lumi.web.cern.ch/cms-service-lumi/publicplots. Accessed: 2015-11-10. [19 and 20]

[34] CMS Collaboration, "CMS Physics: Technical Design Report Volume 1: Detector Performance and Software". Technical Design Report CMS. CERN, Geneva, 2006. [21, 25, 121, and 122]

[35] CMS Collaboration, "CMS detector - Perspective view". http://www-collider.physics.ucla.edu/cms/CMS_3D_Detector_50.gif. Accessed: 2015-11-10. [22]

[36] CMS Collaboration, "Energy Calibration and Resolution of the CMS Electromagnetic Calorimeter in pp Collisions at $\sqrt{s} = 7$ TeV", *JINST* **8** (2013) P09009, doi:10.1088/1748-0221/8/09/P09009, arXiv:1306.2016. [27 and 28]

[37] CMS Collaboration, "Performance of the CMS Hadron Calorimeter with Cosmic Ray Muons and LHC Beam Data", *JINST* **5** (2010) T03012, doi:10.1088/1748-0221/5/03/T03012, arXiv:0911.4991. [30]

[38] CMS Collaboration, "Using Russian navy shells". http://cms.web.cern.ch/news/using-russian-navy-shells. Accessed: 2015-11-29. [31]

[39] CMS Collaboration, "Performance of CMS muon reconstruction in pp collision events at $\sqrt{s} = 7$ TeV", *JINST* **7** (2012) P10002, doi:10.1088/1748-0221/7/10/P10002, arXiv:1206.4071. [31, 33, and 40]

[40] CMS Collaboration, "CMS Technical Design Report for the Level-1 Trigger Upgrade", Technical Report CERN-LHCC-2013-011. CMS-TDR-12, CERN, Geneva, Jun, 2013. [35]

[41] CMS Trigger and Data Acquisition Group Collaboration, "The CMS high level trigger", *Eur. Phys. J.* **C46** (2006) 605–667, doi:10.1140/epjc/s2006-02495-8, arXiv:hep-ex/0512077. [35]

[42] CMS Collaboration, "Interactive Slice of the CMS detector". https://cms-docdb.cern.ch/cgi-bin/PublicDocDB/ShowDocument?docid=4172. Accessed: 2015-12-04. [37]

[43] CMS Collaboration, "Description and performance of track and primary-vertex reconstruction with the CMS tracker", *JINST* **9** (2014), no. 10, P10009, doi:10.1088/1748-0221/9/10/P10009, arXiv:1405.6569. [38 and 39]

[44] R. Frühwirth, "Application of Kalman filtering to track and vertex fitting", *Nuclear Instruments and Methods in Physics Research Section A: Accelerators, Spectrometers, Detectors and Associated Equipment* **262** (1987), no. 2 - 3, 444 – 450, doi:10.1016/0168-9002(87)90887-4. [38]

[45] CMS Collaboration, "Particle-Flow Event Reconstruction in CMS and Performance for Jets, Taus, and MET", Technical Report CMS-PAS-PFT-09-001, CERN, 2009. Geneva, Apr, 2009. [39]

[46] CMS Collaboration, "Commissioning of the Particle-flow Event Reconstruction with the first LHC collisions recorded in the CMS detector", Technical Report CMS-PAS-PFT-10-001, 2010. [39]

[47] CMS Collaboration, "Baseline muon selections for Run-II". https://twiki.cern.ch/twiki/bin/view/CMS/SWGuideMuonIdRun2. Accessed: 2016-1-09. [41]

[48] CMS Collaboration, "Performance of Electron Reconstruction and Selection with the CMS Detector in Proton-Proton Collisions at $\sqrt{s} = 8$ TeV", *JINST* **10** (2015), no. 06, P06005, doi:10.1088/1748-0221/10/06/P06005, arXiv:1502.02701. [41]

[49] CMS Collaboration, "Electron performance with 19.6 fb^{-1} of data collected at $\sqrt{s} = 8$ TeV with the CMS detector", CMS-DP-2013-003. [42]

[50] CMS Collaboration, "Cut Based Electron ID for Run 2". https://twiki.cern.ch/twiki/bin/viewauth/CMS/CutBasedElectronIdentificationRun2. Accessed: 2016-1-10. [42]

[51] CMS Collaboration, "Isolated Photon Reconstruction and Identification at $\sqrt{s} = 7$ TeV", CMS-PAS-EGM-10-006. [42]

[52] CMS Collaboration, "Photon ID performance with 19.6 fb^{-1} of data collected at $\sqrt{s} = 8$ TeV with the CMS detector", CMS-DP-2013-010. [42]

[53] CMS Collaboration, "Cut Based Photon ID for Run 2". https://twiki.cern.ch/twiki/bin/view/CMS/CutBasedPhotonIdentificationRun2. Accessed: 2016-1-14. [43]

[54] M. Cacciari, G. P. Salam, and G. Soyez, "The Anti-k(t) jet clustering algorithm", *JHEP* **04** (2008) 063, doi:10.1088/1126-6708/2008/04/063, arXiv:0802.1189. [43]

[55] CMS Collaboration, "Jet Performance in pp Collisions at 7 TeV", CMS-PAS-JME-10-003. [43]

[56] CMS Collaboration, "Pileup measurement and mitigation techniques in CMS", *J. Phys. Conf. Ser.* **404** (2012) 012045, doi:10.1088/1742-6596/404/1/012045. [44]

[57] CMS Collaboration, "Jet Identification". https://twiki.cern.ch/twiki/bin/view/CMS/JetID. Accessed: 2016-1-14. [44]

[58] CMS Collaboration, "Determination of Jet Energy Calibration and Transverse Momentum Resolution in CMS", *JINST* **6** (2011) P11002, doi:10.1088/1748-0221/6/11/P11002, arXiv:1107.4277. [44]

[59] CMS Collaboration, "Identification of b-quark jets with the CMS experiment", *JINST* **8** (2013) P04013, doi:10.1088/1748-0221/8/04/P04013, arXiv:1211.4462. [45]

[60] CMS Collaboration, "Identification of b-quark jets at the CMS Experiment in the LHC Run 2", Technical Report CMS-PAS-BTV-15-001, CERN, Geneva, 2016. [45]

[61] CMS Collaboration, "Measurement of $B\overline{B}$ Angular Correlations based on Secondary Vertex Reconstruction at $\sqrt{s} = 7$ TeV", *JHEP* **03** (2011) 136, doi:10.1007/JHEP03(2011)136, arXiv:1102.3194. [45]

[62] CMS Collaboration, "Performance of b tagging in boosted topology events". https://twiki.cern.ch/twiki/bin/view/CMSPublic/BoostedBTaggingPlots2015. Accessed: 2015-11-21. [46]

[63] CMS Collaboration, "Search for supersymmetry in the multijet and missing transverse momentum final state in pp collisions at 13 TeV", *Phys. Lett. B* (2016) doi:10.1016/j.physletb.2016.05.002, arXiv:1602.06581. [49 and 105]

[64] CMS Collaboration, "Search for gluino mediated bottom- and top-squark production in multijet final states in pp collisions at 8 TeV", *Phys. Lett.* **B725** (2013) 243–270, doi:10.1016/j.physletb.2013.06.058, arXiv:1305.2390. [49, 91, and 102]

[65] CMS Collaboration, "Search for new physics in the multijet and missing transverse momentum final state in proton-proton collisions at $\sqrt{s} = 8$ TeV", *JHEP* **06** (2014) 055, doi:10.1007/JHEP06(2014)055, arXiv:1402.4770. [49, 91, and 102]

[66] J. Alwall, P. C. Schuster, and N. Toro, "Simplified models for a first characterization of new physics at the LHC", *Phys. Rev. D* **79** (Apr, 2009) 075020, doi:10.1103/PhysRevD.79.075020. [51]

[67] Particle Data Group Collaboration, "Review of Particle Physics (RPP)", *Phys. Rev.* **D86** (2012) 010001, doi:10.1103/PhysRevD.86.010001. [72 and 74]

[68] T. Junk, "Confidence level computation for combining searches with small statistics", *Nuclear Instruments and Methods in Physics Research Section A: Accelerators, Spectrometers, Detectors and Associated Equipment* **434** (1999), no. 2 - 3, 435 – 443, doi:10.1016/S0168-9002(99)00498-2. [100]

[69] A. L. Read, "Presentation of search results: The CL(s) technique", *J. Phys.* **G28** (2002) 2693–2704, doi:10.1088/0954-3899/28/10/313. [11 (2002)]. [100]

[70] The ATLAS and CMS Collaborations and the LHC Higgs Combination Group, "Procedure for the LHC Higgs boson search combination in Summer 2011", Technical Report CMS-NOTE-2011-005. ATL-PHYS-PUB-2011-11, CERN, Geneva, Aug, 2011. [100]

[71] CMS Collaboration, "Search for $B_s^0 \to \mu^+\mu^-$ and $B^0 \to \mu^+\mu^-$ decays", *JHEP* **04** (2012) 033, doi:10.1007/JHEP04(2012)033, arXiv:1203.3976. [105]

[72] CMS Collaboration, "Observation of a new Ξ_b baryon", *Phys. Rev. Lett.* **108** (2012) 252002, doi:10.1103/PhysRevLett.108.252002, arXiv:1204.5955. [105]

Appendix A

Service Work

Through the course of my graduate career, I spent considerable time working on the HCAL subsystem of CMS. Specifically, I was an expert in the HCAL Trigger Primitive Generator (TPG) algorithm and a contact person between the HCAL and L1 groups. A thorough understanding from the conversion of hits and signals within HCAL all the way to the transmission of energy to the triggering system was required. This section will summarize this work, starting with the technical description of how a Trigger Primitive is created. Later I will detail a few of the studies performed.

A.1 Trigger Primitive Generation

The role of the HCAL Trigger Primitives (TPs) is to send the energy readout of HCAL to the L1CT. They are computed from the digital samples of HCAL detector pulses. Optical signals are converted to electrical signals using hybrid photodiodes (HPDs) in the scintillator barrel and endcaps detectors (HB and HE respectively, or Hadron barrel and endcap detectors (HBHE) collectively). Simpler PMTs are used in the HF detector. The electrical signal, which is analog, is then converted to a digital signal using a charge-integrating analog-to-digital-converter called the QIE. This 7-bit QIE data is linearized and converted to (transverse) energy. The linearization of the QIE data, or counts, to 10-bit

linear energies is done via an input Look-Up Table (LUT). This input LUT's i-th entry, dependent on individual readout channel, is defined as

$$\mathrm{LUT(i)} = \frac{(\mathrm{Q(i)} - \mathrm{P(i)}) \cdot g \cdot R_{\mathrm{calib}}}{g_{\mathrm{nom}} \cdot \mathcal{G}}, \tag{A.1}$$

where, Q(i) is the inputed QIE data to be linearized, in fC, P(i) is the calibrated minimum of a particular channel, also in fC, g and g_{nom} are the gains associated with converting fC to GeV, R_{calib} is a calibration factor to align the TP energy with its reconstructed energy and $\mathcal{G}$ is the granularity of the channel. The Q, P, and g are all channel-dependent values, having differing values for each individual readout channel. On average, the P(i) is ~3 fC and g is 0.10-0.20 GeV/fC on average. The nominal gain value, g_{nom}, is a constant 0.177 GeV/count while $\mathcal{G}$ accounts for the size of the iϕ channel and is 1 for all of HB, 2 for $18 \geq |\mathrm{i}\eta| \geq 26$, and 5 for $27 \geq |\mathrm{i}\eta| \geq 29$ (see below for the definition of iϕ and iη, in particular Fig. A.3 and Tab. A.1). On average the R_{calib} value is ~1.1 and is shown in Fig. A.1.

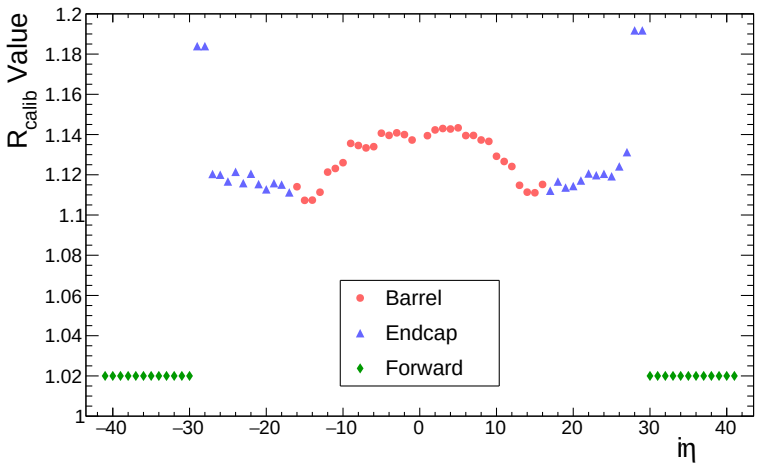

Figure A.1: The R_{calib} factor as a function of iη in HCAL.

In order to assign a specific bunch crossing to HCAL detector pulses, see Fig. A.2, a peak-finding algorithm is used. This peak-finding algorithm uses a sliding sum of two

Time Slices (TSs) to identify the peak:

$$\sum \mathrm{TS} = \mathrm{TS_i} + \mathrm{TS_{i+1}}. \tag{A.2}$$

This sum is then compared to its neighbors, and if the the current sum is bigger than its neighbors it is considered to be the peak. Otherwise the algorithm moves forward a TS to continue to find the peak. The energy associated with the peak then becomes the TP energy, by definition. This sum of two TSs is the reason for the R_{calib} factor, since the sum does not capture the full pulse.

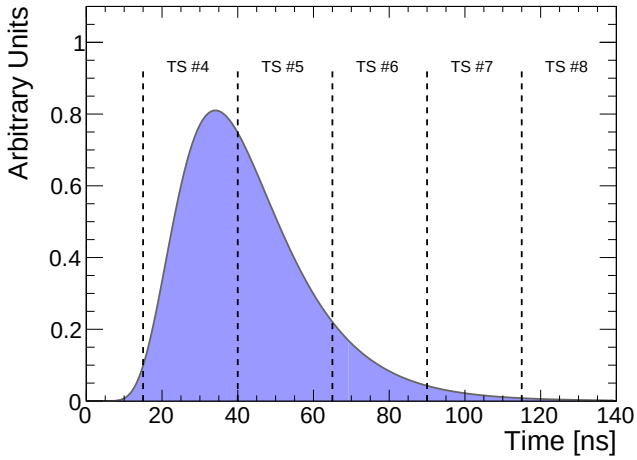

Figure A.2: Illustration of the HCAL pulse shape and its relation to the integrated samples. Time slice 0 is defined by the trigger for a nominally synchronized event. A single TS lasts for 25 ns.

After summing the energy in time a single trigger tower is constructed by summing all depths. A graphic of the distribution of trigger towers is shown in Fig. A.3, while the size and numbering scheme is given in Tab. A.1. The trigger towers also define two spatial parameters which are a mapping of the η and ϕ onto integer values, iη and iϕ respectively. iη can be read off as the tower index from Tab. A.1 and iϕ is 5° increments from 0 to 360° numbering from 1 to 72.

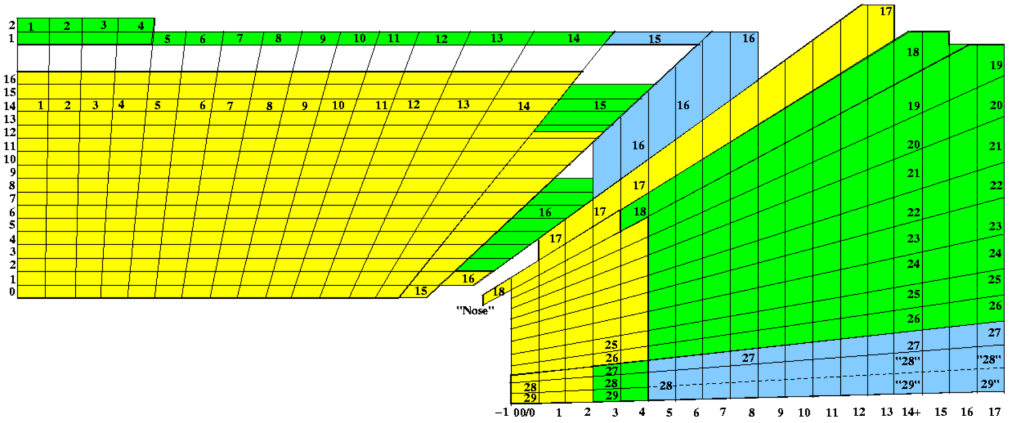

Figure A.3: Schematic view of the trigger tower mapping in the HCAL barrel and endcaps regions in the $r - z$ plane. From Ref. [34].

Once a TP is created in a one-to-one correspondence with a trigger tower, a final LUT is used to compress the 10-bit energy to 8-bit energy before its transmission to the L1CT. This is done to reduce the data flux to the L1CT. The compression algorithm is shown in Fig. A.4, where the algorithm is given by:

$$\mathrm{C(i)} = \sqrt{14.94 \cdot \mathrm{i} \cdot \ln(1 + \frac{\mathrm{i}}{14.94})} + 0.5. \tag{A.3}$$

This compression algorithm then finalizes the HCAL TP which is sent to the triggering system. To summarize then, optical detector pulses are converted into digital counts with the QIE. These QIE counts then convert to energy, measured in GeV, and are then summed over time and depth to create a TP. Before it is sent to the L1CT, the TP energy is compressed. This ends the HCAL triggering chain, as the triggering systems then take these energies, along with the TPs from the other subsystems, to make the trigger determinations.

The preceding explanation applies to both hardware and software. Data uses actual hardware to make the real-time calculations, but the software emulation of the hardware, which obviously mirrors the hardware, is also crucial. When simulating events, the emulation of the TP generation needs to be used. The emulation of the TP generation needs to be accurate.

Table A.1: Sizes of the HCAL trigger towers in η and ϕ. Adapted from Ref. [34].

Tower Index	$\lvert\eta_{\max}\rvert$	Detector	Size	
			η	ϕ (°)
1-15	0.087 $\times\eta$	HB	0.087	5
16	1.392	HB, HE	0.087	5
17-20	0.087 $\times\eta$	HE	0.087	5
21	1.830	HE	0.090	5
22	1.930	HE	0.100	5
23	2.043	HE	0.113	5
24	2.172	HE	0.129	5
25	2.322	HE	0.150	5
26	2.500	HE	0.178	5
27	2.650	HE	0.150	5
28	3.000	HE	0.350	5
29	3.314	HF	0.461	20
30	3.839	HF	0.525	20
31	4.363	HF	0.524	20
32	5.191	HF	0.828	20

A.2 TP Studies

As an expert on the HCAL TP generation, I was assigned various tasks and studies to determine performance and keep maintenance. The validation and upkeep of the TP software is a critical function of the HCAL subsystem. This section will highlight a few of these studies.

A.2.1 Data and simulation mismatch

In late 2012, the L1 group reported a discrepancy between data and simulation in L1 calorimeter energy sums when using 2012 data and its corresponding simulation. It was first noticed when trigger rates of calorimetric quantities were massively over predicted by the simulation, by up to a factor of ten. An official task force was setup to deal with this issue. Both ECAL and HCAL TPs were identified as likely culprits.

As part of the HCAL delegation, I first studied the performance of HCAL TPs in relation to HCAL Reconstructed Hits (RHs). A RH is an offline quantity equivalent to a

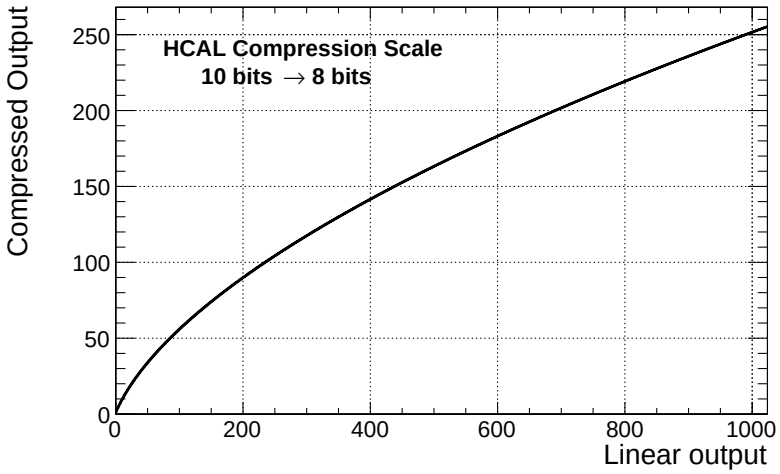

Figure A.4: The compression of the TP linear energy into a non-linear form. The compression algorithm loses some resolution at the high end of the energy scale, but maintains full dynamic range of the energy.

TP, recorded after the triggering systems have performed. TPs and RHs were matched, and then compared, within data and simulation separately. This study would immediately show if the TPs were mis-calibrated or otherwise inflated if the ratio of TP energy to RH energy was greater than one. Fig. A.5 shows the result of this investigation. The ratio of energies between TPs and RHs was found to be consistent with unity and within expectations. This implied the TP algorithm was not likely at fault.

However, the discrepancy did not disappear even after ECAL uncovered and addressed the issues within its subsystem. Every aspect of the HCAL TP generation chain was checked, including the values in Eq. A.1. As part of these checks, plots of the average sum TP E_{T}, $\left\langle \sum E_{\mathrm{T}}^{\mathrm{TP}} \right\rangle$, as a function of number of PVs, N_{PV}, were investigated. These plots revealed that the HE region showed a mismatch between data and simulation, with the mismatch increasing with increasing N_{PV}. The HB region showed no mismatch. These plots are shown in Fig. A.6.

A potential cause of this asymmetric mismatch within HCAL is radiation damage. Degradation was expected to occur within HE due to harsh radiation from particle collisions.

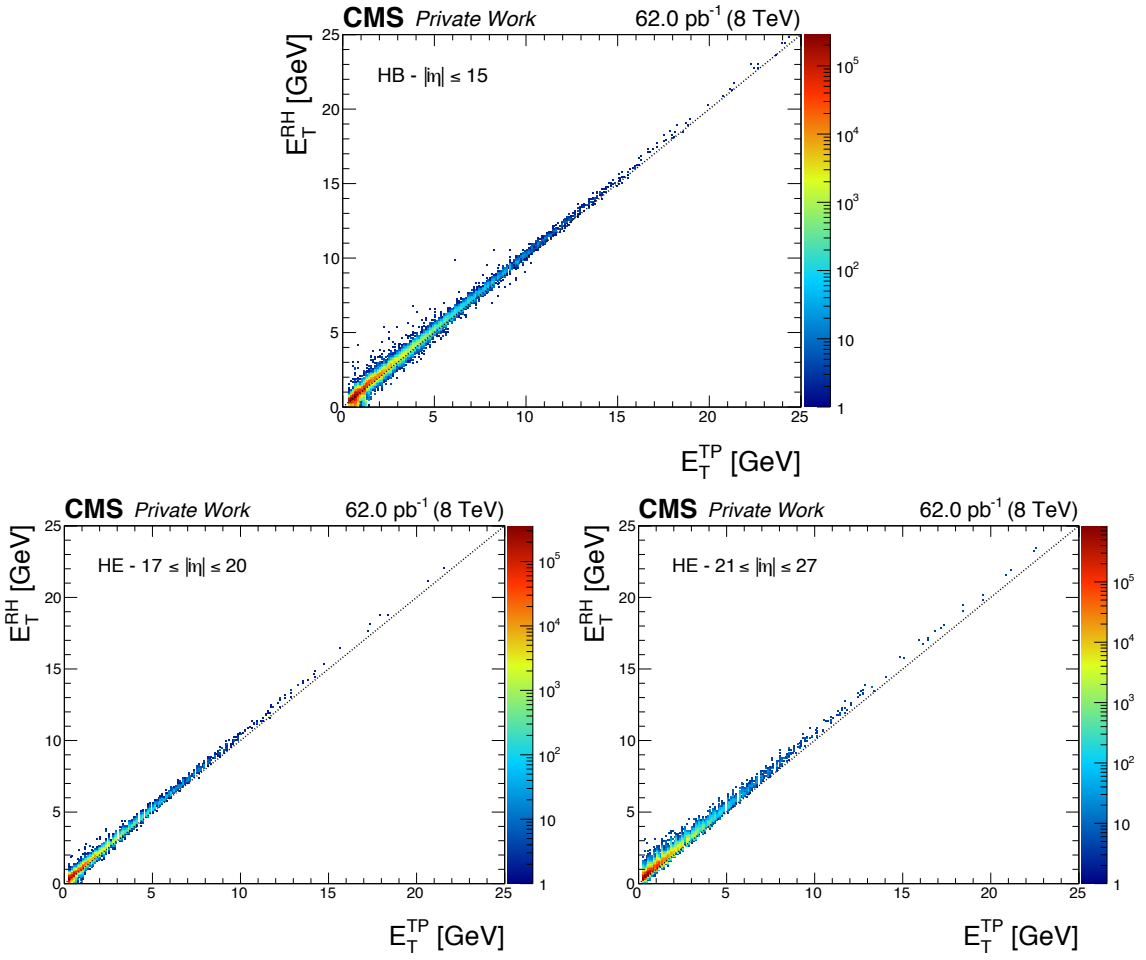

Figure A.5: HCAL subregions plotting E_{T} of matched RH vs. TP in 2012 data. The top plot is the barrel region while the bottom two plots are the endcaps regions split into two regions. The dotted black line shows a slope of one and is there to guide the eye.

However, this was not expected so soon into the initial running of the LHC. When the radiation damage is calculated in the HE region during the 2012 running, it is indeed found to be non-negligible. This can be calculated as a correction factor shown in Fig. A.7. Once the radiation damage is accounted for, the data mismatch with simulation is greatly improved. This has the effect of increasing the energy measured in data, as the data is corrected by the calculated radiation damage. As the radiation damage will keep worsening, continuous measurements and corrections must be determined. The updated plot including

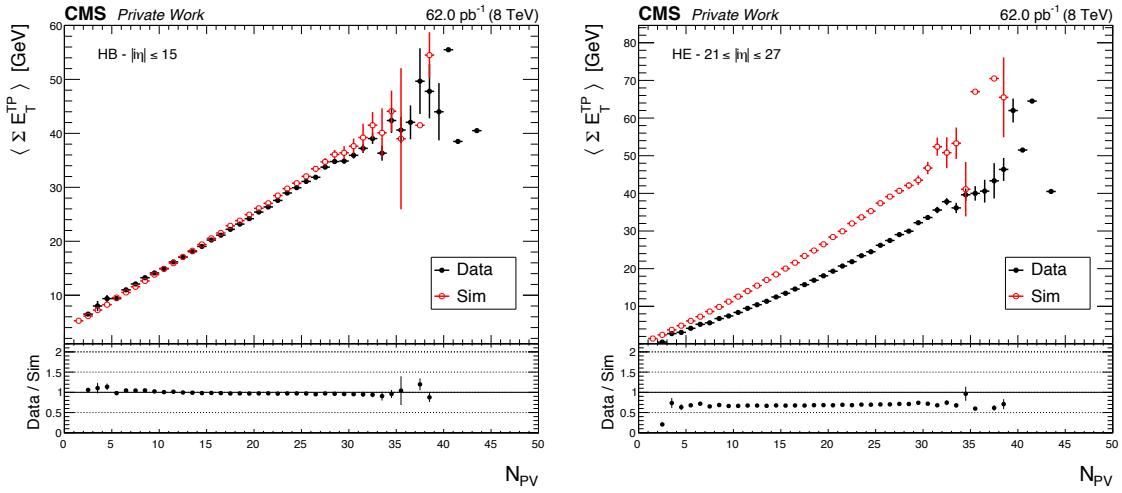

Figure A.6: Plots of $\left\langle \sum E_{\mathrm{T}}^{\mathrm{TP}} \right\rangle$ vs. N_{PV} in the barrel (left) and endcaps (right) regions in 2012. The endcaps show a significant mismatch between data and simulation.

radiation damage is shown in Fig. A.8.

A.2.2 Out-Of-Time Pile-Up

In the lead-up to the 2015 running, an important study was needed concerning potential Out-Of-Time Pile-Up (OOTPU) affecting HCAL TPs and therefore L1 quantities. OOTPU is a form of Pile-Up that occurs when events coming from additional proton-proton interactions originate from successive bunch crossings. In other words, it can become difficult to discern a real event in a bunch crossing from a Pile-Up event from a previous bunch crossing. This was not much of an issue within HCAL when the bunch crossings occurred every 50 ns as this was sufficient time between bunch crossings; however, starting in 2015 this number would drop to the design value of 25 ns. This faster time made it imperative to study what effect, if any, OOTPU had on HCAL. Potential solutions include modifying the peak-finding algorithm, but as will be shown, no actions were required.

In order to study the possible OOTPU effect, two sets of simulated $t\bar{t}$ events were analyzed: one with bunch crossings at 50 ns and one with 25 ns. To try to isolate any OOTPU differences in the two sets of events, TPs were matched to generated jets. Using

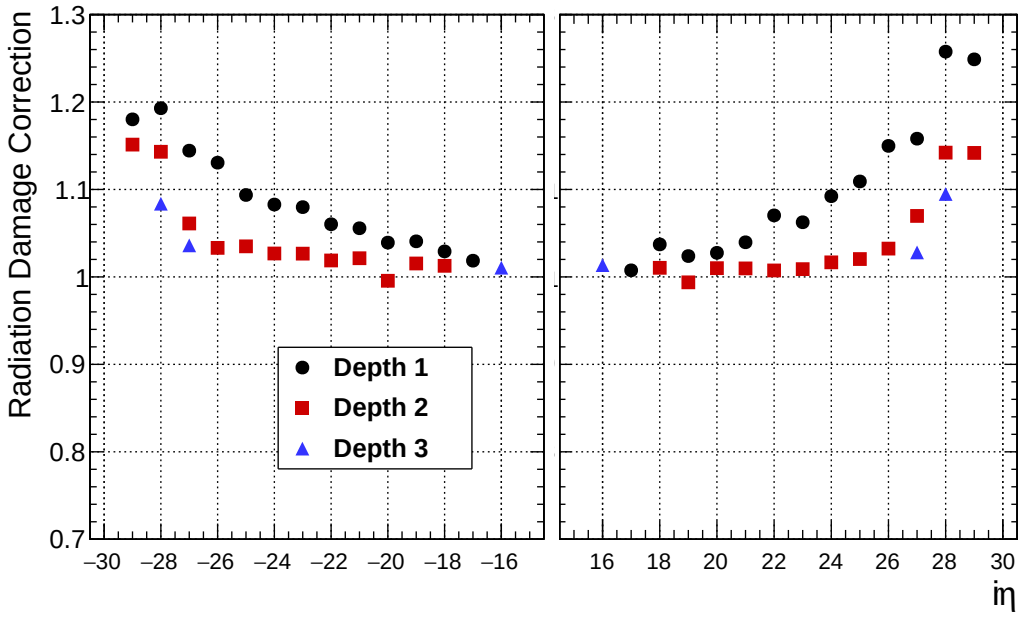

Figure A.7: The radiation damage correction factor as a function of iη and depth in the endcaps region through the end of 2012.

a ΔR cone of 0.5 around a generated jet, all TPs within were summed. This matched TP energy was then compared to the generated jet in question. Since both sets of simulated events have the exact same generated jets, the only difference in this comparison should be

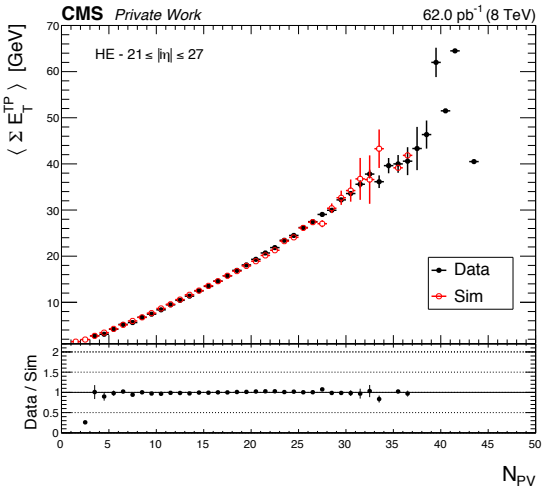

Figure A.8: Plot of $\left\langle \sum E_{\mathrm{T}}^{\mathrm{TP}} \right\rangle$ vs. N_{PV} in the endcaps region with radiation damage included.

the summed energy in the TPs where this summed energy could potentially be altered by OOTPU. Practically, the comparison was made in the form of a ratio, $\sum E_{\mathrm{T}}^{\mathrm{TP,\,matched}}/p_{\mathrm{T}}^{\mathrm{gen}}$, and this distribution was plotted to compare the two sets of simulated events. A large difference would potentially be indicative of a OOTPU affecting the HCAL TPG. As shown in Fig. A.9, the agreement in the $\sum E_{\mathrm{T}}^{\mathrm{TP,\,matched}}/p_{\mathrm{T}}^{\mathrm{gen}}$ ratio between the 50 ns and 25 ns was good. There did not seem to be any notable disagreements. To ensure there was no dependence on the generated jet p_{T}, the average ratio, $\left\langle \sum E_{\mathrm{T}}^{\mathrm{TP,\,matched}}/p_{\mathrm{T}}^{\mathrm{gen}} \right\rangle$, was plotted as a function of the generated jet p_{T}. This formed a sort of an efficiency measurement. This check can be seen in Fig. A.10 and there was again good agreement between the two sets of simulated $t\bar{t}$ events. Based on these studies, OOTPU was not deemed to be a problem in HCAL.

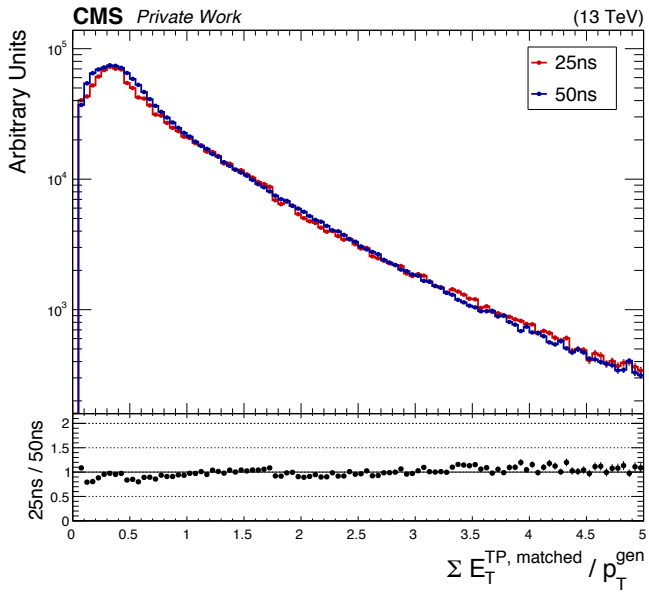

Figure A.9: Plot of $\sum E_{\mathrm{T}}^{\mathrm{TP,\,matched}}$ ratio comparing the 50 ns and 25 ns simulated $t\bar{t}$ events.

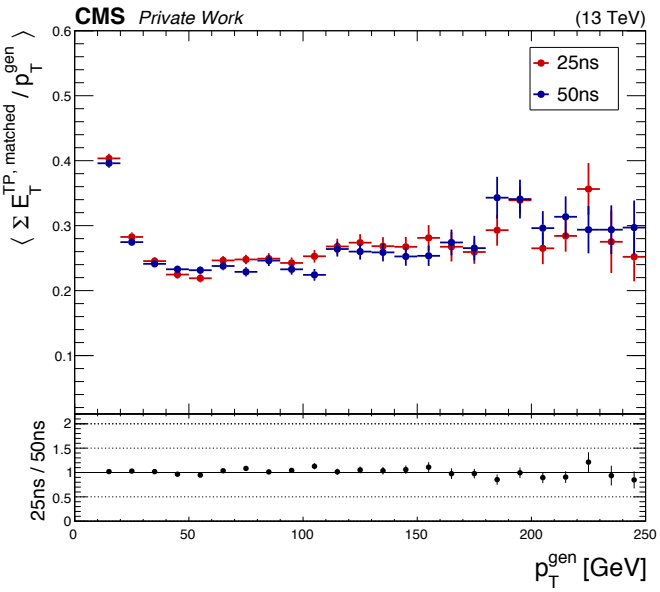

Figure A.10: Plot of $\sum E_{\mathrm{T}}^{\mathrm{TP,\,matched}}$ as a function of $p_{\mathrm{T}}^{\mathrm{gen}}$ comparing the 50 ns and 25 ns simulated $t\bar{t}$ events.

Appendix B

Background Simulated Samples

Table B.1: All Standard Model (BG) simulated samples used in the analysis. The order in which the cross sections were calculated are given for each process.

Dataset	σ **(pb)**	$\int \mathcal{L}\,\mathrm{d}t$ **(fb^{-1})**
SM $t\bar{t}$ simulated datasets with cross sections calculated at NNLO		
TTJets_TuneCUETP8M1_13TeV-madgraphMLM-pythia8	816.0	13.90
TTJets_SingleLeptFromT_TuneCUETP8M1_13TeV-madgraphMLM-pythia8	179.3	324.6
TTJets_SingleLeptFromTbar_TuneCUETP8M1_13TeV-madgraphMLM-pythia8	179.3	335.7
TTJets_DiLept_TuneCUETP8M1_13TeV-madgraphMLM-pythia8	86.66	351.2
TTJets_HT-600to800_TuneCUETP8M1_13TeV-madgraphMLM-pythia8	2.615	1898
TTJets_HT-800to1200_TuneCUETP8M1_13TeV-madgraphMLM-pythia8	1.077	3198
TTJets_HT-1200to2500_TuneCUETP8M1_13TeV-madgraphMLM-pythia8	0.195	5063
TTJets_HT-2500toInf_TuneCUETP8M1_13TeV-madgraphMLM-pythia8	0.002	218575
SM QCD simulated datasets with cross sections calculated at LO		
QCD_HT200to300_TuneCUETP8M1_13TeV-madgraphMLM-pythia8	1735000	0.01
QCD_HT300to500_TuneCUETP8M1_13TeV-madgraphMLM-pythia8	366800	0.05
QCD_HT500to700_TuneCUETP8M1_13TeV-madgraphMLM-pythia8	29370	0.67
QCD_HT700to1000_TuneCUETP8M1_13TeV-madgraphMLM-pythia8	6524	2.30
QCD_HT1000to1500_TuneCUETP8M1_13TeV-madgraphMLM-pythia8	1064	4.67
QCD_HT1500to2000_TuneCUETP8M1_13TeV-madgraphMLM-pythia8	121.5	31.67
QCD_HT2000toInf_TuneCUETP8M1_13TeV-madgraphMLM-pythia8	25.42	77.17
SM $\mathrm{Z} \to \nu\bar{\nu}$ +jets simulated datasets with cross sections calculated at NNLO		
ZJetsToNuNu_HT-100To200_13TeV-madgraph	345.0	14.92
ZJetsToNuNu_HT-200To400_13TeV-madgraph	96.38	52.22

Continued on next page

Table B.1 – *Continued from previous page*

Dataset	σ **(pb)**	$\int \mathcal{L}\,\mathrm{d}t$ **(fb^{-1})**
ZJetsToNuNu_HT-400To600_13TeV-madgraph	13.46	75.34
ZJetsToNuNu_HT-600ToInf_13TeV-madgraph	5.170	196.5
SM $W \to \ell\nu$+jets simulated datasets with cross sections calculated at NNLO		
WJetsToLNu_HT-100To200_TuneCUETP8M1_13TeV-madgraphMLM-pythia8	1635	6.20
WJetsToLNu_HT-200To400_TuneCUETP8M1_13TeV-madgraphMLM-pythia8	437.0	11.97
WJetsToLNu_HT-400To600_TuneCUETP8M1_13TeV-madgraphMLM-pythia8	59.50	31.96
WJetsToLNu_HT-600ToInf_TuneCUETP8M1_13TeV-madgraphMLM-pythia8	22.80	45.44
WJetsToLNu_HT-600To800_TuneCUETP8M1_13TeV-madgraphMLM-pythia8	15.50	257.1
WJetsToLNu_HT-800To1200_TuneCUETP8M1_13TeV-madgraphMLM-pythia8	6.366	247.4
WJetsToLNu_HT-1200To2500_TuneCUETP8M1_13TeV-madgraphMLM-pythia8	1.614	158.4
WJetsToLNu_HT-2500ToInf_TuneCUETP8M1_13TeV-madgraphMLM-pythia8	0.037	6770
SM Single top simulated datasets with cross sections calculated at NLO		
ST_s-channel_4f_leptonDecays_13TeV-amcatnlo-pythia8_TuneCUETP8M1	3.340	183.6
ST_t-channel_antitop_4f_leptonDecays_13TeV-powheg-pythia8_TuneCUETP8M1	26.23	64.64
ST_t-channel_top_4f_leptonDecays_13TeV-powheg-pythia8_TuneCUETP8M1	44.07	74.88
ST_tW_antitop_5f_inclusiveDecays_13TeV-powheg-pythia8_TuneCUETP8M1	35.80	27.93
ST_tW_top_5f_inclusiveDecays_13TeV-powheg-pythia8_TuneCUETP8M1	35.80	27.81
SM diboson and other rare process simulated datasets with cross sections calculated at NNLO		
ttHJetTobb_M125_13TeV_amcatnloFXFX_madspin_pythia8	0.293	18269
TTZToLLNuNu_M-10_TuneCUETP8M1_13TeV-amcatnlo-pythia8	0.228	811.4
TTZToQQ_TuneCUETP8M1_13TeV-amcatnlo-pythia8	0.530	663.4
TTWJetsToLNu_TuneCUETP8M1_13TeV-amcatnloFXFX-madspin-pythia8	0.204	635.6
TTWJetsToQQ_TuneCUETP8M1_13TeV-amcatnloFXFX-madspin-pythia8	0.423	1018
ZH_HToBB_ZToNuNu_M125_13TeV_amcatnloFXFX_madspin_pythia8	0.100	12116
WH_HToBB_WToLNu_M125_13TeV_amcatnloFXFX_madspin_pythia8	0.260	4782
WWTo1L1Nu2Q_13TeV_amcatnloFXFX_madspin_pythia8	50.00	64.26
WWTo2L2Nu_13TeV-powheg	12.18	158.5
WZTo1L1Nu2Q_13TeV_amcatnloFXFX_madspin_pythia8	10.71	1339
WZTo1L3Nu_13TeV_amcatnloFXFX_madspin_pythia8	3.058	305.7
ZZTo2Q2Nu_13TeV_amcatnloFXFX_madspin_pythia8	4.040	5556
ZZTo2L2Q_13TeV_amcatnloFXFX_madspin_pythia8	3.220	3706
TTTT_TuneCUETP8M1_13TeV-amcatnlo-pythia8	0.009	57031
WWZ_TuneCUETP8M1_13TeV-amcatnlo-pythia8	0.165	1341
WZZ_TuneCUETP8M1_13TeV-amcatnlo-pythia8	0.056	3938
ZZZ_TuneCUETP8M1_13TeV-amcatnlo-pythia8	0.014	15297
SM DY+jets simulated datasets with cross sections calculated at NNLO		

Continued on next page

Table B.1 – *Continued from previous page*

Dataset	σ **(pb)**	$\int \mathcal{L}\,\mathrm{d}t$ **(fb**$^{-1}$**)**
DYJetsToLL_M-50_TuneCUETP8M1_13TeV-madgraphMLM-pythia8	6025	1.50
DYJetsToLL_M-50_HT-100to200_TuneCUETP8M1_13TeV-madgraphMLM-pythia8	171.5	15.31
DYJetsToLL_M-50_HT-200to400_TuneCUETP8M1_13TeV-madgraphMLM-pythia8	52.58	18.18
DYJetsToLL_M-50_HT-400to600_TuneCUETP8M1_13TeV-madgraphMLM-pythia8	6.761	155.0
DYJetsToLL_M-50_HT-600toInf_TuneCUETP8M1_13TeV-madgraphMLM-pythia8	2.718	363.5
SM γ+jets simulated datasets with cross sections calculated at LO		
GJets_HT-100To200_TuneCUETP8M1_13TeV-madgraphMLM-pythia8	22010	0.23
GJets_HT-200To400_TuneCUETP8M1_13TeV-madgraphMLM-pythia8	9110	1.13
GJets_HT-400To600_TuneCUETP8M1_13TeV-madgraphMLM-pythia8	273	9.07
GJets_HT-600ToInf_TuneCUETP8M1_13TeV-madgraphMLM-pythia8	94.5	26.99

Appendix C

Additional Interpretations

Supplementary SMS signal scenarios are presented in this Appendix. These scenarios are interpreted in the same way as the ones presented in Sec. 5.1.3 using the same statistical procedure, outlined in Sec. 7.3.1, as well.

C.1 T2tt signal scenario

The T2tt scenario features stop ($\tilde{t}$) pair production. Each stop decays into a $t\widetilde{\chi}_1^0$, which is assumed to be the LSP. The scenario scans the stop mass-neutralino mass plane. The event topology and exclusion limits for T2tt are given in Fig. C.1.

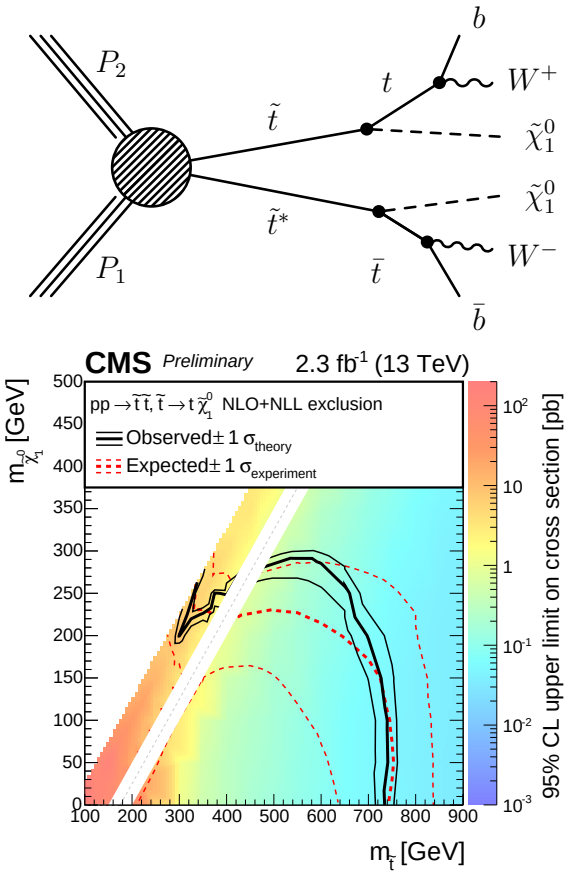

Figure C.1: An event diagram illustration for the T2tt signal model is given in the top plot, with the exclusion limit for the T2tt scenario given in the bottom plot. The region where $M_{\tilde{t}_1} \approx M_t + M_{\tilde{\chi}_1^0}$ is hidden, as this region of parameter space will be targeted by a separate, dedicated search.

C.2 T1ttbb signal scenario

The T1ttbb scenario features a similar gluino ($\tilde{g}$) pair production as the T1bbbb and T1tttt scenarios. The difference is the branching ratios of each gluino. In total there are six possible topologies:

1. each gluino decays into $b\bar{b}\tilde{\chi}_1^0$, like T1bbbb
2. each gluino decays into $t\bar{t}\tilde{\chi}_1^0$, like T1tttt
3. each gluino decays into $tb\tilde{\chi}_1^\pm$, where the $\tilde{\chi}_1^\pm$ decays into a $W^*\tilde{\chi}_1^0$ (the W^* is virtual)
4. each gluino decays with 50% branching ratio to $b\bar{b}\tilde{\chi}_1^0$ and 50% branching ratio to $tb\tilde{\chi}_1^\pm$, where the $\tilde{\chi}_1^\pm$ decays into a $W^*\tilde{\chi}_1^0$ (the W^* is virtual)
5. each gluino decays with 50% branching ratio to $t\bar{t}\tilde{\chi}_1^0$ and 50% branching ratio to $tb\tilde{\chi}_1^\pm$, where the $\tilde{\chi}_1^\pm$ decays into a $W^*\tilde{\chi}_1^0$ (the W^* is virtual)
6. each gluino decays with 25% branching ratio to $b\bar{b}\tilde{\chi}_1^0$, 25% branching ratio to $t\bar{t}\tilde{\chi}_1^0$ and 50% branching ratio to $tb\tilde{\chi}_1^\pm$, where the $\tilde{\chi}_1^\pm$ decays into a $W^*\tilde{\chi}_1^0$ (the W^* is virtual)

In the topologies where the $\tilde{\chi}_1^\pm$ decay to a $\tilde{\chi}_1^0$, the mass difference between two is set to 5 GeV. As in the other signal scenarios, the $\tilde{\chi}_1^0$ is assumed to be the LSP. The scenario scans the gluino mass-neutralino mass plane. The event topology and exclusion limits for T1ttbb are given in Fig. C.2.

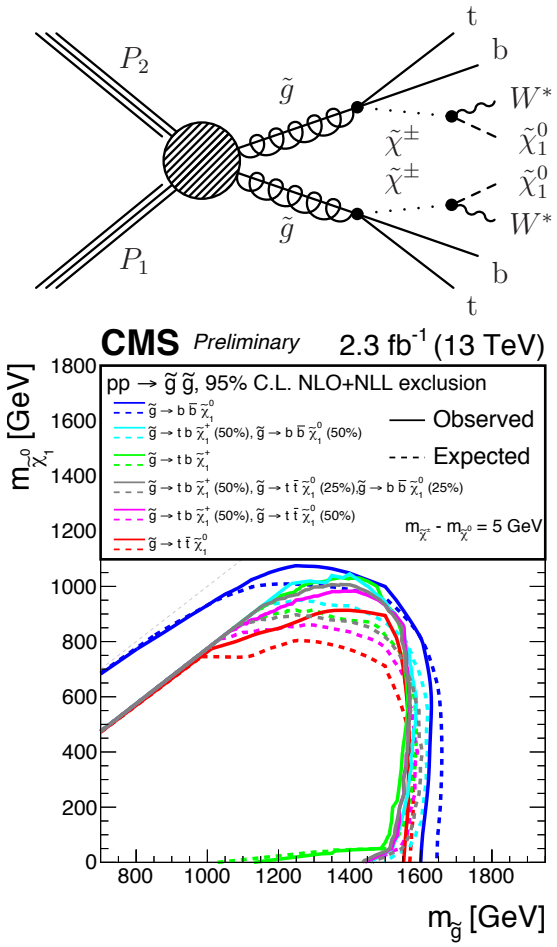

Figure C.2: An event diagram illustration for the third T1ttbb signal model topology ($\tilde{g} \to tb\widetilde{\chi}_1^{\pm}$) is given in the top plot, with the exclusion limit for the T1ttbb scenario given in the bottom plot. The six T1ttbb signal topologies for different gluino branching ratios are separated by color.